

SOLVING ATOMIC STRUCTURES USING STATISTICAL MECHANICAL SEARCHES ON  
X-RAY SCATTERING DERIVED POTENTIAL ENERGY SURFACES

by

Christopher James Wright

Bachelor of Science  
Brown University 2014

---

Submitted in Partial Fulfillment of the Requirements

for the Degree of Masters of Science in

Chemical Engineering

College of Engineering and Computing

University of South Carolina

2016

Accepted by:

Xiao-Dong Zhou, Major Professor

Mark Uline, Committee Member

Jochen Lauterbach, Committee Member

Lacy Ford, Vice Provost and Dean of Graduate Studies

© Copyright by Christopher James Wright, 2016  
All Rights Reserved.

## DEDICATION

To Diane & Donald Wright

My first scientific advisers

*To see a World in a Grain of Sand*

## ACKNOWLEDGMENTS

This work would not have been possible without my entire ensemble of colleagues, advisers, friends, and family.

To Dr. Sanjit Ghose thank you very much for getting me started in the x-ray field and sticking with me, even when I went into the mathematical deep end. To Dr. Yan Li, thank you very much for always pushing my simulations to be the best they could be, and pushing me to search every possible nook and cranny of parameter space. To Daniel DeCiccio I am eternally greatful...

To Emir, thank you very much for being my partner in beamtime. I hope you continue your x-ray work. I'd also like to thank the NSLS-II XPD team for their experimental, intellectual, and moral support. To Dr. Thomas Caswell, Dr. Eric Dill, and Dr. Dan Allen, I would not be  $1e^{-6}$  of the programmer I am today without your guidance, conversation, and explanations.

To Prof. Scopatz, thank you very much for your insights, conversation, and being a spectacular developer role model.

To my many readers, I'd like to say thank you, if my thesis hasn't put you to sleep already.

To my parents, I don't know if any language could correctly render the magnitude of my gratitude for everything you have done for me.

Last, but certainly not least, Prof. Zhou. I am certain that I could not have gotten a better start in research science than working with you.

## ABSTRACT

Engineering the next generation of materials, especially nanomaterials, requires a detailed understanding of the material's underlying atomic structure. By understanding these structures we can obtain a better insight into their structure-property relationship, allowing for a property driven rational design of the material structure on the atomic level. Even more importantly, understanding the structure in-situ will allow the reversal of the flow of information, translating stimuli and responses on the macroscopic system level to changes in the atomic structure. Despite the importance of atomic structures for designing materials, solving the atomic structure of materials is difficult both experimentally and computationally. Atomic pair distribution functions (PDFs) have been shown to provide information on atomic structure, although extracting the PDF from x-ray total scattering measurements can be difficult. Computationally, translating the PDF to an atomic structure requires the search of a very high dimensional space, the set of all potential atomic configurations, and can be computationally expensive.

This work aims to address these issues by developing 1) novel statistical mechanical approaches to solving material structures, 2) fast simulation of x-ray total scattering and atomic pair distribution functions (PDFs), and 3) data processing procedures for experimental x-ray total scattering measurements. First, experimentally derived potential energy surfaces (PES) and the statistical mechanical ensembles used to search them are developed. Then the mathematical and computational framework for the PDF and its gradients will be discussed. The combined PDF-PES-ensemble system will be benchmarked against a series of nanoparticle structures to ascertain

the efficiency and effectiveness of the system. Experimental data processing procedures, which maximize the usable data, will be presented. Finally, preliminary results from experimental x-ray total scattering measurements will be discussed. This work presents one of the most complete end-to-end systems for processing and modeling x-ray total scattering PDF data, potentially allowing for high-throughput structural solution.

## TABLE OF CONTENTS

DEDICATION . . . . .	iii
ACKNOWLEDGMENTS . . . . .	iv
ABSTRACT . . . . .	v
LIST OF FIGURES . . . . .	x
TODO LIST . . . . .	1
CHAPTER 1 INTRODUCTION . . . . .	2
CHAPTER 2 STATISTICAL MECHANICAL ENSEMBLES AND POTENTIAL ENERGY SURFACES . . . . .	4
2.1 Introduction . . . . .	4
2.2 Potential Energy Surfaces . . . . .	4
Experimentally Derived Potential Energy Surfaces . . . . .	5
Potentials . . . . .	5
Forces . . . . .	7
2.3 Ensembles . . . . .	7
Monte Carlo Modeling . . . . .	8
Hamiltonian Monte Carlo . . . . .	9
No-U-Turn Sampling . . . . .	11
Grand Canonical Ensemble . . . . .	11
Ensemble description . . . . .	12
Grand Canonical Monte Carlo . . . . .	12
GCMC biasing . . . . .	13
2.4 Conclusions . . . . .	16

<b>CHAPTER 3 ATOMIC PAIR DISTRIBUTION FUNCTION: THEORY AND COMPUTATION . . . . .</b>	<b>17</b>
3.1 Introduction . . . . .	17
3.2 Theory . . . . .	18
Derivation . . . . .	18
Analytically Gradients . . . . .	19
Without ADPs . . . . .	20
Periodic Boundary Conditions . . . . .	21
3.3 Computation . . . . .	21
HPC and GPUs . . . . .	22
GPUs and Parallelization . . . . .	22
Map from ij space to k space . . . . .	23
GPU Memory Allocation . . . . .	25
Speed and Scaling of PDF Computation . . . . .	27
3.4 Conclusions . . . . .	28
 <b>CHAPTER 4 BENCHMARKS . . . . .</b>	 29
4.1 Introduction . . . . .	29
Target Setup . . . . .	30
Model Parameters . . . . .	31
4.2 Structural Solutions . . . . .	32
Case I: crystalline Au <sub>55</sub> . . . . .	32
Case II: Au <sub>55</sub> with surface disorder . . . . .	33
Case III: amorphous Au <sub>55</sub> . . . . .	35
Case IV: ligand-protected Au <sub>102</sub> . . . . .	37
Starting from fcc structure . . . . .	37
Starting from Marks Decahedron . . . . .	39
4.3 Discussion and Conclusion . . . . .	40
 <b>CHAPTER 5 X-RAY TOTAL SCATTERING DATA ACQUISITION AND PRO- CESSING . . . . .</b>	 43
5.1 Introduction . . . . .	43
5.2 Detector $Q$ resolution . . . . .	43

5.3	Automated Mask Generation . . . . .	46
	Introduction . . . . .	46
	Algorithm Design . . . . .	47
	Test Cases . . . . .	47
	Results and Discussion . . . . .	52
	Conclusions . . . . .	55
5.4	Automated Image Azimuthal Integration . . . . .	55
5.5	Conclusions . . . . .	60
 CHAPTER 6 PHASE CHANGES AND ANNEALING DYNAMICS OF $\text{Pr}_2\text{NiO}_4$ AND ITS DERIVATIVES . . . . .		61
6.1	Introduction . . . . .	61
6.2	Experiments . . . . .	62
	$\text{Pr}_2\text{NiO}_4$ Synthesis . . . . .	62
	X-ray Measurements . . . . .	62
6.3	Data Processing . . . . .	62
6.4	Data Analysis . . . . .	63
	Intra Sample Comparison . . . . .	63
	PDF . . . . .	63
	$I(Q)$ . . . . .	68
	Inter Sample Comparison . . . . .	73
6.5	Simulation . . . . .	76
6.6	Conclusions . . . . .	76
 CHAPTER 7 CONCLUSION . . . . .		78
 BIBLIOGRAPHY . . . . .		81
 APPENDIX A SUPPLEMENTAL INFORMATION: PHASE CHANGES AND AN- NEALING DYNAMICS OF $\text{Pr}_2\text{NiO}_4$ AND ITS DERIVATIVES . . .		87
	Intra Sample Comparison . . . . .	87
	Inter Sample Comparison . . . . .	100

## LIST OF FIGURES

Figure 2.1	Addition biasing with a Lennard Jones potential.	15
Figure 3.1	Comparison of the CPU and GPU chip architectures	22
Figure 3.2	Speed comparison of CPU and GPU implementations	27
Figure 4.1	Au <sub>55</sub> PDF fitting of DFT-optimized <i>c</i> -Au <sub>55</sub> .	33
Figure 4.2	Au <sub>55</sub> PDF fitting of surface-disordered Au <sub>55</sub> .	34
Figure 4.3	Similar to figure 4.2 for DFT-optimized amorphous Au <sub>55</sub> .	36
Figure 4.4	Similar to Fig. 4.2 for Au <sub>102</sub> as in DFT-optimized Au <sub>102</sub> MBA <sub>44</sub> cluster.	38
Figure 4.5	Similar to Fig. 4.4 with Marks decahedron as the starting structure.	39
Figure 5.1	Scattering onto a flat detector	44
Figure 5.2	$Q$ resolution as a function of $Q$ .	45
Figure 5.3	Number of pixels as a function of $Q$ , binned at the $Q$ resolution of the detector.	46
Figure 5.4	Generated dead/hot pixel masks for a detector with 100 bad pixels.	48
Figure 5.5	Generated dead/hot pixel masks for a detector with 300 bad pixels.	49
Figure 5.6	Generated dead/hot pixel masks for a detector with 500 bad pixels.	49
Figure 5.7	Generated dead/hot pixel masks for a detector with 1000 bad pixels.	50
Figure 5.8	Generated beamstop holder masks for a beamstop holder with 10% transmittance.	50

Figure 5.9 Generated beamstop holder masks for a beamstop holder with 30% transmittance. . . . .	51
Figure 5.10 Generated beamstop holder masks for a beamstop holder with 50% transmittance. . . . .	51
Figure 5.11 Generated beamstop holder masks for a beamstop holder with 90% transmittance. . . . .	51
Figure 5.12 Generated beamstop holder masks which is rotated away from vertical. . . . .	52
Figure 5.13 Masked experimental data. . . . .	53
Figure 5.14 Masked experimental data with Pt single crystal signal. . . . .	53
Figure 5.15 Masked experimental data with Pt single crystal signal using figure's 5.13 mask as a starting mask. . . . .	54
Figure 5.16 Masking, average, and standard deviation of an example x-ray total scattering measurement with with no mask. . . . .	57
Figure 5.17 Masking, average, and standard deviation of an example x-ray total scattering measurement with with only an edge mask. . . . .	58
Figure 5.18 Masking, average, and standard deviation of an example x-ray total scattering measurement with combining an edge mask and the automatically generated mask. . . . .	59
Figure 6.1 PDF as a function of temperature for as synthesized PNO showing the full PDF . . . . .	64
Figure 6.2 PDF as a function of temperature for as synthesized PNO showing a close up on the short range section . . . . .	65
Figure 6.3 PDF as a function of temperature for PNO annealed at 750 °C for 25 hours showing the full PDF . . . . .	66
Figure 6.4 PDF as a function of temperature for PNO annealed at 750 °C for 25 hours showing a close up on the short range section . . . . .	67
Figure 6.5 $I(Q)$ as a function of temperature for as synthesized PNO showing the full XRD . . . . .	69

Figure 6.6 $I(Q)$ as a function of temperature for as synthesized PNO showing a close up on the low $Q$ section . . . . .	70
Figure 6.7 $I(Q)$ as a function of temperature for PNO annealed at 750 °C for 25 hours showing the full XRD . . . . .	71
Figure 6.8 $I(Q)$ as a function of temperature for PNO annealed at 750 °C for 25 hours showing a close up on the low $Q$ section . . . . .	72
Figure 6.9 Comparison of PNO sample PDFs as a function of annealing time high-temp . . . . .	74
Figure 6.10 Comparison of PNO sample $I(Q)$ as a function of annealing time high-temp . . . . .	75
Figure A.1 PDF as a function of temperature for PNO annealed at 750 °C for 50 hours showing the full PDF . . . . .	88
Figure A.2 PDF as a function of temperature for PNO annealed at 750 °C for 50 hours showing a close up on the short range section . . . . .	89
Figure A.3 PDF as a function of temperature for PNO annealed at 750 °C for 100 hours showing the full PDF . . . . .	90
Figure A.4 PDF as a function of temperature for PNO annealed at 750 °C for 100 hours showing a close up on the short range section . . . . .	91
Figure A.5 PDF as a function of temperature for PNO annealed at 750 °C for 200 hours showing the full PDF . . . . .	92
Figure A.6 PDF as a function of temperature for PNO annealed at 750 °C for 200 hours showing a close up on the short range section . . . . .	93
Figure A.7 $I(Q)$ as a function of temperature for PNO annealed at 750 °C for 50 hours showing the full XRD . . . . .	94
Figure A.8 $I(Q)$ as a function of temperature for PNO annealed at 750 °C for 50 hours showing a close up on the low $Q$ section . . . . .	95
Figure A.9 $I(Q)$ as a function of temperature for PNO annealed at 750 °C for 100 hours showing the full XRD . . . . .	96
Figure A.10 $I(Q)$ as a function of temperature for PNO annealed at 750 °C for 100 hours showing a close up on the low $Q$ section . . . . .	97

Figure A.11 $I(Q)$ as a function of temperature for PNO annealed at 750 °C for 200 hours showing the full XRD . . . . .	98
Figure A.12 $I(Q)$ as a function of temperature for PNO annealed at 750 °C for 200 hours showing a close up on the low $Q$ section . . . . .	99
Figure A.13 Comparison of PNO sample PDFs as a function of annealing time at room temperature . . . . .	101
Figure A.14 Comparison of PNO sample PDFs as a function of annealing time at room temperature . . . . .	102
Figure A.15 Comparison of PNO sample PDFs as a function of annealing time at room temperature . . . . .	103
Figure A.16 Comparison of PNO sample PDFs as a function of annealing time at room temperature . . . . .	104
Figure A.17 Comparison of PNO sample PDFs as a function of annealing time at operating temperature . . . . .	105
Figure A.18 Comparison of PNO sample PDFs as a function of annealing time at operating temperature . . . . .	106
Figure A.19 Comparison of PNO sample PDFs as a function of annealing time at operating temperature . . . . .	107
Figure A.20 Comparison of PNO sample PDFs as a function of annealing time at operating temperature . . . . .	108
Figure A.21 Comparison of PNO sample PDFs as a function of annealing time cooled back to room temperature . . . . .	109
Figure A.22 Comparison of PNO sample PDFs as a function of annealing time cooled back to room temperature . . . . .	110
Figure A.23 Comparison of PNO sample PDFs as a function of annealing time cooled back to room temperature . . . . .	111
Figure A.24 Comparison of PNO sample PDFs as a function of annealing time cooled back to room temperature . . . . .	112
Figure A.25 Comparison of PNO sample $I(Q)$ as a function of annealing time at room temperature . . . . .	113

Figure A.26 Comparison of PNO sample  $I(Q)$  as a function of annealing time at operating temperature . . . . . 114

Figure A.27 Comparison of PNO sample  $I(Q)$  as a function of annealing time cooled back to room temperature . . . . . 115

1

## TODO LIST

- |   |   |    |
|---|---|----|
| 2 | Put in the definition of $Rw$ . . . . .         | 6  |
| 3 | state that the $\vec{u}$ are the ADPs . . . . . | 19 |

4

# CHAPTER 1

5

## INTRODUCTION

6 Engineering materials and chemicals on the atomic scale has long been a goal for  
7 the chemistry, physics, materials science, and chemical engineering fields. Realizing  
8 this goal could lead to more durable fuel cell catalysts, bioavailable pharmaceuticals,  
9 and radiation resistant shielding. Before we can even think of making atomistically  
10 exact, durable, or reproducibly changing structures, we need to know the precise  
11 atomic structure. This work bridges the gap in structural knowledge by developing  
12 a methodology for solving the structure of materials by matching experimental x-ray  
13 total scattering data with simulated atomic structures.

14 Chapter 2 develops the statistical mechanical system used to match experimen-  
15 tal and theoretical structures. §2.2 focuses on potential energy surfaces, including  
16 potential energy and force equations, which have minima where experimental results  
17 and simulated structures agree the most. §2.3 will discuss the statistical mechanical  
18 ensembles which search the potential energy surface for minima.

19 Chapter 3 develops the mathematical and computational framework for the atomic  
20 pair distribution function (PDF). §3.3 will focus on the rapid graphical processing  
21 unit based calculation of the PDF and its gradients.

22 Chapter 4 will discuss the benchmarking of the the combined statistical mechan-  
23 ical optimizer and PDF calculation systems against a series of theoretical nanopar-  
24 ticles. These benchmarks will focus on understanding the limitations of the method  
25 and the relationship between goodness of fit and structure reproduction.

26 Chapter 5 will focus on the acquisition of experimental data, their management,

27 and processing. §5.2, 5.3, and 5.4 will discuss the derivation of the  $Q$  resolution  
28 function, the automated masking of 2D area detectors using the previously derived  
29  $Q$  resolution, and the impact of different averaging methods and masks on azimuthal  
30 integration, respectively.

31 Chapter 6 will discuss preliminary experimental results investigating the phase  
32 changes and local structure of  $\text{Pr}_2\text{NiO}_4$ , revealing the influence of thermal history on  
33 the structure. This chapter will also analyze the discrepancy between the reciprocal  
34 space scattering and the PDF.

35

## CHAPTER 2

36

# STATISTICAL MECHANICAL ENSEMBLES AND POTENTIAL ENERGY SURFACES

38 2.1 INTRODUCTION

39 The approach taken in this work for solving the atomic structures of materials is one  
40 of optimization. The plan is to develop a potential energy surface (PES) which has  
41 minima associated with atomic structures who's properties match the experimentally  
42 observed properties. Thus, the various positional variables of the structure can be  
43 solved by optimizing the structure against the PES. This approach is popular in the  
44 PDF community for solving the structure of materials using both extensive large box  
45 models and simpler small box models.

46 In this chapter we discuss the development of the various PESs used in the PDF  
47 community for comparing theoretical and experimental PDFs. Special attention will  
48 be paid to the gradients of the potential energy functions, as these are important  
49 to some optimization techniques. Additionally, we also discuss the use of statistical  
50 mechanical ensembles for finding minima on the PES.

51 2.2 POTENTIAL ENERGY SURFACES

52 A PES simply describes the potential energy of the system as a function of all its  
53 relevant coordinates in phase space, essentially providing a mapping  $\mathbb{R}^n \rightarrow \mathbb{R}$ , where  $\mathbb{R}$   
54 is the set of real numbers and  $n$  is the number of positional parameters in the system.  
55 Usually these coordinates are the positions of the atoms  $q$  and their conjugate the

56 momenta  $p$ . Note that there could be more variables associated with the system,  
 57 for instance the magnetic moments of the atoms could play a role in describing the  
 58 system. In this magnetic system there would be positional variables for the atom-wise  
 59 spin vectors and their "momenta". Application of the term "momenta" might seem  
 60 odd here, as the magnetic spin does not have a mass or a velocity. However, since the  
 61 magnetic "position" is defined on the PES we need to describe its conjugate variable  
 62 to properly formulate Hamiltonian dynamics and the kinetic portion of the PES.

## 63 Experimentally Derived Potential Energy Surfaces

64 Generally PESs are obtained from purely computational experiments including: ab-  
 65 initio DFT, classical approximations via the embedded atom method, or even param-  
 66 eter driven models with experimentally fitted parameters. However, one can derive  
 67 a PES from an experiment which describes how well the model reproduces the ex-  
 68 perimental data. In this case one needs a theoretical and computational framework  
 69 mapping the atomistic variables of the simulation to the same space of the data ob-  
 70 tained from the experiment. This allows the experiment to be compared directly  
 71 against the predicted data via an experimentally derived PES.

## 72 Potentials

73 For an experiment which produces 1D data, like powder diffraction, EXAFS or XPS,  
 74 the implemented potentials are:

$$\chi^2 = \sum_{a=a_{\min}}^{a_{\max}} (A_{\text{obs}} - \alpha A_{\text{calc}})^2 \quad (2.1)$$

$$75 \quad R_w = \sqrt{\frac{\sum_{a=a_{\min}}^{a_{\max}} (A_{\text{obs}} - \alpha A_{\text{calc}})^2}{\sum_{a=a_{\min}}^{a_{\max}} A_{\text{obs}}^2}} \quad (2.2)$$

$$76 \quad \chi^2_{\text{INVERT}} = \frac{1}{N} \sum_j \sum_r [A_{\text{obs}}(r) - \alpha A_{j,\text{calc}}(r)]^2 \quad (2.3)$$

77

$$\alpha = \frac{\sum_{a=a_{\min}}^{a_{\max}} A_{\text{obs}} A_{\text{calc}}}{\sum_{a=a_{\min}}^{a_{\max}} A_{\text{calc}}^2} = \frac{\vec{A}_{\text{obs}} \cdot \vec{A}_{\text{calc}}}{|\vec{A}_{\text{calc}}|^2} \quad (2.4)$$

78

79 Put in the definition of  $Rw$ 

80 where  $A_{\text{calc}}$  and  $A_{\text{obs}}$  are the calculated and observed 1D experimental data and  
 81  $A_{\text{calc},j}$  is the calculated data for a single atom interacting with the other atoms of the  
 82 system. Note that  $A_{\text{calc}}$  has a dependence on  $q$ , the positions of the system.

83 The  $Rw$  and  $\chi^2$  potentials have been reported numerous times. [46, 35, 7, 36, 48]  
 84 Essentially these potentials measure the least squares distance between the observed  
 85 scattering and the predicted scattering providing a way to quantify the agreement  
 86 between the model and experiment. While  $Rw$  and  $\chi^2$  are now standard in the PDF  
 87 community, the INVERT potential is fairly new and aims to incorporate descriptions  
 88 of the structural symmetry into the PES. [10, 11] In the case of the INVERT poten-  
 89 tial NMR or other symmetry sensitive data is used to describe the number of unique  
 90 atomic coordinations. This is then used to describe the number of unique atom-wise  
 91 pair distribution functions, thus causing systems with more or less unique coordi-  
 92 nation environments to be higher in energy. This approach has been shown to be  
 93 useful for  $C_{60}$  and other systems which are highly symmetric, creating a PES with an  
 94 easier to find minima. [10, 11] However, many times this kind of data is unavailable  
 95 when refining the structure causing the potential to be less useful. Additionally, this  
 96 potential introduces an element of user bias as the refiner must decide, based on some  
 97 spectroscopic data, how many unique environments are in the material. This bias  
 98 could be removed by using one of the other potentials with a method for simulat-  
 99 ing the observed spectra, allowing the computational system decide what structures  
 100 properly reproduce all the observed data.

101 **Forces**

$$\vec{\nabla}\chi^2 = -2 \sum_{a=a_{\min}}^{a_{\max}} (\alpha \frac{\partial A_{\text{calc}}}{\partial \gamma_{i,w}} + A_{\text{calc}} \frac{\partial \alpha}{\partial \gamma_{i,w}})(A_{\text{obs}} - \alpha A_{\text{calc}}) \quad (2.5)$$

$$\vec{\nabla}Rw = \frac{Rw}{\chi^2} \sum_{a=a_{\min}}^{a_{\max}} (\alpha \frac{\partial A_{\text{calc}}}{\partial \gamma_{i,w}} + A_{\text{calc}} \frac{\partial \alpha}{\partial \gamma_{i,w}})(\alpha A_{\text{calc}} - (A_{\text{obs}})) \quad (2.6)$$

$$\vec{\nabla}\chi^2_{\text{INVERT}} = \frac{-2}{N} \sum_{a=a_{\min}}^{a_{\max}} \sum_j (\alpha \frac{\partial A_{j,\text{calc}}}{\partial \gamma_{i,w}} + A_{j,\text{calc}} \frac{\partial \alpha}{\partial \gamma_{i,w}})(A_{\text{obs}} - \alpha A_{j,\text{calc}}) \quad (2.7)$$

$$\frac{\partial \alpha}{\partial \gamma_{i,w}} = \frac{(\sum_{a=a_{\min}}^{a_{\max}} A_{\text{obs}} \frac{\partial A_{\text{calc}}}{\partial \gamma_{i,w}} - 2\alpha \sum_{a=a_{\min}}^{a_{\max}} A_{\text{calc}} \frac{\partial A_{\text{calc}}}{\partial \gamma_{i,w}})}{\sum_{a=a_{\min}}^{a_{\max}} A_{\text{calc}}^2} \quad (2.8)$$

105 where  $\gamma_{i,w}$  is the  $i$ th arbitrary positional variable in the  $w$ th direction. The concept  
 106 of an "arbitrary positional variable" might seem a bit cumbersome but it allows us  
 107 to define the forces for any atomic parameter which can be represented as a vector  
 108 in 3-space. This comes in handy when trying to define the forces acting on variables  
 109 like anisotropic displacement parameters or atomic magnetic spins.

110 **2.3 ENSEMBLES**

111 While PESs describe which atomic configurations are the most desirable and how  
 112 the atoms would like to get there, the ensemble describes how the atoms move on  
 113 the PES. The abstraction of the PES from the ensemble is an important one, as it  
 114 allows for the reuse and exchange of both PESs and ensembles for a wide array of  
 115 problems. Statistical mechanical ensembles can be described in two ways, analytically  
 116 and scholastically. For long simulation times and fine enough numerical or analytical  
 117 integration these two descriptions should be identical.

118 In either case one starts by defining the Hamiltonian,  $\mathcal{H}$ , as the total energy of  
 119 the system. Thus, the Hamiltonian is described as the sum of the potential  $U(q)$  and  
 120 kinetic  $K(p)$  energies, where  $q$  is the positions of the atoms and  $p$  is their momenta

$$\mathcal{H}(q, p) = U(q) + K(p) \quad (2.9)$$

121 where  $K(p) = \frac{1}{2} \sum_i \frac{p_i^2}{m_i}$  and  $i$  denotes the  $i$ th particle.

122 Analytically one generally defines a partition function, which describes the sum  
123 of probabilities over all potential atomic states.

$$\Xi = \sum_i P_i(q, p) \quad (2.10)$$

124 where  $P_i$  is the probability of the  $i$ th state and is a function of the total energy of  
125 that state. This partition function can then be used to obtain the probability of any  
126 specific state. The relationship of the probability of a state to the state's energy and  
127 other properties depends on the ensemble being used.

128 For the canonical ensemble the partition function is probability is:

$$Q(N, V, T) = \exp\left(\frac{-\mathcal{H}(q, p)}{k_b T}\right) \quad (2.11)$$

129 where  $k_b$  is the Boltzmann constant and  $T$  is the temperature of the system. [37]

## 130 Monte Carlo Modeling

131 Monte Carlo can be used to simulate a statistical mechanical ensemble which can not  
132 be solved analytically. In most Monte Carlo systems the ensemble is simulated by  
133 randomly changing one of the system parameters and comparing the energy of the  
134 new system against the energy of the old system. If the energy of the new system is  
135 lower than the current energy then the new configuration is accepted. Otherwise the  
136 new system is rejected unless

$$\exp\left(\frac{-\Delta E}{E_T}\right) < u \quad (2.12)$$

137 where  $u$  is a random number  $[0, 1)$  and  $E_T$  is the thermal energy characteristic to the  
138 system. The ability of Monte Carlo modeling to accept “bad” moves allows the system  
139 to hop out of local energy minima during the search for the global minimum. Reverse  
140 Monte Carlo (RMC) is similar to Monte Carlo except it uses  $\chi^2$  as the PES.[36]

141 Despite the utility of RMC, and its wide use in the x-ray scattering community, as  
142 Hoffman and Gelman state “Not all MCMC [Markov Chain Monte Carlo] algorithms

143 are created equal".[24] RMC, similar to standard Monte Carlo simulations, samples  
 144 from the PES at random, usually by translating atoms in the system randomly. This  
 145 creates a less efficient, random walk based, exploration of the PES.[24, 38] Thus,  
 146 methods for suppressing this random walk nature, while still searching the potential  
 147 energy surface fully are needed.

## 148 Hamiltonian Monte Carlo

149 Hybrid or Hamiltonian Monte Carlo (HMC) can help to address some of these issues.  
 150 HMC was developed originally in the lattice quantum chromodynamics community  
 151 and provides a more efficient, more scalable approach to PES sampling for Monte  
 152 Carlo.[15, 39] In HMC the PES is explored using Hamiltonian dynamics, essentially  
 153 following the gradient of the PES to find more acceptable configurations.

In order to model dynamics we need to describe the motion of the particles in our system, thus:

$$\frac{dq_i}{dt} = \frac{\partial \mathcal{H}}{\partial p_i} = p_i \quad (2.13)$$

$$\frac{dp_i}{dt} = -\frac{\partial \mathcal{H}}{\partial q_i} = -\vec{\nabla}U \quad (2.14)$$

Using these equations we can derive the position and momentum vectors at any point in time using the leap-frog algorithm:

$$p_i(t + \delta t/2) = p_i(t) - \frac{\delta t}{2} \frac{\partial}{\partial q_i} U(q(t)) \quad (2.15)$$

$$q_i(t + \delta t) = q_i(t) + \delta t * p_i(t + \delta t/2) \quad (2.16)$$

$$p_i(t + \delta t) = p_i(t + \delta t/2) - \frac{\delta t}{2} \frac{\partial}{\partial q_i} U(q(t + \delta t)) \quad (2.17)$$

154 Note that  $\frac{\partial}{\partial q_i}$  is the gradient with respect to  $q$  where  $i$  denotes the  $i$ th atom being

155 moved. Using this notation the gradient is

$$\vec{\nabla}U = \begin{bmatrix} \frac{\partial U}{\partial q_{0,x}} & \frac{\partial U}{\partial q_{0,y}} & \frac{\partial U}{\partial q_{0,z}} \\ \vdots & \frac{\partial U}{\partial q_{i,w}} & \vdots \\ \frac{\partial U}{\partial q_{n,x}} & \frac{\partial U}{\partial q_{n,y}} & \frac{\partial U}{\partial q_{n,z}} \end{bmatrix} = \begin{bmatrix} \vec{\mathcal{F}}_0 \\ \vdots \\ \vec{\mathcal{F}}_i \\ \vdots \\ \vec{\mathcal{F}}_n \end{bmatrix} \quad (2.18)$$

156 where  $\frac{\partial}{\partial q_{i,w}}$  is the derivative with respect to  $q$  where  $w$  denotes direction of the deriva-  
 157 tive ( $x$ ,  $y$ , or  $z$ ),  $n$  is the number of atoms and  $U$  is the potential which depends on  $q$ ,  
 158 and  $\vec{\mathcal{F}}_i$  is the "force" on the  $i$ th atom. Using these equations new potential configura-  
 159 tions are proposed from the PES. These proposals are checked against the standard  
 160 Metropolis criteria discussed above, except that the change in potential energy  $\Delta E$   
 161 is replaced with the change in the Hamiltonian  $\Delta\mathcal{H}$ . Note that while this sampling  
 162 closely simulates the canonical ensemble, it is not exactly the same. Usually the  
 163 canonical ensemble is formulated as microcanonical ensembles in contact with an in-  
 164 finite heat bath at a given temperature, or a set of microcanonical ensembles which  
 165 exchange thermal energy. However, the HMC ensemble presented here has a momen-  
 166 tum bath instead of a temperature bath. One could imagine the atoms sitting in a  
 167 simulation box which has walls which can toggle their thermal exchange. Initially the  
 168 box starts in the momentum bath, allowing the atoms to come to equilibrium with  
 169 the bath momentum. The box is then removed from the bath causing it to become  
 170 adiabatic. Hamiltonian dynamics are then propagated inside the box, essentially run-  
 171 ning a microcanonical simulation. Once the dynamics are finished the energy of the  
 172 system is checked with the Metropolis criteria and the box is reintroduced to the  
 173 momentum bath and the process starts again.

174 **No-U-Turn Sampling**

175 Two parameters must be specified in HMC simulations, the step size  $\delta$  and the number  
176 of steps  $N$ . The step size is critical to the stability of the fitting procedure: with  
177 a too small  $\delta$  the simulation runs inefficiently producing structures too close to the  
178 previous, whereas with a too big  $\delta$  the linear approximation for the forces breaks  
179 down and often the simulated NP explodes. The number of steps to take during the  
180 dynamics is equally important and an inappropriate choice may result in backtracking  
181 or random walk characteristics in the simulations. In this work, we employ the No-  
182 U-Turn Sampling (NUTS) method recently proposed by Hoffman and Gelman to  
183 address this issue [24]. In the NUTS method  $\delta$  and  $N$  are dynamically computed  
184 by examining the ratio of accepted to rejected configurations as well as whether  
185 or not the simulation has started to take a U-turn. The U-Turn criteria makes  
186 certain that the simulation stops when it begins to backtrack, preventing excess  
187 computation on configurations that have very little new information to offer. The  
188 use of NUTS leaves us with two simulation parameters: the simulation temperature  
189 and the target acceptance. Hoffman and Gelman have empirically shown that the  
190 ideal target acceptance, which governs the dynamics time steps, is .65, which we have  
191 used for all of the simulations here. The simulation temperature sets the magnitude  
192 of the random starting momenta for the atoms at the beginning of each dynamics  
193 run [24].

194 **Grand Canonical Ensemble**

195 While NUTS-HMC simulations provide a system to find minima on PESs, the sim-  
196 ulation is fundamentally run in the Canonical Ensemble thus the variables in the  
197 simulation are limited to a fixed number of particles, simulation volume, and thermal  
198 energy. Fixing the thermal energy and simulation volume is not a problem, as they  
199 are not variables of interest in the final structure. However, specifying the number of

200 atoms in the system can be problematic, as the exact number of atoms in a sample  
201 can be difficult to count or a sample could have a distribution of particle sizes. Thus,  
202 a new ensemble needs to be used to allow the number of atoms to vary as a function  
203 of the PES. This new ensemble is the Grand Canonical Ensemble.

204 **Ensemble description**

205 In the Grand Canonical Ensemble (GCE) two sets of variables are allowed to change,  
206 the atomic positions, and the total number of atoms and their associated identi-  
207 ties. These two variables are controlled by temperature, or average momentum, and  
208 chemical potential. The partition function is

$$\Xi = \sum_{N=0}^{\infty} Q(N, V, T) \exp \frac{N\mu\beta}{T} \quad (2.19)$$

209 where  $Q(N, V, T)$  is the Canonical partition function discussed above,  $\mu$  is the chem-  
210 ical potential. [37] This is translated into a Monte Carlo system, producing Grand  
211 Canonical Monte Carlo (GCMC).

212 **Grand Canonical Monte Carlo**

213 While the probabilities for atomic motion are the same as in the Canonical Ensemble,  
214 the addition or removal of an atom have their own probabilities. For the addition of  
215 an atom the probability is formally:

$$\min[1, \frac{V}{(N+1)\Lambda(T)^3} e^{-\beta\Delta U + \beta\mu}] \quad (2.20)$$

216 Similarly the removal of an atom has the probability:

$$\min[1, \frac{(N)\Lambda(T)^3}{V} e^{-\beta\Delta U - \beta\mu}] \quad (2.21)$$

217 However, both of these equations depend of the overall simulation volume and the  
218 thermal wavelength, which is undesirable as these are not really properties that we  
219 are of interest to these simulations. Thus, we roll them into the definition of the

chemical potential, essentially setting the base chemical potential to counteract these effects. This makes certain that our simulation does not change if we change the overall cell volume. A GCMC move consists of creating a new atomic configuration, where an atom has been added or removed, and checking the above criteria. However, previous results have shown that this method is computationally expensive in dense liquids, and exceedingly expensive in solid materials. The long simulation times are due to the random nature of the atomic additions or removals which produce: over-tightly packed atoms, atoms in the middle of nowhere, or nonphysical vacancies. These configurations are rejected by the GCMC criteria but their probability of being sampled is much higher than configurations which are lower in energy, since the number of incorrect ways to add/remove atoms is much larger than the correct ways. Thus, we have implemented methods for biasing the atomic addition positions and the atomic removals toward configurations which are more likely to be accepted.

### 233 GCMC biasing

The basic idea of GCMC biasing is mapping, in 3 dimensions, where an atomic addition or removal is most likely to be accepted. Thus, the simulation volume is broken up into voxels, 3 dimensional volumes which are contained by the total simulation volume, with a pre-set size. Each voxel is given a probability of being chosen for a trial insertion where the probability is:

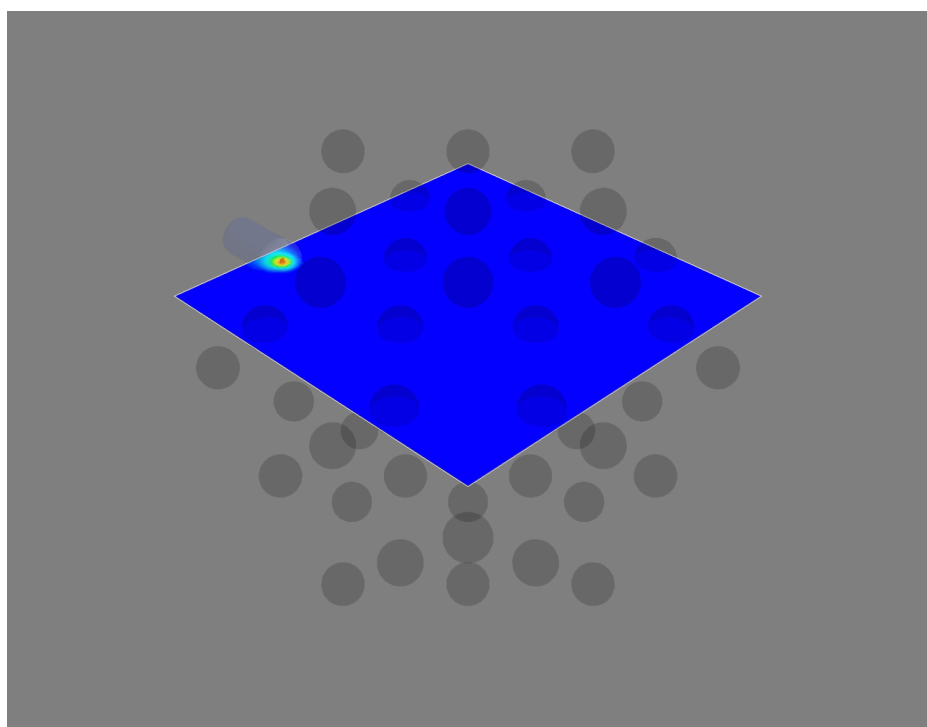
$$P_{i,j,k} = \frac{e^{\beta\Delta U_{i,j,k}}}{\sum_{i,j,k} e^{\beta\Delta U_{i,j,k}}} \quad (2.22)$$

where  $\Delta U_{i,j,k}$  is the change in energy. However, calculating  $\Delta U_{i,j,k}$  can be particularly expensive, especially when calculating scattering from atomic positions. The computational expense can be mitigated by using a cheaper potential, if only for the evaluation of the voxel energy, as previously shown. Similar to previous work we can use the Lennard Jones potential to approximate the addition potential, lowering the computational burden. [52]

245        Atomic deletion follows a similar biasing procedure, calculating the energy of each  
246    atom and biasing the probability of each atom to be chosen for removal by its energy.  
247    This way atoms which add the most energy to the system are more likely to be  
248    removed.

249        Figure 2.1a shows an example map for atomic addition in a Au54 atom system,  
250    with an Au55 atom target. Figure 2.1b shows the results of a few GCMC insertions  
251    with biasing, showing the focusing of the simulation on the missing atom. The high  
252    density of insertions around the missing atom would not have been possible without  
253    the biasing.

(a)



(b)

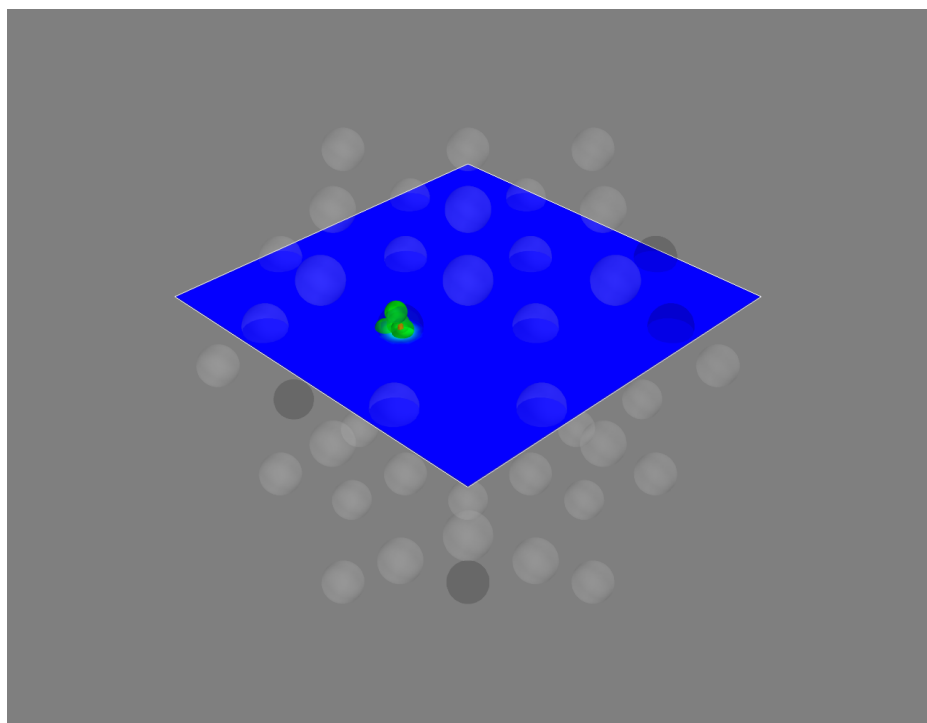


Figure 2.1: These figures show slices of the three dimensional addition potential energy surface. a) shows the addition probability, with the red area most probable. b) shows the results of trial insertions, where the green spheres denote where insertions were attempted.

254 2.4 CONCLUSIONS

255 In this chapter we have presented the development of both PES and the statistical  
256 mechanical ensembles used to search them. We expanded the classical concept of  
257 a PES to a more general mapping from positional variable space to energy space.  
258 This expansion allowed for the implementation of experimentally derived PES, where  
259 the disagreement between experimental and computed results can be included in the  
260 PES. Common experimental PESs were discussed, and their forces derived. The  
261 implementation of various statistical mechanical ensembles, used for searching the  
262 PES for minima, was also discussed with a special focus on No-U-Turn-Sampling  
263 Hamiltonian Monte Carlo. Grand Canonical Monte Carlo was also discussed, with  
264 an emphasis on the us of biasing to increase the overall acceptance rate. Future  
265 work in this area may include the development of PESs which leverage 2 dimensional  
266 data, like STEM images, or ensembles which help to eliminate tuned parameters like  
267 parallel tempering.

268

## CHAPTER 3

269

### ATOMIC PAIR DISTRIBUTION FUNCTION:

270

### THEORY AND COMPUTATION

271 

#### 3.1 INTRODUCTION

272 Atomistic structural insight is essential for understanding and controlling a mate-  
273 rial's properties and functions, which has led to some of the most exciting advances  
274 in modern materials science and engineering. X-ray diffraction techniques are one of  
275 the most powerful tools for probing atomic structures with ultimate precision. Tradi-  
276 tionally, thousands of diffraction peaks are analyzed using refinements of a structural  
277 model with few parameters to determine the 3D structure of bulk single crystals with  
278 high precision [21]. However, real engineered materials differ from ideal single crystals  
279 by showing a complexity in morphology, crystallite size, and atomic structure. The  
280 X-ray Powder Diffraction method (XPD) is among the most widely used methods  
281 for solving the structure of micro-crystals. The XPD technique utilizes hundreds of  
282 diffraction peaks and constrains the refinement of the structural model to few pa-  
283 rameters in order to resolve the structure [42]. Solving the atomic structure becomes  
284 difficult using traditional x-ray diffraction techniques when the size of the material or  
285 its important features is reduced to the nanometer scale with non-periodic or short-  
286 periodic atomic arrangements. Materials consisting of particles with sizes less than  
287 a few tens of nanometers, often called nanoparticles (NPs), are structurally more  
288 complex than their bulk cousins. This structural complexity is often attributed to  
289 the large number of surface atoms which have incomplete coordination spheres [53],

290 surface relaxation [25], and surface environment effects [47, 23, 34]. These effects  
291 make the precise determination of 3D atomic structure of NPs far more complicated  
292 and problematic [4].

293 Over the years many advances have been made to address the famous “nanostruc-  
294 ture problem”[4], for example, by using the atomic Pair Distribution Function (PDF)  
295 analysis of x-ray and neutron total scattering data [17, 40, 48], PDF analysis combined  
296 with molecular dynamics simulations [56, 22], bulk crystallography approaches [26],  
297 and others. Attempts with non-diffraction based approaches have also been made,  
298 including Transmission Electron Microscopy (TEM) [12], Raman spectroscopy[29],  
299 Extended X-ray Absorption Fine-Structure Spectroscopy (EXAFS)[20] and Nuclear  
300 Magnetic Resonance (NMR) [2].

301 In this chapter the PDF and its gradients will be derived. These expressions,  
302 when combined with the PES and statistical mechanical treatment from chapter 2,  
303 will allow for the solution of atomic structures. This chapter will also develop a  
304 computational framework for evaluating the PDF and its gradients using Graphical  
305 Processing Units (GPUs) to enable fast structural solution.

### 306 3.2 THEORY

307 To properly understand the PDF and its limitations we need to derive its mathemat-  
308 ics. The PDF has been previously derived many times so it is not re-derived here.  
309 This discussion of the PDF and its gradients use the notation of Farrow and Billinge.  
310 [18]

## 311 Derivation

312 Many of the above techniques require the gradient of the PES. This in turn requires  
313 the gradient of the PDF to be derived. Mathematically treating thermal vibrations  
314 will also be discussed in this section. Systems which are truly extended materials, like

315 powders with particle sizes larger than 10nm, are best formulated as systems with  
 316 periodic boundaries. Thus, the equations for a periodically bound PDF need to be  
 317 developed as well, with their gradients.

## 318 Analytically Gradients

319 Many optimization algorithms and simulations methodologies, including HMC, re-  
 320 quire not only the potential energy of a given configuration but also the forces acting  
 321 on that configuration. These forces are described by the gradient of potential energy  
 322 of the system which in turn requires the gradient of the PDF. As previously shown  
 323 the PDF is the Fourier Transform of the Debye equation. Since the Fourier Trans-  
 324 form is expressed as an integral we can exchange the order of the gradient and the  
 325 integral, allowing us to calculate the analytical gradient of the Debye equation and  
 326 Fast Fourier Transform (FFT) the resulting function. The Debye equation, with a  
 327 Debye-Waller vibrational correction is

$$F(Q) = \frac{1}{N\langle f \rangle^2} \sum_{j \neq i} f_i^*(Q) f_j(Q) \exp\left(-\frac{1}{2}\sigma_{ij}^2 Q^2\right) \frac{\sin(Qr_{ij})}{r_{ij}} \quad (3.1)$$

328 where

$$\sigma_{ij}^2 = (\vec{u}_{ij} * \hat{d}_{ij})^2 \quad (3.2)$$

$$\vec{u}_{ij} = \vec{u}_i - \vec{u}_j \quad (3.3)$$

$$\hat{d}_{ij} = \frac{\vec{d}_{ij}}{r_{ij}} \quad (3.4)$$

$$r_{ij} = \|\vec{d}_{ij}\| \quad (3.5)$$

$$\vec{d}_{ij} = \begin{bmatrix} q_{ix} - q_{jx} \\ q_{iy} - q_{jy} \\ q_{iz} - q_{jz} \end{bmatrix} \quad (3.6)$$

329 where  $Q$  is the scatter vector,  $f_i$  is atomic scattering factor of the  $i$ th atom, and  $r_{ij}$   
 330 is the distance between atoms  $i$  and  $j$  and has  $q$  dependence. [27]

331 state that the  $\vec{u}$  are the ADPs

332 For simplicity's sake we will break up  $F(Q)$  so that

$$F(Q) = \alpha \sum_{j \neq i} \beta_{ij} \tau_{ij} \Omega_{ij} \quad (3.7)$$

333 where

$$\alpha = \frac{1}{N\langle f \rangle^2} \quad (3.8)$$

$$\beta_{ij} = f_i^*(Q) f_j(Q) \quad (3.9)$$

$$\tau_{ij} = \exp\left(-\frac{1}{2}\sigma_{ij}^2 Q^2\right) \quad (3.10)$$

$$\Omega_{ij} = \frac{\sin(Qr_{ij})}{r_{ij}} \quad (3.11)$$

334 The derivatives are as follows:

$$\frac{\partial}{\partial q_{i,w}} F(Q) = \alpha \sum_j \beta_{ij} \left( \frac{\partial \tau_{ij}}{\partial q_{i,w}} \Omega_{ij} + \tau_{ij} \frac{\partial \Omega_{ij}}{\partial q_{i,w}} \right) \quad (3.12)$$

335 where

$$\frac{\partial \Omega_{ij}}{\partial q_{i,w}} = \frac{Q \cos(Qr_{ij}) - \Omega_{ij}}{r_{ij}^2} (q_{i,w} - q_{j,w}) \quad (3.13)$$

$$\frac{\partial \tau_{ij}}{\partial q_{i,w}} = \frac{\sigma_{ij} Q^2 \tau_{ij}}{r_{ij}^3} ((q_{i,w} - q_{j,w}) \sigma_{ij} - (u_{i,w} - u_{j,w}) r_{ij}^2) \quad (3.14)$$

336 Since  $\vec{u}_{ij}$  is a variable as well, we need the derivative with respect to it as well.

337 Thus

$$\frac{\partial}{\partial u_{i,w}} F(Q) = \alpha \sum_j \beta_{ij} \frac{\partial \tau_{ij}}{\partial u_{i,w}} \Omega_{ij} \quad (3.15)$$

$$\frac{\partial \tau_{ij}}{\partial u_{i,w}} = -\frac{\sigma_{ij} Q^2 \tau_{ij}}{r_{ij}} (q_{i,w} - q_{j,w}) \quad (3.16)$$

338 **Without ADPs**

339 Without ADPs the equations simplify down to

$$F(Q) = \frac{1}{N\langle f \rangle^2} \sum_{j \neq i} f_i^*(Q) f_j(Q) \frac{\sin(Qr_{ij})}{r_{ij}} \quad (3.17)$$

340 and

$$\frac{\partial}{\partial q_{i,w}} F(Q) = \alpha \sum_j \beta_{ij} \frac{\partial \Omega_{ij}}{\partial q_{i,w}} \quad (3.18)$$

341 use of these equations, when ADPs are not appropriate (like at cryogenic tempera-  
342 tures), greatly speeds up the computation.

### 343 Periodic Boundary Conditions

344 Periodic boundary conditions can be helpful when simulating extended solids or large  
345 nanoparticles. In this case all the non-crystallinity is contained within the simulation  
346 box and the box is repeated to create the longer distance peaks observed in the PDF.  
347 To perform this we can break up the Debye equation into two main parts, the part  
348 that describes the interatomic distances within the simulation box and those between  
349 boxes. Neglecting the thermal motion portion:

$$F(Q) = \frac{1}{N\langle f \rangle^2} \left( \sum_{j \neq i} f_i^*(Q) f_j(Q) \frac{\sin(Qr_{ij})}{r_{ij}} + \sum_{i,j} f_i^*(Q) f_j(Q) \frac{\sin(QR_{ij})}{R_{ij}} \right) \quad (3.19)$$

350 where

$$R = |\vec{r} + \vec{\nu}| \quad (3.20)$$

$$\vec{\nu} = \gamma_1 * \vec{a} + \gamma_2 * \vec{b} + \gamma_3 * \vec{c} \quad (3.21)$$

351 where  $\gamma_i$  is the number of copies of the simulation box in the  $i$ th direction, and  $\vec{a}, \vec{b}, \vec{c}$   
352 are the lattice or superlattice directions.

### 353 3.3 COMPUTATION

354 Simply deriving the equations for the PDF is not enough. The many body nature of  
355 the PDF equation make analytical solution of the structure from the PDF impossible.  
356 Thus, the PDF must be computed from a structural candidates and compared against  
357 experimental results to evaluate the reliability of the model. These computations were  
358 implemented using high performance or high throughput computing methods (HPC  
359 or HTC) and Graphical Processing Units to provide quicker solutions.

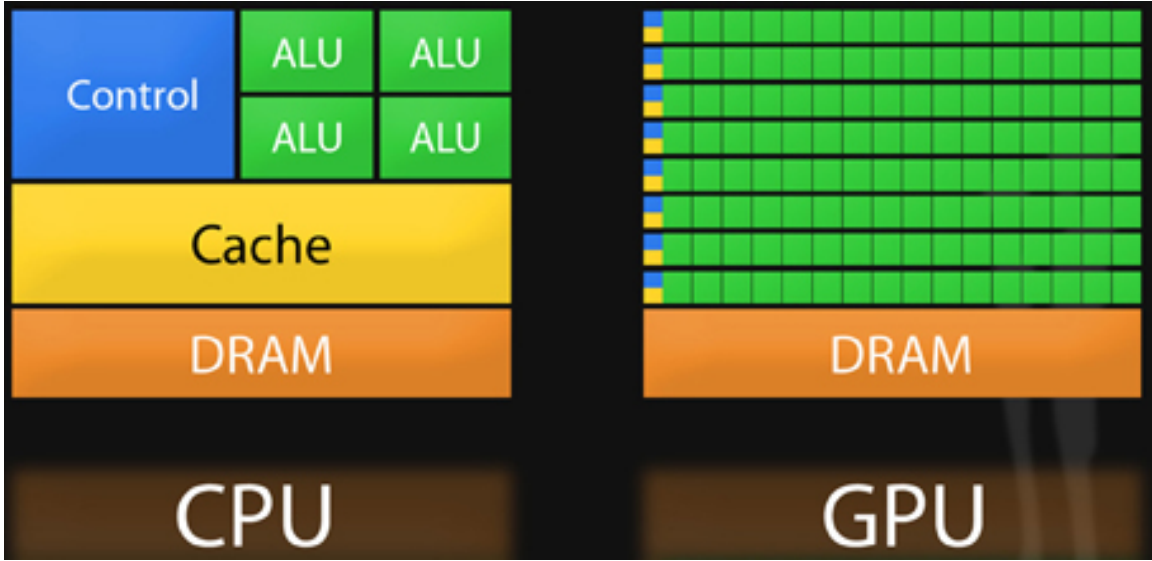


Figure 3.1: Comparison of the central processing unit (CPU) and GPU chip architectures from [6]. The arithmetic logic unit (ALU) are the arithmetic logic units which perform the mathematical operations, the dynamic random-access memory (DRAM) holds most of the data, although it is slower to access, the Cache holds rapidly accessed data, and the Control controls the execution of software. Note the greater number of ALUs on the GPU, the comparatively smaller cache, and the allocation of caches and controls to entire rows of processors.

## 360 HPC and GPUs

361 To properly solve the structure of materials the PDF will need to be computed many  
 362 times and checked against experimental results. This requires computation of the  
 363 PDF, potentially over many atoms. Calculating these PDFs requires a fast, highly  
 364 parallelized, computational framework.

## 365 GPUs and Parallelization

366 Computing the PDF is an embarrassingly parallel problem. The basic procedure is  
 367 to calculate the reduced structure factor  $F(Q)$  for each atom pair and momentum  
 368 transfer vector, sum over all the atom pairs, and Fourier transform the structure to  
 369 the PDF. The first part of this procedure is perfectly parallelizable, as each atom pair  
 370 is separate from the others. The summation over all the atomic reduced structure fac-

371 tors can be parallelized via distributed summing. Lastly the FFT can be parallelized  
372 using existing algorithms.

373 Graphical Processing Units (GPUs) are particularly well suited to the task of  
374 computing PDFs. GPU chip architecture is designed to perform many task simulta-  
375 neously by having potentially thousands of cores. Figure 3.1 show the comparison  
376 of CPU and GPU architectures. As the figure shows the GPUs have a very different  
377 layout of computational processors (ALUs) and memory. While each ALU is simpler  
378 on the GPU, requiring the instructions to be less demanding in terms of memory,  
379 there are many more of them. The greater number of processors allows each atomic  
380 pairing to be placed on its own processor, so long as the math can be broken into sim-  
381 pler operations. The equations are broken up on the GPUs into various pieces which  
382 correspond to the  $\alpha$ ,  $\beta$ ,  $\tau$  and  $\Omega$  as shown in equations 3.8-3.11 and sub-equations as  
383 needed. For example, while  $\beta$  is computed in one step,  $\Omega$  requires the computation  
384 of the displacement array, then the distance array and finally the  $\Omega$  array. The exact  
385 breakdown of processes, how the problems are broken down and spread across the  
386 processor has been optimized for speed and reliability.

387 **Map from ij space to k space**

388 The above equations, although formally correct, are very inefficient.  $F(Q)$  and its  
389 gradient are indexed over all the atoms twice, however there are symmetries that  
390 allow us to only compute over the atom pairs essentially mapping from an  $n \times n$  space,  
 $ij$  space, to a  $\frac{n(n-1)}{2}$  space,  $k$  space. For  $F(Q)$  we apply the following mapping where

$$\begin{array}{ccccc} E & \xrightarrow{\psi} & E' & \xrightarrow{\Sigma} & Z \\ \phi \downarrow & & & \nearrow \Sigma' & \\ B & \xrightarrow{\psi'} & B' & & \end{array}$$

391

392  $E$  denotes the atomic coordinates in  $ij$  space,  $E'$  denotes  $F(Q)$  before the summation  
 393 in  $ij$  space,  $B$  denotes the atomic pairs in  $k$  space,  $B'$  denotes  $F(Q)$  in  $k$  space, and  
 394  $Z$  denotes the final summed  $F(Q)$ . For the operators,  $\phi$  denotes the mapping from  
 395  $ij$  space to  $k$  space  $k = j + i * \frac{i-1}{2}$ ,  $\psi$  and  $\psi'$  denote the  $F(Q)$  operation in  $ij$  and  $k$   
 396 space, respectively.  $\Sigma$  denotes the sum over all the atoms.

397 To properly define  $\Sigma'$  we must establish whether  $F(Q)$  is an even function. We  
 398 can accomplish this by examining each of the portions of  $F(Q)$ ,  $\alpha, \beta, \tau, \Omega$ .  $\Omega$  is even,  
 399 since  $r_{ij}$  is the interatomic distance, which is the same despite a flip of indices,  $Q$   
 400 does not depend on the atomic indices, and since  $Qr_{ij}$  is even so is  $\sin Qr_{ij}$ . Thus,  
 401  $\Omega$  is even. Providing similar analysis to  $\tau$  we can see that while  $\vec{u}_{ij}$  is odd, so is  
 402 the unit displacement vector between the two atoms, thus the two odds cancel out.  
 403 Intuitively this makes sense, since the  $F(Q)$  equation is fundamentally interested  
 404 in the interatomic distances which is even. Thus, switching atom indices does not  
 405 change  $F(Q)$ . Due to the even nature of the  $F(Q)$  operator the  $\Sigma'$  operator sums  
 406 over all the atom pairs, and multiplies by two to reflect the double counting of the  $\Sigma$   
 407 operator.

For the gradient a similar mapping is used:

$$\begin{array}{ccccc}
 & & \psi & & \\
 E & \xrightarrow{\quad} & E' & \xrightarrow{\Sigma} & Z \\
 \phi \downarrow & & & \nearrow \tilde{\phi}\Sigma & \\
 B & \xrightarrow{\quad} & B' & &
 \end{array}$$

408

409 In this mapping, however, we use the  $\tilde{\phi}\Sigma$  operator. This operator simultaneously  
 410 performs a reverse mapping from  $k$  to  $ij$  space, and a summation with the correct  
 411 symmetry. In this case the  $\psi$  and  $\psi'$  operators, which denote the  $\vec{\nabla}F(Q)$  operator  
 412 in  $ij$  and  $k$  space, are antisymmetric. Intuitively this makes sense as an extension  
 413 of Newton's Second Law, since each particle's interaction is felt oppositely by its

414 partner.

## 415 GPU Memory Allocation

416 While GPUs are very fast computational engines they tend to be memory bound.  
417 While a gradient array for a 10nm Au nanoparticle, consisting of 31,000 atoms and  
418 half a billion unique distances, occupies 1.5 TB of memory a single GPU's RAM  
419 allotment varies from 4GB on a NVIDIA GTX970 to 24 GB on a NVIDIA Tesla K80.  
420 Thus, it is important to determine exactly how many atoms can fit on a GPU of  
421 arbitrary size as a function of the number of atoms and the  $Q$  range. The memory  
422 required per array is:

$$q[=]3n \quad (3.22)$$

$$d[=]3k \quad (3.23)$$

$$r[=]k \quad (3.24)$$

$$scatter[=]nQ \quad (3.25)$$

$$normalization[=]kQ \quad (3.26)$$

$$\Omega[=]kQ \quad (3.27)$$

$$F_k(Q)[=]kQ \quad (3.28)$$

$$Sum[=]kQ \quad (3.29)$$

$$Sum2[=]kQ \quad (3.30)$$

$$F(Q)[=]Q \quad (3.31)$$

423 where  $n$  is the number of atoms,  $k$  is the number of unique distances,  $Q$  is the scatter  
424 vector, and the  $[=]$  operator denote the number of single precision floating point  
425 values in memory. Each of the above arrays are used in the computation and thus  
426 must be able to be held in memory. Thus the number of atom pairs that can fit on

427 a GPU with  $am$  bytes of available memory is:

$$k_{perGPU} = \frac{1}{16Q + 16} (-4Qn - 4Q + am - 12n) \quad (3.32)$$

428 If ADPs are included in the calculation, then the following arrays are also added to  
429 the memory allocation:

$$adps = 3n \quad (3.33)$$

$$\sigma = k \quad (3.34)$$

$$\tau = kQ \quad (3.35)$$

430 Thus the pair allotment is:

$$k_{perGPU} = \frac{-4Qn - 4Q + am - 24n}{20Q + 20} \quad (3.36)$$

431 For the Gradient we need to calculate  $F(Q)$  and its gradient, so the total memory  
432 overhead is equal to the previously mentioned arrays plus:

$$\vec{\nabla}\Omega = 3kQ \quad (3.37)$$

$$\vec{\nabla}F_k(Q) = 3kQ \quad (3.38)$$

$$\vec{\nabla}F_n(Q) = 3nQ \quad (3.39)$$

433 Thus the gradient allotment is:

$$\vec{\nabla}k_{perGPU} = \frac{-16Qn + am - 12n}{32Q + 16} \quad (3.40)$$

434 For the gradient with ADPs the ADP gradient array is:

$$\vec{\nabla}\tau = 3kQ \quad (3.41)$$

435 Thus the allocation is:

$$\vec{\nabla}k_{perGPU} = \frac{-16Qn + am - 24n}{48Q + 20} \quad (3.42)$$

436 These equations were solved by sympy as their validity is very important to the overall  
437 reliability of the software. If the GPU is over allocated then the system may crash  
438 or return meaningless results.

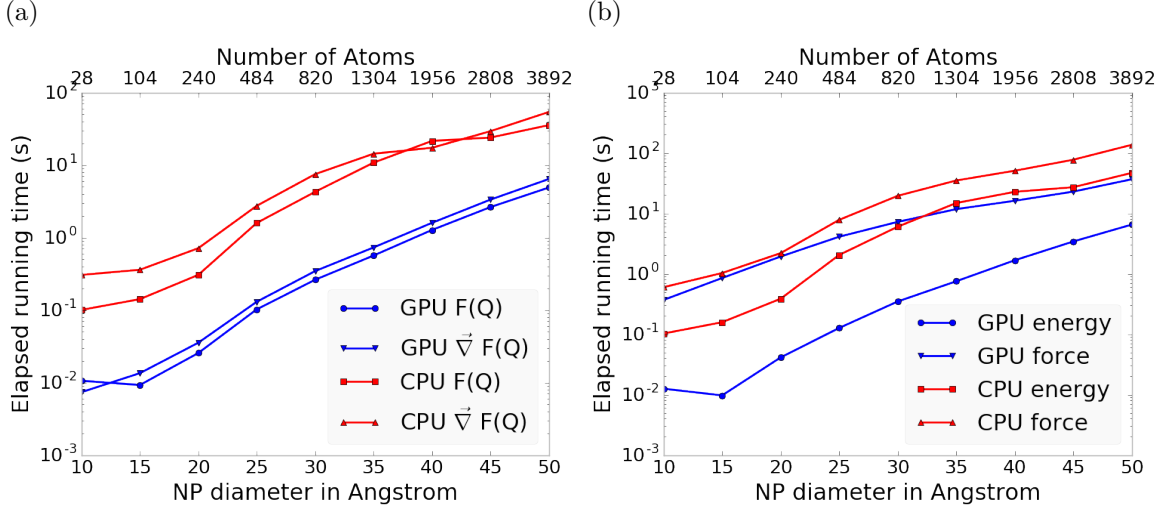


Figure 3.2: Speed comparison of CPU and GPU implementations. a) shows the time to compute the  $F(Q)$  by itself. b) shows the time to compute the  $Rw$  based energy for Au NPs of various sizes, which includes computing  $F(Q)$ , its FFT, and the  $Rw$ .

## 439 Speed and Scaling of PDF Computation

440 To understand exactly how much the GPUs speed up the computation of  $F(Q)$  and  
 441 the PDF a series of time studies were run Au nanoparticles of varying size. Figure  
 442 3.2 shows the results of these time studies. CPU and GPU calculations were carried  
 443 out on an Intel i7-4820K @3.70GHz Quad-Core and one NVIDIA GTX970s, respec-  
 444 tively. The  $F(Q)$  computations show a 100x to 10x speedup using the GPUs over  
 445 the CPUs. Additionally, the  $\vec{\nabla} F(Q)$  and  $F(Q)$  computations seem to have similar  
 446 computation time and scaling relationships on the GPU. This implies that the two  
 447 processes may have similar bottlenecks, most likely in the  $F(Q)$  computation work-  
 448 flow. This relationship is similarly preserved, although to a lesser extent, in the CPU  
 449 scaling.

450 Interestingly, the tight run time relationship between  $F(Q)$  and its gradient are  
 451 not preserved in the  $Rw$  based force calculations. While the energy calculations are  
 452 very similar to the  $F(Q)$  calculations in terms of run time, the GPU and CPU force  
 453 calculations are much closer, with the GPU calculations being much slower. This is

454 due to the force bottleneck being the  $3n$  FFT operations which must be performed  
455 on the  $\vec{\nabla}F(Q)$  array to produce the  $\vec{\nabla}\text{PDF}$  array. While the GPU is leveraged  
456 to perform the FFT, the data must be loaded off the GPU and back on, causing a  
457 potential slowdown. Larger systems of atoms were not tried as the CPU computation  
458 quickly becomes very slow. Even higher GPU speedup is expected on more advanced  
459 GPUs like the NVIDIA Tesla series.

460 3.4 CONCLUSIONS

461 In this chapter we developed the gradients of the PDF in the discrete and periodic  
462 boundary condition case. We also developed the computational implementation of  
463 the PDF equations. This implementation emphasized use of GPUs to compute the  
464 PDF and its gradient. The GPU software was further sped up by mapping the com-  
465 putation to atom pairs rather than atom by atom. Finally, the speed of the GPU  
466 implementation was checked against the CPU implementation via speed benchmark-  
467 ing.

468

## CHAPTER 4

469

## BENCHMARKS

470 4.1 INTRODUCTION

471 Having developed the ensemble, PES, and PDF mathematics in chapters 2 and 3 this  
 472 chapter will now benchmark the system to check its ability to produce reasonable  
 473 structures from PDFs. The benchmarks shown here are certainly not exhaustive, nor  
 474 are they even all the benchmarks run against the NUTS-HMC system. However,  
 475 they do provide a good window into the workings, limitations, and abilities of the  
 476 system.

477 The formation of NPs with both crystallographic and non-crystallographic struc-  
 478 tures [34] and with different chemical patterns [19] are well documented. For sim-  
 479 plicity, we chose monometallic Au clusters as benchmarks and considered two groups  
 480 of structures with different size and degrees of structural disorder in order to assess  
 481 the reliability and efficiency of our HMC method for solving atomic structures from  
 482 PDFs. The first group consists of  $\text{Au}_{55}$  clusters with different degrees of disorder,  
 483 including a crystalline cluster structure in  $O_h$  (Octahedral) symmetry, a structure  
 484 with a disordered surface, and an amorphous structure. The second group consists  
 485 of the crystallographically solved  $\text{Au}_{102}$  structure as in the  $\text{Au}_{102}\text{MBA}_{44}$  nanocrystals  
 486 [26, 33]. We used optimized structures from the Density Functional Theory (DFT)  
 487 as target structures and generated the corresponding PDF,  $G_{\text{obs}}$ , according to

$$G_{\text{obs}} = \frac{2}{\pi} \int_{Q_{\min}}^{Q_{\max}} Q[S_{\text{obs}}(Q) - 1] \sin(Qr) dQ \quad (4.1)$$

488 where  $S_{\text{obs}}$  is the target structure's structure factor. Since all the target structures

were optimized by DFT at zero Kelvin the target and model PDF profiles were calculated at zero temperature, with no atomic displacement parameters (ADPs). However, ADPs would have a considerable impact on the calculation of the PDF, especially for nanoparticles at non-zero temperatures.

## Target Setup

Spin-polarized DFT calculations were carried out using the Vienna ab initio simulation package (VASP) [32, 31] within the Perdew-Burke-Ernzerhof (PBE) exchange-correlation functional [43]. The projected augmented wave method [5] and a kinetic energy cutoff of 400 eV were used. Structural optimization was performed until the total energy and ionic forces were converged to  $10^{-6}$  eV and 10 meV/Å, respectively. The amorphous Au<sub>55</sub> structures were generated by simulated annealing using the classical embedded atom method potential [50]. Different annealing temperatures between 1200 K and 1670 K (bulk melting temperature of Au) were used and the thermally equilibrated structures were cooled down to 300 K before minimization at 0 K. Further optimization using DFT leads to total energies that vary within 1-2 eV among different amorphous structures and the lowest energy one was used as the target structure. The target structure of Au<sub>102</sub> was taken as the Au<sub>102</sub> core of the DFT-optimized Au<sub>102</sub>MBA<sub>44</sub> cluster [33].

All systems were solved using a PES which consists of a linear combination of  $Rw$ , the repulsive and attractive thresholded spring potentials. The total potential energy in the Hamiltonian in Eq. (2.9) is expressed as:

$$U(q) = U_{Rw}(q) + U_{\text{spring}}(q, R_{\min}) + U_{\text{spring}}(q, R_{\max}) \quad (4.2)$$

The thresholded spring potentials are based on those previously proposed on by Petersen [44], i.e.  $U_{\text{spring}}(q, r_t) = \frac{\kappa}{2} \sum_{i,j} (r_{i,j} - r_t)^2$  for all atomic distance  $r_{i,j}$  outside the bounds of the spring threshold  $r_t$ . The resulting restoring forces on the out-of-bound

513 atoms bring the system back within the bounds of the PDF,  $R_{\min}$  and  $R_{\max}$ , and  
514 therefore preventing the system from exploding or collapsing. Otherwise, incorrect  
515 solutions may result by having atomic pair distances out of the PDF bounds.  $\kappa$  is  
516 the spring constant in eV/Å and the  $Rw$  potential is converted from unitless to eV  
517 via multiplication by a conversion factor  $\lambda$ .

518 Whereas the choice of the absolute values of  $\lambda$  and  $\kappa$  is somewhat arbitrary, their  
519 relative values are important in determining which term in Eq. (4.2) dominates the  
520 PES, especially when considering the effect of the simulation temperature. Generally,  
521 the ratio between the total potential energy and the temperature determines how  
522 much random motion will dominate the dynamics; a lower ratio implies that random  
523 motion will play a large role in the dynamics. The ratio between  $\lambda$  and  $\kappa$  of each  
524 spring describes how far the PDF can push the system below or above the bounds set  
525 by the spring potentials. Heuristically, too stiff a spring forbids the system to access  
526 new configurations, e.g. high energy “transition states” which may involve shorter  
527 bonds or a larger system size. Conversely, too small a spring constant makes it slower  
528 for the system to snap back within bounds and may lead to an explosion or implosion  
529 of the system, leaving the dynamics to drift aimlessly.

## 530 Model Parameters

531 Unless otherwise stated, the PDFs of the target and starting structures were generated  
532 using Eqn. (4.1) with a step of  $\delta R = .01 \text{ \AA}$ ,  $Q_{\min} = 0.1 \text{ \AA}^{-1}$ ,  $Q_{\max} = 25.0 \text{ \AA}^{-1}$ .  $R_{\min}$   
533 and  $R_{\max}$  correspond to the first minimum before the first PDF peak and that after  
534 the last PDF peak, respectively, which ensure that the full meaningful region of the  
535 PDF is modeled. For each of the simulations, the Q resolution was calculated by

$$\delta Q = \frac{\pi}{R_{\max} + \frac{12\pi}{Q_{\max}}} \quad (4.3)$$

536 The HMC simulation was run with  $N = 300$  iterations, a target acceptance rate of

537 0.65, and an average starting momentum for each NUTS iteration of 10 eVfs/Å. Both  
538 repulsive and attractive spring potentials are used with  $\kappa = 200$  eV/Å and thresholds  
539 matching  $R_{\max}$  and  $R_{\min}$  of the PDF, respectively.  $\lambda = 300$  eV was used as conversion  
540 factor for  $Rw$ . Each simulation was run with a pair of NVIDIA GTX970 graphics  
541 cards, with one card partially occupied with desktop visualization.

542 4.2 STRUCTURAL SOLUTIONS

543 **Case I: crystalline Au<sub>55</sub>**

544 We first test our algorithm by solving the crystalline Au<sub>55</sub> (*c*-Au<sub>55</sub>) cluster structure  
545 from its PDF. The starting structure is taken as the bulk-cut cuboctahedron of Au<sub>55</sub>  
546 with a uniform bond length of 2.89 Å. Due to finite-size and surface effects, the DFT-  
547 relaxed cluster structure shows a distinctively different bond length distribution as a  
548 function of the bond's distance to the cluster center of mass, and therefore is difficult  
549 to model with a small box approach which assumes an identical unit cell throughout  
550 the whole system.

551  $R_{\min}$  and  $R_{\max}$  for this simulation were 2.45 Å and 11.4 Å, respectively, with  
552  $\delta Q = 0.24$  Å<sup>-1</sup>. The simulation ran for approximately 34 minutes, over a total of  
553 ~40 thousand configurations. The results are shown in Fig. 4.1.

554 The PDF, radial bond distribution, and bond angle distribution show good agree-  
555 ment between the target and final fitted structures, with a  $Rw$  of 0.3% whereas  $Rw$   
556 of the starting structure is as high as 44.8%. DFT calculations yield a total energy of  
557 the final structure very close to that of the target structure (within a few meV). The  
558 success in the fitting is largely attributed to the factor that the target structure is  
559 only locally (and mildly) disturbed from its bulk-like counterpart and therefore there  
560 is no need to overcome any high PES barriers to reach the correct solution. As shown  
561 below, the situation is rather different for much more disordered target structures.

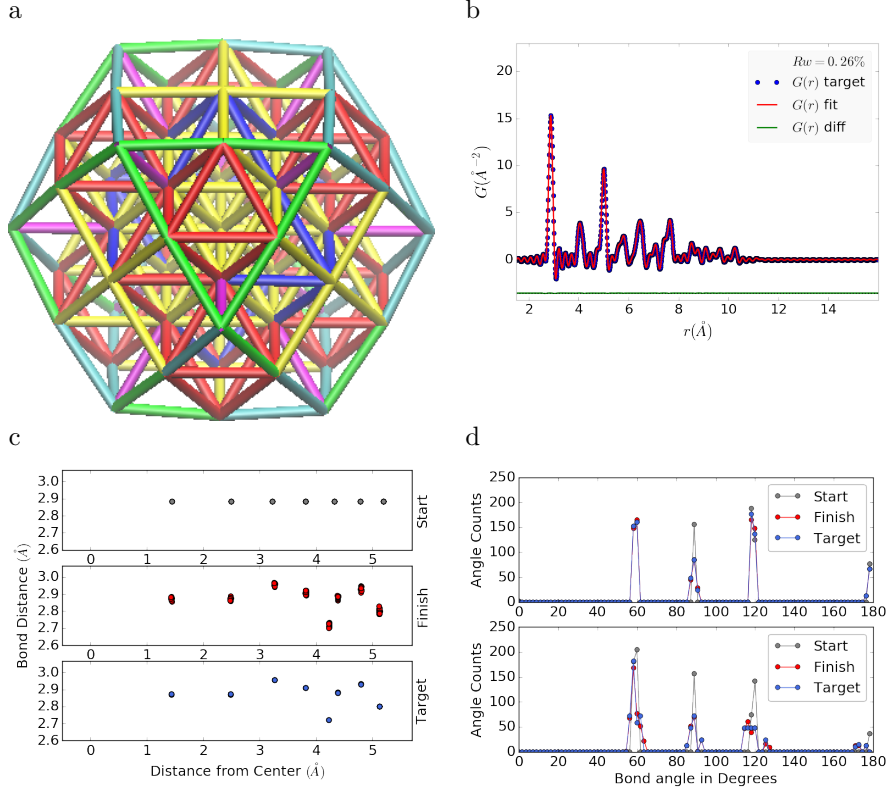


Figure 4.1:  $\text{Au}_{55}$  PDF fitting of DFT-optimized  $c\text{-Au}_{55}$ . a) the final structural solution ( $Rw=0.3\%$ ) with bond lengths color-coded by step of  $0.05\text{\AA}$ , b) the target PDF(blue dots) overlaid with the PDF of the final structure (solid red lines) with the difference in green lines offset below, c) the radial bond distribution, and d) bond angle distribution.

562 Interestingly, the small-box solution using PDFgui[17] yields a rather large  $Rw$  of  
 563 43%, due to the failure to fit the surface contracted atoms with a unit cell. The  
 564 PDF fits of the starting structure and small-box solution are shown in Fig. S1 in the  
 565 Supporting Information.

## 566 Case II: $\text{Au}_{55}$ with surface disorder

567 In addition to surface relaxation, the structure of a cluster or nanoparticle is often  
 568 disrupted by the presence of defects and/or ligand bound to the surface. To mimic  
 569 such surface disorders, we took the DFT-optimized  $c\text{-Au}_{55}$  structure from case I as  
 570 the starting structure and randomly displaced the surface atoms with a normal distri-

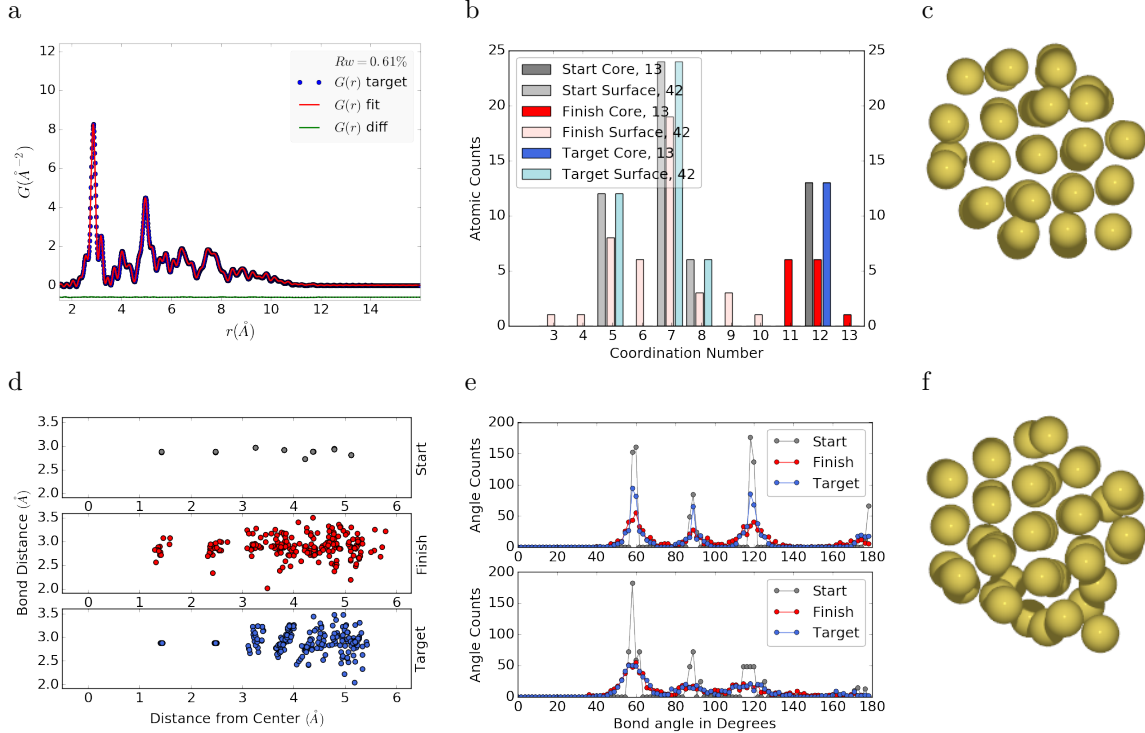


Figure 4.2:  $\text{Au}_{55}$  PDF fitting of surface-disordered  $\text{Au}_{55}$ . (a) the comparison of PDFs, (b) the CN distribution, (c) the target structure, (d) the radial bond distribution, (e) the bond angle distribution, and (f) the final structural solution ( $Rw=0.6\%$ )

571 bution of  $\sigma = 0.2 \text{\AA}$ . All atoms are allowed to move in the HMC simulation, including  
 572 the originally undisturbed core, which is a  $\text{Au}_{13}$  cluster with  $O_h$  symmetry.

573  $R_{\min}$  and  $R_{\max}$  for this simulation were  $1.95 \text{\AA}$  and  $12.18 \text{\AA}$ , respectively, with  
 574  $\delta Q = 0.23 \text{\AA}^{-1}$ . The simulation ran for approximately 3.6 hours, over a total of  $\sim 270$   
 575 thousand configurations. The results of the simulation are shown in Fig. 4.2.

576 Overall, good agreement is found between PDFs of the target structure and the  
 577 final structural solution, even out to larger  $r$ , with an  $Rw = 0.6\%$  starting from an  
 578  $Rw = 50.4\%$  (see Fig. S2). The radial bond distribution and angle distribution  
 579 show reasonably good agreement, but with lower degree of crystallinity in the final  
 580 structure compared to the target structure. The discrepancy is most obvious in  
 581 the core: despite the identical core structure in the starting and target structures,  
 582 the core atoms were displaced in the HMC simulations in order to achieve a “best”

583 solution. This is because PDF measures the global average of interatomic distances  
584 between each atomic pair and does not contain direct information about the locality  
585 of such pairs, e.g. on the surface or cores. If such information is obtained a priori, for  
586 example, from theoretical prediction or other experimental measurements, the core  
587 structure can then be fixed and excluded from HMC dynamics.

588 Similar discrepancies are found in the CN distribution. Since the initial displace-  
589 ments of the surface atoms are relatively mild, the interatomic connectivities remain  
590 more or less the same and therefore the target structure has an identical CN distri-  
591 bution to the starting (unperturbed) structure. This is, however, not the case for  
592 the final fitted structure, which shows discernible differences, especially at the low  
593 and high CN numbers. This is partly caused by the displacement of the core atoms  
594 mentioned above, and partly by the lack of CN constraints for the PDF fitting, which  
595 has been previously demonstrated in the case of  $\alpha$ -Si [10]. Additional experimental  
596 data, e.g. from EXAFS or NMR, may help to steer the simulations towards better  
597 agreement in both PDF and CN distribution.

### 598 Case III: amorphous Au<sub>55</sub>

599 Next, we turn to the case in which the entire cluster structure is disordered. We used  
600 a DFT-optimized amorphous Au<sub>55</sub> (*a*-Au<sub>55</sub>) as the target structure, and the DFT-  
601 relaxed *c*-Au<sub>55</sub> cluster from Case I as the starting structure. The total energy of  
602 *a*-Au<sub>55</sub> was computed to be *lower* than that of *c*-Au<sub>55</sub> by as large as 2.9 eV, consistent  
603 with the 3.0 eV found in previous DFT work [13].

604  $R_{\min}$  and  $R_{\max}$  for this simulation were 2.6 Å and 11.26 Å, respectively, with  
605  $\delta Q = 0.25 \text{ \AA}^{-1}$ . The simulation ran for approximately an hour, over a total of  $\sim 87$   
606 thousand configurations. The results of the simulation are shown in Fig. 4.3.

607 Our PDF fitting yielded a final structure of  $Rw$  of 1.7%, whereas that of the  
608 initial structure is as high as 76.1% (see Fig. S3 ), due to the drastically different

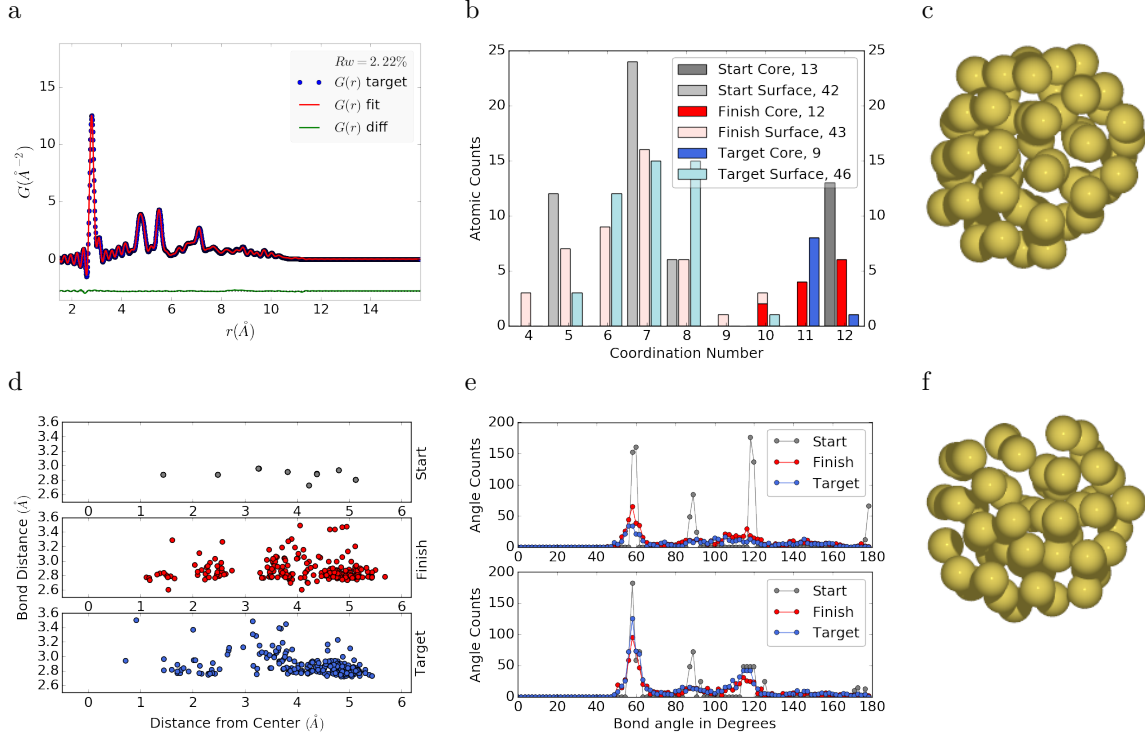


Figure 4.3: Similar to figure 4.2 for DFT-optimized amorphous  $\text{Au}_{55}$ .

609 atomic structure of the crystalline and amorphous  $\text{Au}_{55}$  clusters. Overall reasonable  
 610 agreement in PDF, bond angle distribution, and radial bond distance distribution  
 611 was found, and the wide spread of the bond lengths was qualitatively reproduced.  
 612 However, the mismatch in CNs is problematic, partly due to the lack of information  
 613 and/or constraints on the CNs. The total energy of the final structure is computed to  
 614 be  $\sim 6$  eV higher than that of the target structure and the difference is substantially  
 615 larger than the variation among different amorphous structures computed by DFT  
 616 ( $\Delta E_{\text{tot}} \sim \pm 1\text{-}2$  eV). Such a fitting result, despite the rather small  $Rw$ , clearly  
 617 indicates the importance of complementary information and/or constraints necessary  
 618 for reliably solving disordered NP structures from PDF.

619 **Case IV: ligand-protected Au<sub>102</sub>**

620 Our final benchmark is Au<sub>102</sub>, whose structure was initially solved by Jadzinsky and  
621 coworkers using x-ray crystallography [26] and further confirmed by DFT studies [33].  
622 The Au<sub>102</sub> structure consists of three main parts, a 49-atom Marks decahedron core,  
623 two  $C_5$  caps consisting of 20 atoms each, and 13 equatorial atoms. Unlike previous  
624 cases, the multi-symmetry nature of the structure, i.e. each part has its own distinct  
625 symmetry, poses a challenge for PDF-based solution of the structure. This is because  
626 of the atomically centralized nature of the PDF, in which each atom “sees” a density  
627 of other atoms surrounding it and has a strong tendency towards becoming the center  
628 of the main symmetry group. Such tendency may lead to a solution where some of  
629 the correct atomic symmetries are discarded in favor of the core symmetry.

630 **Starting from fcc structure**

631 The starting structure was generated by a spherical cut of the fcc bulk lattice, with  
632 two surface atoms removed to conserve the total number of Au atoms.

633  $R_{\min}$  and  $R_{\max}$  for this simulation were 2.7 Å and 16. Å, respectively, with  $\delta Q =$   
634 0.18 Å<sup>-1</sup>. The simulation ran for approximately two hours, over a total of ~82  
635 thousand configurations. The results of the simulation are shown in Fig. 4.4.

636 The initial structure of an fcc bulk-cut cluster, had a starting  $Rw$  of 77.6% (see Fig.  
637 S4), whereas the final structure has a  $Rw$  as low as 8.1%. The disagreement between  
638 the final and target PDFs shows that the majority of the error is in the high  $R$  region,  
639 which is related to the long range distances between the core, caps, and equatorial  
640 atoms. The agreement for other structural metrics is less satisfactory. The bond  
641 angle distribution for core atoms in the final structure has a poor correlation with  
642 those in the target structure, with much broader peak widths. This is likely caused  
643 by the high kinetic barrier to change from one high-symmetry core structure (fcc)  
644 to another (Marks Decahedron). In contrast, the bond angle distribution for surface

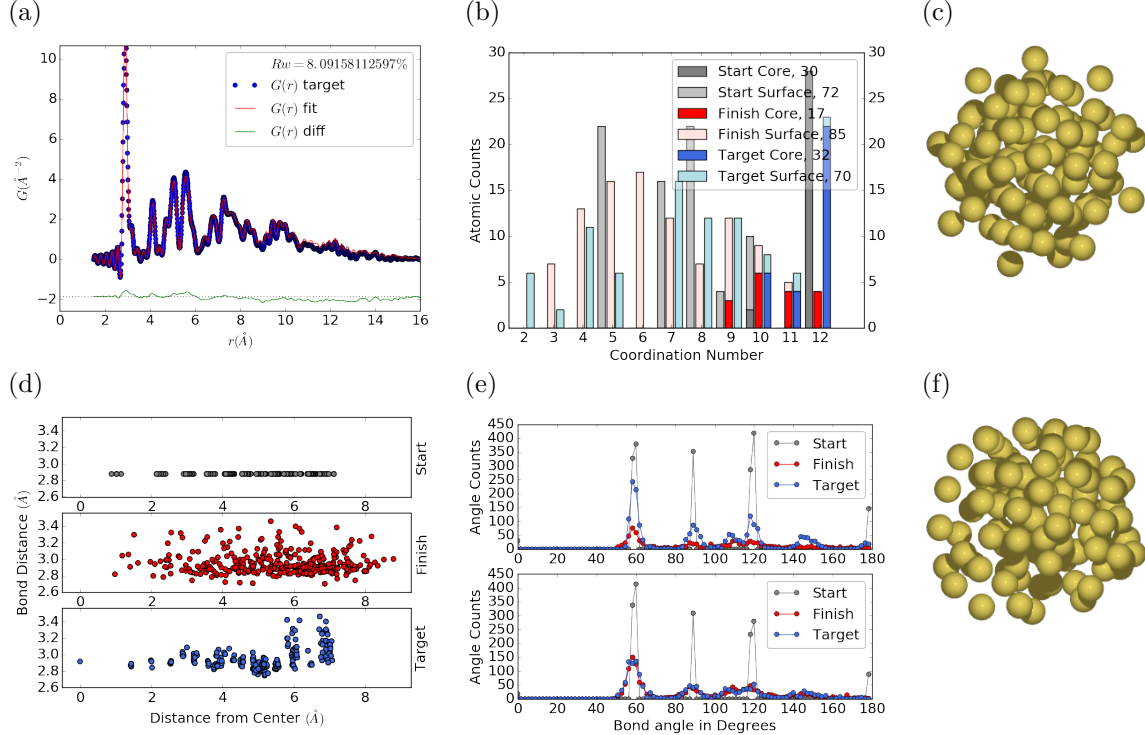


Figure 4.4: Similar to Fig. 4.2 for  $\text{Au}_{102}$  as in DFT-optimized  $\text{Au}_{102}\text{MBA}_{44}$  cluster.

atoms, which are of lower symmetry than the core, show a much better agreement.  
 This is due to the preference of Monte Carlo techniques for higher entropy, and thus  
 lower symmetry, structures. Similarly, the radial bond distance does not show the  
 correct clustering of bond lengths as expected from an ordered structure, indicating  
 the amorphous nature of our fit. Finally, the CN distribution shows the largest  
 discrepancy at  $\text{CN}=12$ , again due to the amorphous nature of the fit. Overall, the  
 structural metrics beyond the PDF indicate the poor agreement between the final  
 and target structures. A higher simulation temperature, potentially combined with  
 $\text{CN}$  or bond length aware potentials (such as DFT or EXAFS derived PESs) may  
 help to resolve this discrepancy.

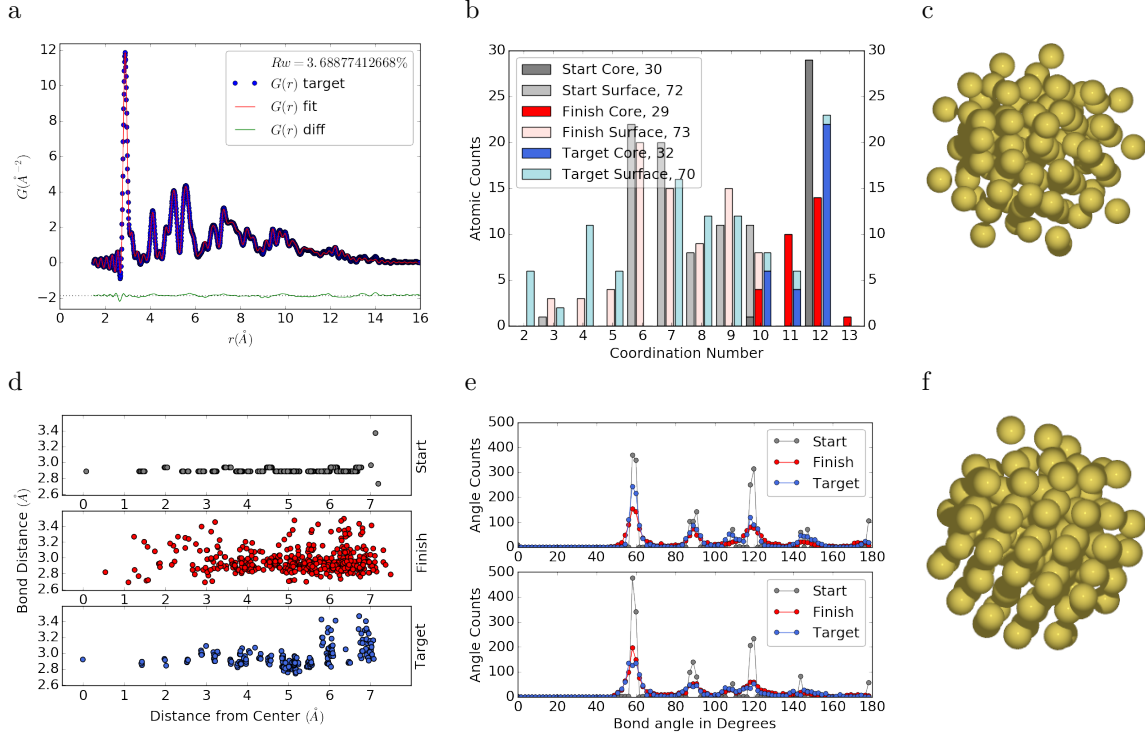


Figure 4.5: Similar to Fig. 4.4 with Marks decahedron as the starting structure.

## 655 Starting from Marks Decahedron

656 The starting structure, a Marks Decahedron, was generated by the ASE Cluster tool  
 657 with 2 atoms on the [100] face normal to the 5-fold axis, 3 atoms on the [100] plane  
 658 parallel to the 5-fold axis and, 1 atom deep Marks reentrance. This produced a  
 659 structure with 101 atoms which was extended by one more Au atom to fill out the  
 660  $\text{Au}_{102}$  structure.

661  $R$  bounds and Q resolution were the same as the previous case. The simulation  
 662 ran for approximately 2.5 hours over a total of  $\sim 90$  thousand configurations. The  
 663 results of the simulation are shown in Fig. 4.5.

664 The starting structure of Marks decahedron ( $Rw=56.6\%$ , see Fig. S5) yielded  
 665 a better structural solution, with a final  $Rw$  of 3.3%. However, the discrepancies at  
 666 high  $R$  remains as in the previous case. By examining the final structure, we can see  
 667 that these high  $R$  errors are due to a lack of the two 20-atom caps and 13 equatorial

668 atoms. Similarly, the radial bond distance distribution displays a diffusive behavior  
669 unlike the bond length clustering in the target structure. Compared to the previous  
670 case, the agreement in the CN and bond angle distributions are improved, with the  
671 latter capturing nearly all peaks in the target structure with the exception of the 110  
672 bond angle. Relatively large discrepancies are found in the CN distribution at the  
673 low and high ends.

674 4.3 DISCUSSION AND CONCLUSION

675 The challenge of NP structure determination from X-ray Diffraction stems from the  
676 absence of long range atomic ordering and the presence of non-trivial disordered  
677 structures. PDF data analysis is one of the successful experimental methods for  
678 solving NP structures, which has been tested on varieties of NP structures using  
679 non-crystallographic large box hybrid methods [46]. In this work, we developed a  
680 novel, HMC-based method to solve the structures of NPs from PDFs. We chose  
681 monometallic Au clusters as benchmarks and generated synthetic experimental PDF  
682 data from DFT-optimized cluster structures. Two cluster sizes ( $\text{Au}_{55}$  and  $\text{Au}_{102}$ )  
683 and different degree of disorders (crystalline, surface disordered, amorphous, ligand-  
684 protected) were considered, which pose further challenges in addition to the lack of  
685 long-range order in finite-size systems.

686 The quality of the PDF fit, as measured by the agreement factor  $Rw$ , is expected  
687 to provide a basis for the comparison between the fit structure and the target struc-  
688 ture. The HMC method is designed to find minima in the  $Rw$  PES and therefore the  
689 ultimate criterion for its success is the magnitude of the  $Rw$  values. This criterion has  
690 been met in the cases of surface relaxed  $c\text{-}\text{Au}_{55}$ , surface distorted-Au55, and  $a\text{-}\text{Au}_{55}$   
691 systems, where we obtained an excellent fits with  $Rw < 2\%$ . With most of the mod-  
692 eling methods a PDF fit with an  $Rw < 15\%$  would be considered a solved structure  
693 [46, 1, 35, 51, 45]. However, a low  $Rw$  does not necessarily translate into the correct

694 structural solution and the discrepancies may be caused by several different factors.  
695 For example, the disordered surfaces associated with NPs produces a fall off in the  
696 PDF profile, resulting in underestimated NP sizes in the fitted structures [46]. In ad-  
697 dition, as the PDF profile depends on the average core and surface pair distributions,  
698 the structural solution may not be unique especially for disordered systems. This is  
699 best manifested in the example of amorphous Au<sub>55</sub>, in which the final structure pro-  
700 duces a rather small  $R_w$  but has distinctively different structural features and a much  
701 higher total energy compared to the target structure. In order to faithfully solve the  
702 structures, other fitting metrics, such as the atomic coordination numbers, may need  
703 to be considered. For ordered or partially ordered systems, we have demonstrated  
704 a reasonable agreement between the final and target CN distributions, whereas the  
705 discrepancy increases for disordered structures. A hybrid HMC method combining  
706 with other experimental (EXAFS, NMR) or computational (DFT, force field) meth-  
707 ods is expected to provide more physical constraints, e.g. CN distribution, in the  
708 PDF fitting and result in better structural agreement.

709 The case of ligand-protected Au<sub>102</sub>, a crystallographically well solved NP system  
710 by X-ray diffraction, provides a unique test for the HMC algorithm due to its multi-  
711 symmetry nature and very short range ordering. The structure of Au<sub>102</sub> was solved  
712 using two different starting crystal structures, i.e. fcc and Mark decahedron. The  $R_w$   
713 values support the Marks decahedron structure of the cluster core over the fcc one,  
714 but discrepancies are found at high  $R$  values. This could be explained as limitation  
715 of the method while using PDF profile fit for high symmetry local structures such  
716 as cap atoms in Au<sub>102</sub>, which has a  $C_5$  symmetry. This is an intrinsic problem with  
717 the PDF, which measures the global inter-atomic distances, thus causing each atom  
718 to see itself at the epicenter of the majority symmetry. Use of additional techniques,  
719 like EXAFS, which has an emphasis on the local coordination spheres, may help  
720 with finding better minima by breaking the dominant symmetry and providing a low

721 energy path to compartmentalized structures.

722 In summary, we present the development of a novel Hamiltonian Monte Carlo  
723 based method for finding atomic structure solutions to PDFs. We derived the ana-  
724 lytical derivatives of  $Rw$ ,  $G(r)$ , and  $F(Q)$ , which were used to guide the Hamiltonian  
725 dynamics to follow the gradient of the PES towards minimum energies. The ma-  
726 trix element algebra inherent to the Debye sum and its derivatives lent itself to be  
727 written as GPU kernels, allowing for the speedup of the HMC algorithm by massive  
728 parallelization. The GPU implementation is 100 to 4x faster than the comparable  
729 multi-core CPU enabled code, depending on the size of the NP. The robustness and  
730 accuracy of the HMC method was benchmarked against a set of Au cluster struc-  
731 tures of different size and degree of disorder. Overall, low  $Rw$  values were obtained  
732 for all the benchmarks, with most of the structural features reproduced as shown by  
733 various structural metrics. The  $Au_{102}$  cluster, which contains both high symmetry  
734 local structures and disordered surface regions, posed the largest challenge. Although  
735 the fitted structure shows some dependence on two starting configurations, neither  
736 of them was able to fully solve the target structure. Future work which employs ex-  
737 perimentally derived potentials, including EXAFS, or computational potentials that  
738 contain chemical bonding information, may help to solve these particularly difficult  
739 cases. Work is underway to extend this method to the grand canonical ensemble and  
740 parallel tempering, which will allow for solving structures with unknown number of  
741 atoms and compositions and provide better stochastic mixing of structures.

742

## CHAPTER 5

743

# X-RAY TOTAL SCATTERING DATA ACQUISITION AND PROCESSING

745

## 5.1 INTRODUCTION

746 X-ray total scattering experiments are generally performed at synchrotron light sources,  
747 as only these sources can provide the needed flux, energy, and high momentum trans-  
748 fer vectors needed to obtain reliable PDFs. [9, 16] Despite the need for a dedicated  
749 facility to perform the total scattering experiments, the experiments themselves are  
750 fairly forgiving, allowing for reactive gaseous environments, experiment temperatures  
751 ranging from 2 K to 1800 K, and even electrochemical cycling. [8, 47, 49] The rapid  
752 PDF data acquisition associated with 2D area detectors creates a data management  
753 problem, as 96 hours of beamtime could result in almost 10,000 images which need  
754 to be associated with the experimental conditions and detector metadata. [9] Finally,  
755 all this data needs to be processed by masking bad pixels and regions, integrating  
756 azimuthally, and converting the scattering data to the PDF. [30, 28, 54, 41, 3]

757

## 5.2 DETECTOR $Q$ RESOLUTION

758 To properly azimuthally integrate the images taken from the detector the  $Q$  resolution  
759 of the pixels must be calculated. Azimuthal integration is the process of dividing the  
760 pixels up into “bins”. Each bin has a set width, usually in  $Q$ , which describes which  
761 pixels can go into the bin. During the integration process each pixel is placed into  
762 its corresponding bin. Finally a statistical measurement of the average of all the

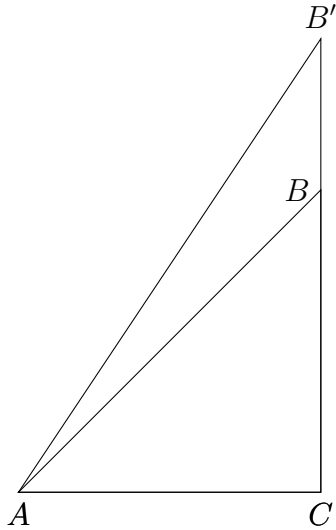


Figure 5.1: Scattering onto a flat detector

763 pixels in each bin is taken to produce the  $I(Q)$  data. Although commonly performed,  
 764 integrating using evenly spaced bins will cause pixels which are not on the same ring  
 765 to be binned together, causing the incorrect value of  $I(Q)$  to be obtained and a larger  
 766 standard deviation in the integrated data. To properly calculate the  $Q$  resolution  
 767 the resolution of each of the pixels in  $2\theta$  must be calculated. Figure 5.1 shows the  
 768 scattering of x-rays onto a flat image plate detector. In this diagram the bottom of the  
 769  $n$ th pixel is  $B$  while the top is  $B'$ . The resolution of this pixel in  $2\theta$  is  $\angle BAC - \angle B'AC$ .  
 770 Thus the resolution, calculated from the distances is

$$\Delta 2\theta = \arctan \frac{b}{d} - \arctan \frac{t}{d} \quad (5.1)$$

771 where  $d$  is the sample to detector distance ( $AC$  in figure 5.1),  $b$  is the distance to  
 772 the bottom of a pixel ( $CB$  in figure 5.1)), and  $t$  is the distance to the top of that  
 773 pixel ( $CB'$  in figure 5.1)). Note that these distances need to have been corrected for  
 774 detector tilt and rotation. Thus the resolution of a pixel in  $Q$  is

$$\Delta Q = \frac{4\pi(\sin \arctan \frac{b}{d} - \sin \arctan \frac{t}{d})}{\lambda} \quad (5.2)$$

775 where  $\lambda$  is the x-ray wavelength.

776 This effect is analogous to looking at windows on a very tall building. The windows  
777 are all the same size, but due to the nature of the perspective, the windows seem to  
778 shrink as one looks higher up the building.

779 For a Perkin Elmer image plate, like the one used at the NSLS-II's XPD and the  
780 APS's 11-ID-B, the resolution function is shown in 5.2. For the same detector the  
number of pixels per  $Q$  is shown in 5.3

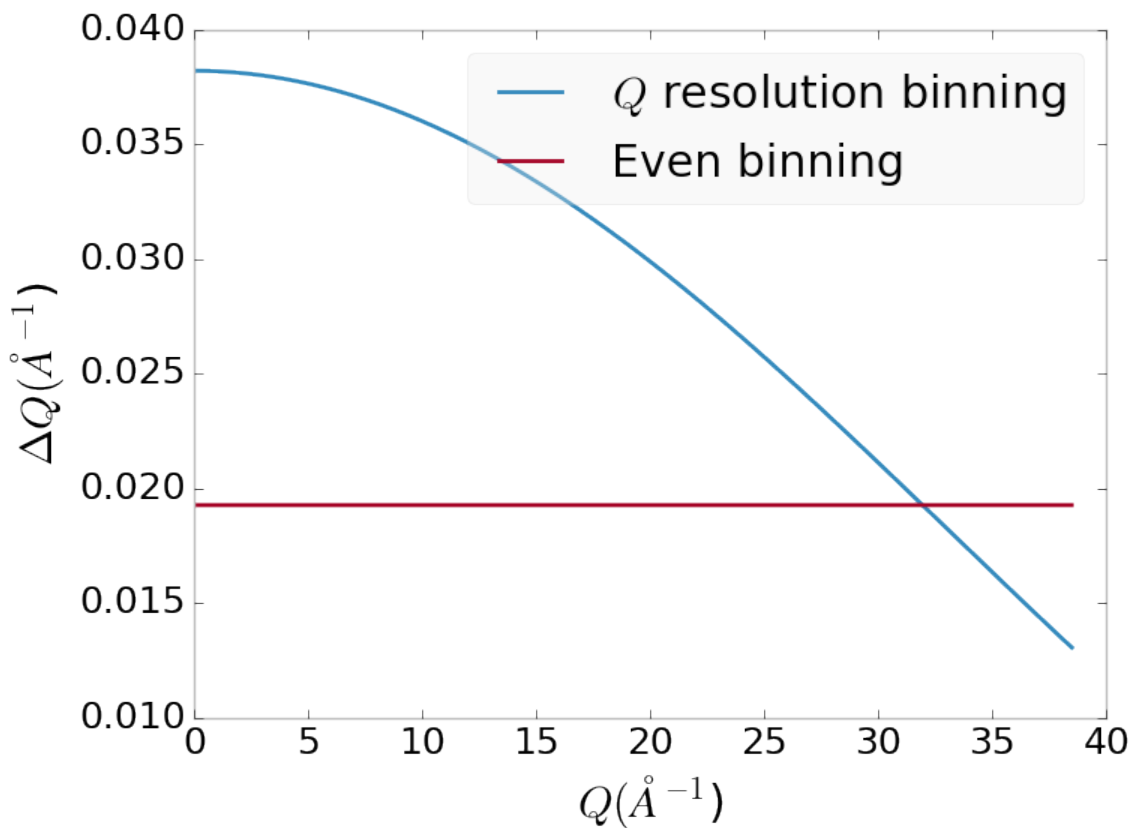


Figure 5.2:  $Q$  resolution as a function of  $Q$ .

781

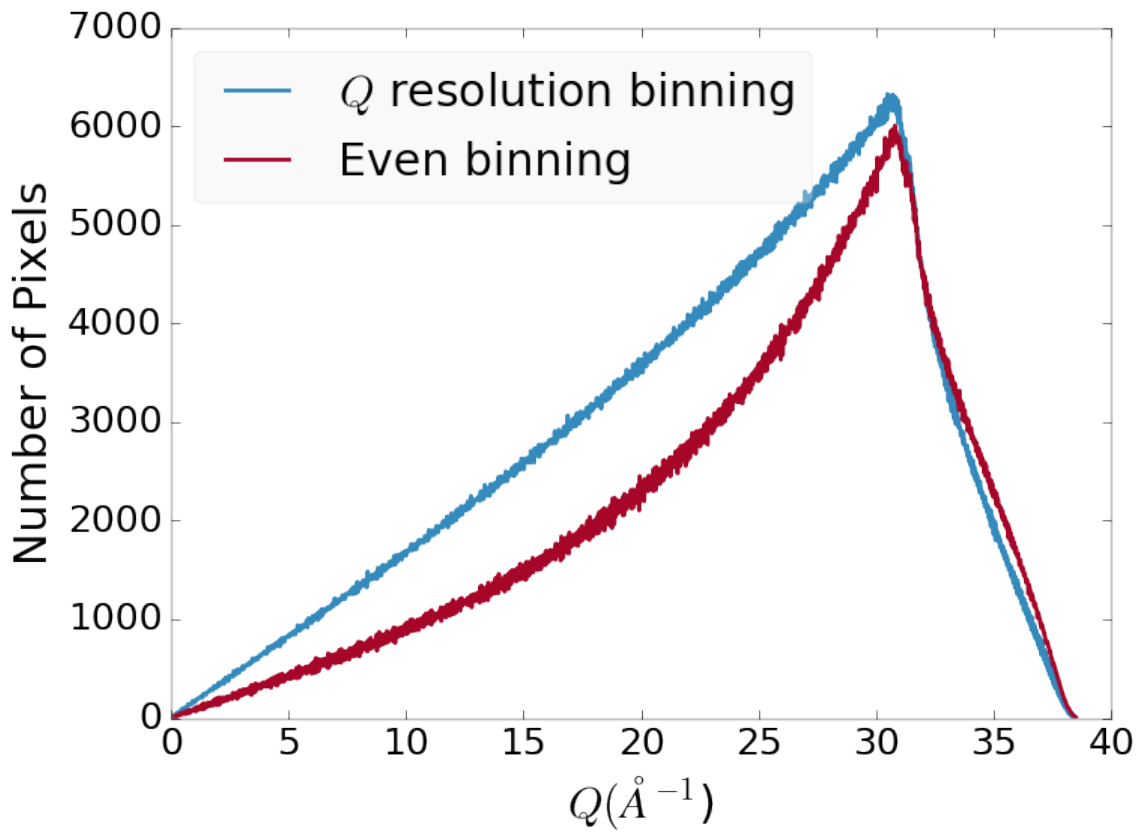


Figure 5.3: Number of pixels as a function of  $Q$ , binned at the  $Q$  resolution of the detector.

782 5.3 AUTOMATED MASK GENERATION

783 **Introduction**

784 Detector masking is an important part of any x-ray scattering workflow as dead/hot  
 785 pixels, streak errors, and beamstop associated features can be averaged into the data  
 786 changing the signal and its statistical significance. While some features, like the  
 787 beamstop holder, can be easily observed and masked by hand other are much more  
 788 difficult to observe even on large computer monitors. Additionally, while dead/hot  
 789 pixels and streaks are usually static the hot pixels associated with textured or sin-  
 790 gle crystal scattering or cosmic rays are not. Thus, coming up with an automated  
 791 method for finding such erroneous pixels is important, especially as high flux diffrac-

792 tion beamlines can generate data very quickly.

793 While this problem can be quite complex in the most general case, we can use the  
794 annular symmetry of the powder scattering pattern to our advantage, by comparing  
795 a pixel against pixels in the same ring. Since non-textured powder scattering should  
796 produce the same pixel intensity for a given ring we can mask any pixels which are  $\alpha$   
797 standard deviations away from the mean. This method relies on the aforementioned  
798 pixel binning algorithm, as using miss sized bins will cause some pixels which should  
799 be in separate rings to be put together, and others which should be in the same ring  
800 to be separated. In that case the masking algorithm will overestimate the number of  
801 pixels to be masked due to the additional statistical variation in the sample.

## 802 **Algorithm Design**

803 The masking algorithm procedure takes in the image and a description of the pixel  
804 positions in either distance from the point of incidence or in  $Q$ . The image is then  
805 integrated twice, producing both the mean  $I(Q)$  and the standard deviation of each  
806  $I(Q)$  ring. The mask is created by comparing the pixel values against each ring's  
807 standard deviation and threshold  $\alpha$ . Note that the threshold can be a function of  
808 distance from the point of incidence or  $Q$ .

## 809 **Test Cases**

810 To study the effectiveness of the masking we ran the algorithm against both simulated  
811 and experimental data. In the case of the simulated data four systems were created:  
812 1) dead/hot pixels with varying numbers of defective pixels, 2) beamstop holder with  
813 varying beamstop holder transmittance, 3) rotated beamstop holder with varying  
814 beamstop holder transmittance, and 4) beamstop holder with dead/hot pixels. The

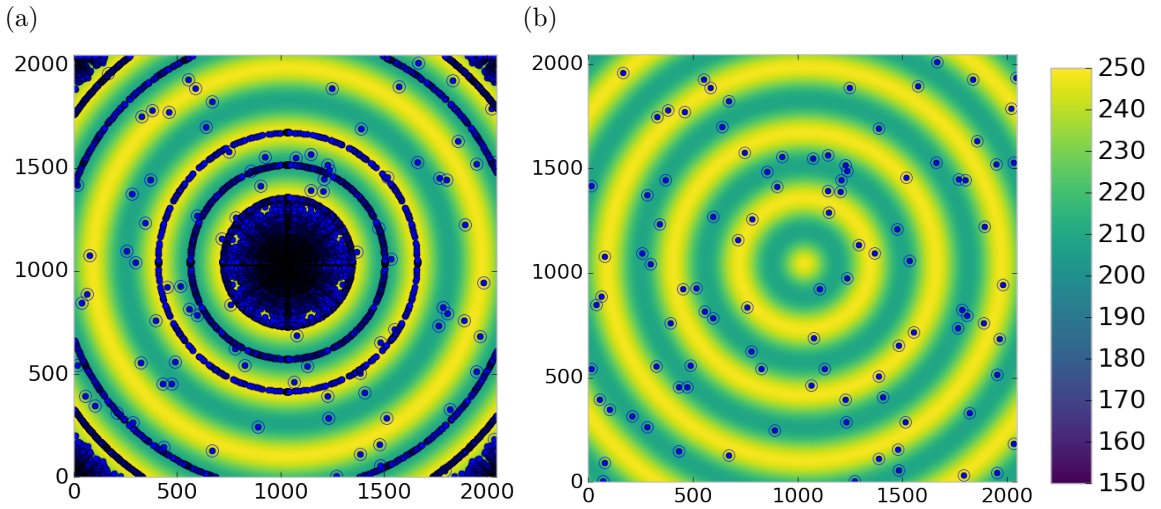


Figure 5.4: Generated dead/hot pixel masks for a detector with 100 bad pixels. a) the standard even bin mask and b) the  $Q$  resolution binned mask. The bad pixels are noted with open circles, masked pixels are noted with solid circles.

base scattering was produced by

$$I = 100 \cos(50r)^2 + 150 \quad (5.3)$$

where  $r$  is a pixel's distance from the beam point of incidence. The positions of the dead/hot pixels were chosen at random as was the dead or hot nature of the defect. Dead pixels had values from 0 to 10, while hot pixels had values from 200 to 255. The beamstop was positioned at the vertical center of the detector with an initial width of 60 pixels and final width of 120 pixels. The height of the beamstop was 1024 pixels. The beamstop was calculated to attenuate the x-ray scattering signal at various transmittance, as various beamstop holder materials have different transmittance. Two versions of the masking algorithm were run for each test case, one using the standard even bin sizes for the integration step, and one where the bin sizes are tuned to the pixel  $Q$  resolution as discussed in 5.2.

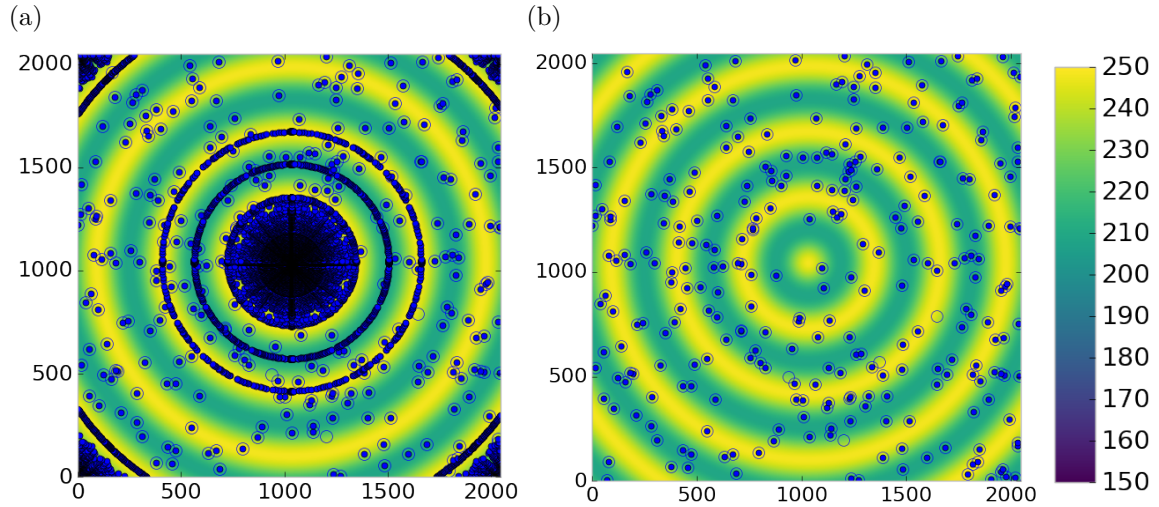


Figure 5.5: Generated dead/hot pixel masks for a detector with 300 bad pixels. a) the standard even bin mask and b) the  $Q$  resolution binned mask. The bad pixels are noted with open circles, masked pixels are noted with solid circles.

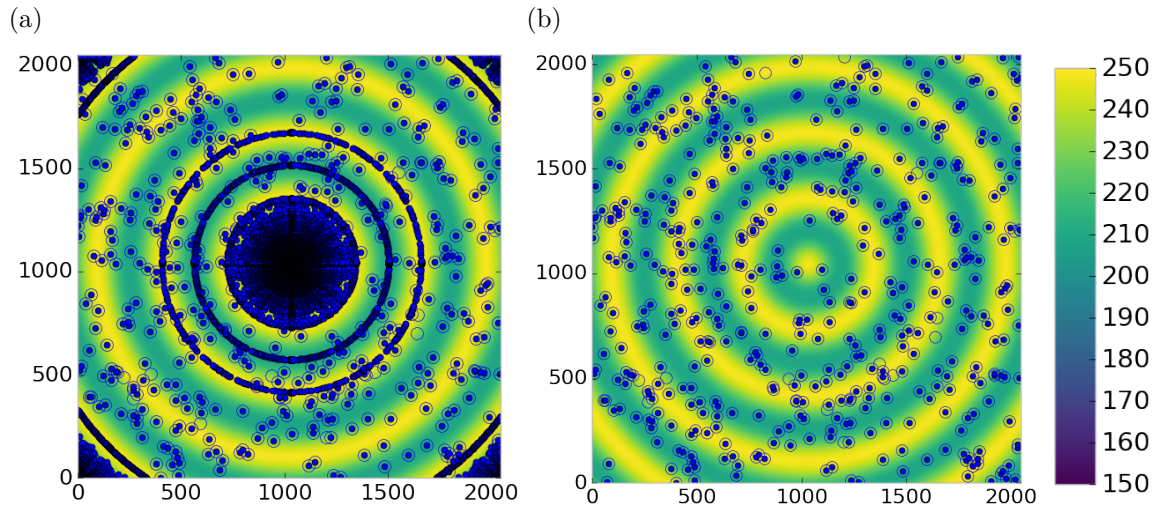


Figure 5.6: Generated dead/hot pixel masks for a detector with 500 bad pixels. a) the standard even bin mask and b) the  $Q$  resolution binned mask. The bad pixels are noted with open circles, masked pixels are noted with solid circles.

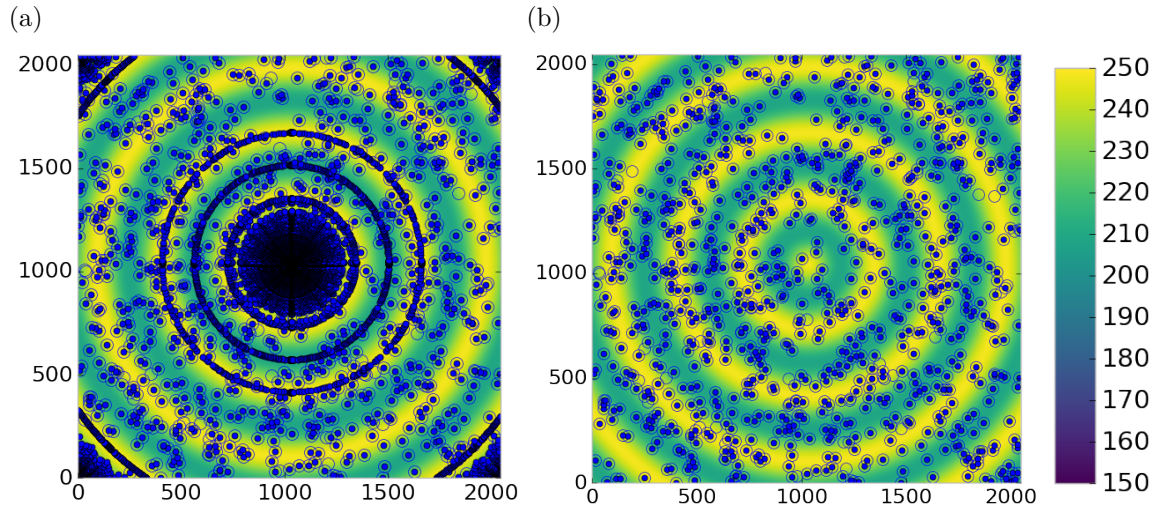


Figure 5.7: Generated dead/hot pixel masks for a detector with 1000 bad pixels. a) the standard even bin mask and b) the  $Q$  resolution binned mask. The bad pixels are noted with open circles, masked pixels are noted with solid circles.

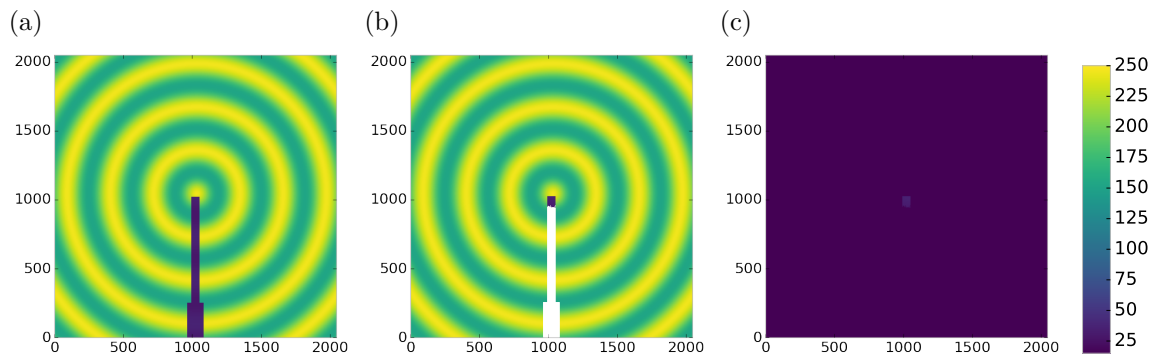


Figure 5.8: Generated beamstop holder masks for a beamstop holder with 10% transmittance. a) the raw image, b) the masked image, c) and the missed pixels. Note that the masked pixels in b) are white.

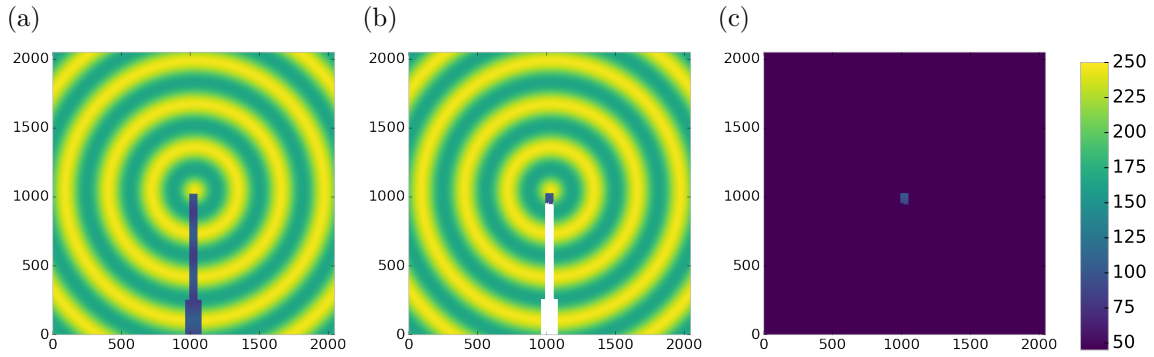


Figure 5.9: Generated beamstop holder masks for a beamstop holder with 30% transmittance. a) the raw image, b) the masked image, c) and the missed pixels. Note that the masked pixels in b) are white.

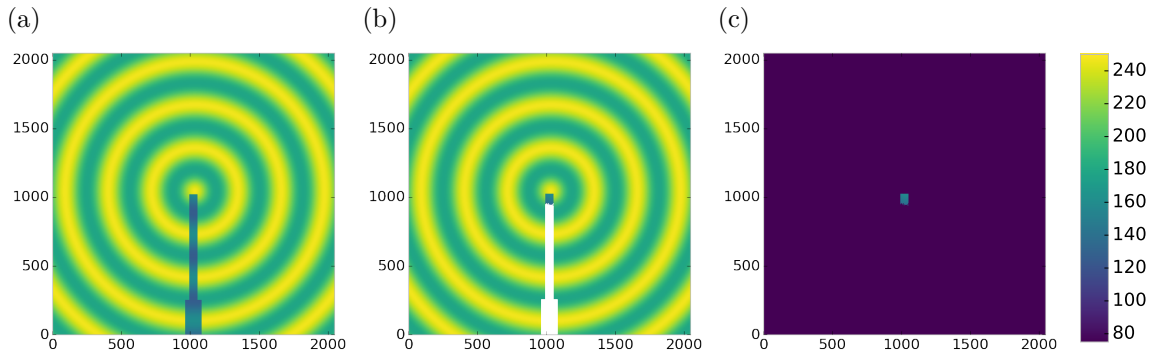


Figure 5.10: Generated beamstop holder masks for a beamstop holder with 50% transmittance. a) the raw image, b) the masked image, c) and the missed pixels. Note that the masked pixels in b) are white.

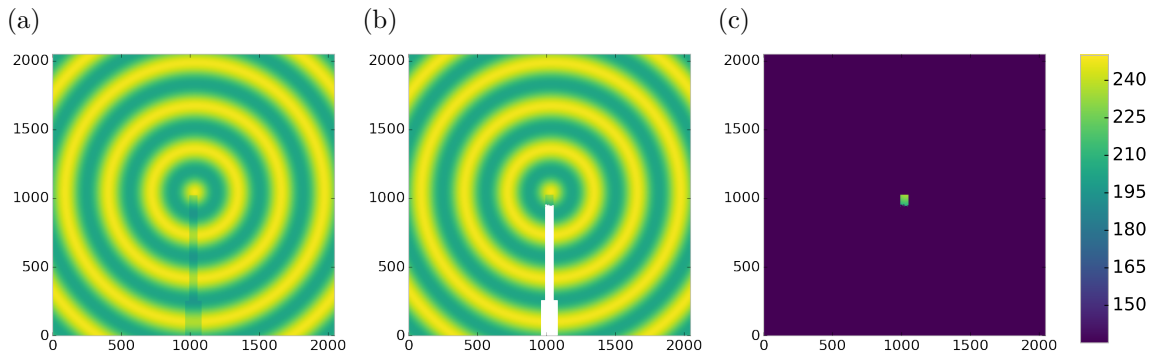


Figure 5.11: Generated beamstop holder masks for a beamstop holder with 90% transmittance. a) the raw image, b) the masked image, c) and the missed pixels. Note that the masked pixels in b) are white.

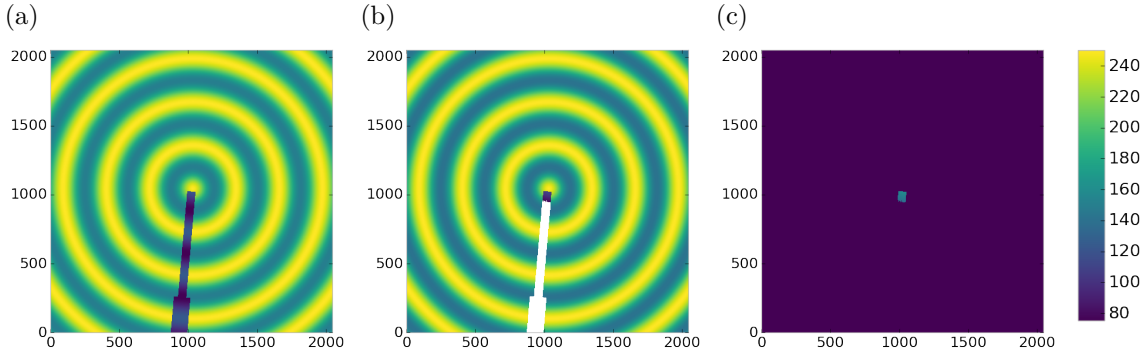


Figure 5.12: Generated beamstop holder masks which is rotated away from vertical. Note that the masked pixels in b) are white.

## 826 Results and Discussion

827 Three main studies were run each examining a different aspect of the simulated  
 828 or experimental studies. These included, masking bad pixels, masking a beamstop  
 829 holder, and masking experimental data. Figures 5.4-5.11 show the results of the  
 830 masking algorithm on simulated images. The dead/hot pixel masking shows the  
 831 importance of using the  $Q$  resolution based bin sizes as the even bin based mask have  
 832 a tendency to over mask the image, removing pixels which contain valuable signal.  
 833 This over-masking is caused by pixels being improperly associated with one another  
 834 by the even bins. Figure 5.4 indicates that the masking algorithm, with the proper  
 835 binning, masks the image perfectly, with no missed bad pixels or good pixels masked.  
 836 This is not the case in figures 5.5 - 5.7 as we can see pixels which should have been  
 837 masked but were not. Despite these missed pixels no pixels were improperly masked  
 838 in any of the well binned images. These test cases are actually more difficult than  
 839 experimental data, as the dynamic range of most detector causes the dead/hot pixels  
 840 and single crystal/texture peaks to be orders of magnitude away from the desired  
 841 signal.

842 The beamstop holder masks shown in figures 5.8 - 5.11, which were all run with  
 843 the  $Q$  resolution binning show similar results across the transmittance range, missing  
 844 only a small part of the beamstop holder near the point of incidence. Near this point

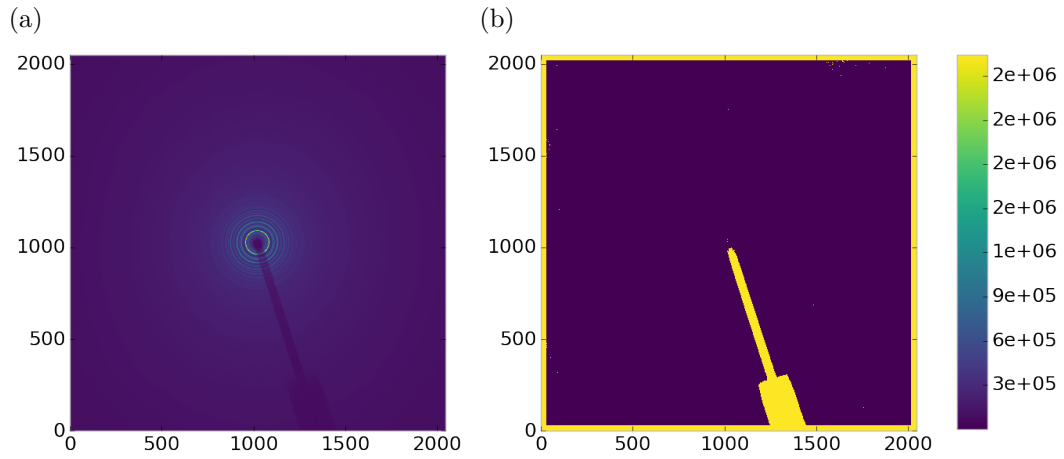


Figure 5.13: Masked experimental data. a) the raw image, b) the mask.

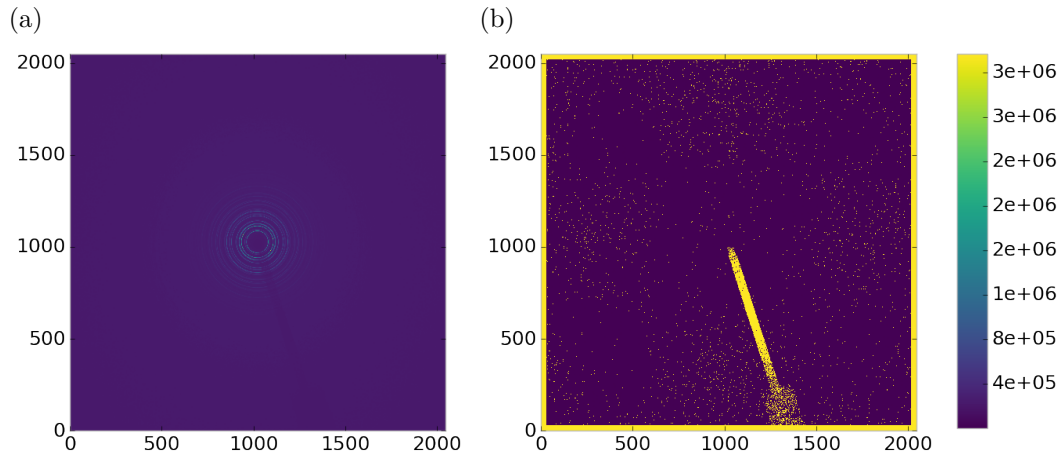


Figure 5.14: Masked experimental data with Pt single crystal signal. a) the raw image, b) the mask.

845 the beamstop holder becomes a statistically significant part of the total number of  
 846 pixels in a given ring, thus it can not be masked out using a statistical search of the  
 847 rings. For most PDF and XRD studies this small area can be masked automatically  
 848 by masking all the pixels who's distance from the point of incidence is smaller than a  
 849 given radius  $r$ , or can be neglected outright as the area is not used in the analysis or  
 850 refinement. Similar results were produced for beamstop holders which were rotated  
 851 away from the vertical position, as shown in figure 5.12

852 Working with actual experimental data, obtained at the Advanced Photon Source

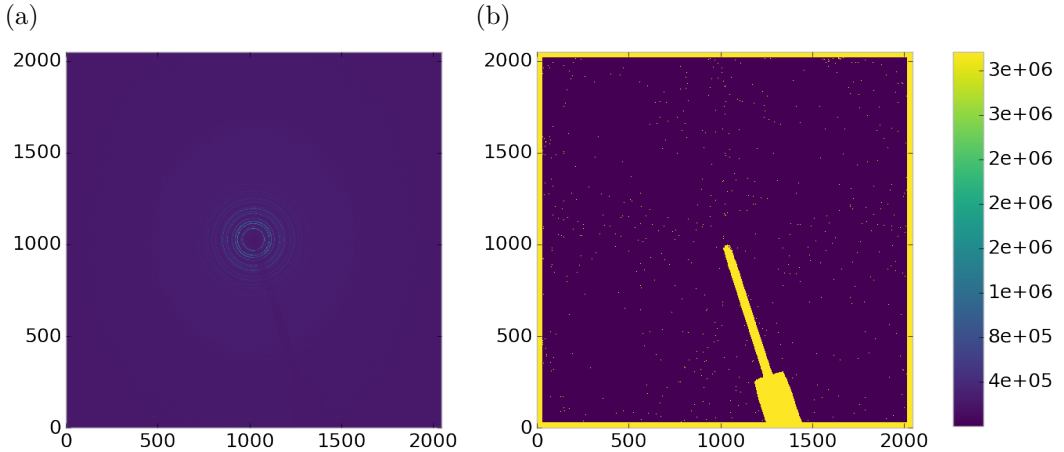


Figure 5.15: Masked experimental data with Pt single crystal signal using figure's 5.13 mask as a starting mask. a) the raw image, b) the mask.

beamline 11-ID-B, shows the difficulty of masking images which have low photon counts. While the masking of experimental data taken with longer exposures, consisting of 250 .2 second shots, shown in figure 5.13 provides very sharp edges to the beamstop holder, and very little extra masking beyond the occasional dead pixel, this is not the case for the single crystal data. The single crystal data is more problematic because of its short exposure time and low flux, with 500 frame at a .1 second exposure and having shrunk the beam size. The low flux is to prevent the very strong single crystal peaks from damaging the detector. However, this causes the image to be less statistically viable than ideal, causing problems with the mask as seen in figure 5.14. This can be alleviated to some degree by using the previously generated mask as a starting mask for the single crystal image, as shown in 5.15. While the masking algorithm still produces many diffuse masked pixels, they are far fewer, this may be due to the removal of the beamstop which could have contributed to the large standard deviation in figure 5.14.

867 **Conclusions**

868 In this section the masking algorithm, which relies on both  $Q$  resolution based bin-  
869 ning and a statistical approach to azimuthal symmetry, was developed. The focus of  
870 this algorithm was to remove many unwanted detector features associated with pixel  
871 defect, beamstop holder associated scattering attenuation, and single crystal/texture  
872 peaks. Simulated data was used to evaluate the beamstop holder and dead/hot pixel  
873 masking capacity, while experimental data was used to check for single crystal and  
874 texture based masking.  $Q$  resolution based binning was shown to be very important  
875 to avoid over-masking. The ability of the mask writer to mask images is somewhat  
876 limited by the overall statistical image quality, although some deficiencies can be  
877 obtained by using previously generated masks as starting points. This masking algo-  
878 rithm is now in use in the data processing workflow and will be available in scikit-beam  
879 soon.

880 **5.4 AUTOMATED IMAGE AZIMUTHAL INTEGRATION**

881 Using the  $Q$  resolution binning and masking developed in sections 5.2 and 5.3 the  
882 images can be properly integrated. Generally, images are integrated by taking the  
883 mean value of the pixels in a ring. However, other statistical measures of the average  
884 value can be used, like the median. Note that all the integrations done here use the  
885 pixels as they are, without pixel splitting, minimizing the covariance of the resulting  
886  $I(Q)$ .[54]

887 Figures 5.16-5.18 show the importance of masking and the choice of average func-  
888 tion. All the figures were produced using the same dataset, 50 °C  $\text{Pr}_2\text{NiO}_4$  taken at  
889 the APS's 11-ID-B on a Perkin Elmer area detector. The automatic masking alpha  
890 was 3 standard deviations from the mean. While it is difficult to observe the changes  
891 the mask causes in the full  $I(Q)$  plot (subfigures a) and b)), the standard deviation  
892 plots show the effect of bad pixels on the data (subfigure c)). Subfigure c) for figures

5.16-5.18 shows that removal of the beamstop holder lowers the low  $Q$  standard deviation from around .1 to almost .01 out to  $15 \text{ \AA}^{-1}$ . The high  $Q$  subfigures d) and f) in figures 5.16-5.18 show the “kink” effect of the detector edge and beamstop holder, where there is a dip in the  $I(Q)$  scattering when the rings include the edge of the detector. This effect seems to be due to both errors in the edge pixel intensity and the beamstop holder as masking of the edges only seems to provide only partial removal of the issue. It is important to note that while integration using the mean of the ring has issues with only the edge mask, as evidenced by the change in slope in 5.17 d) around  $29.5 \text{ \AA}^{-1}$ , the median integration does not include this error. Ideally the detector would have a normal distribution of pixel intensity for a given ring, which would imply an equivalency between the mean and median  $I(Q)$  values. Despite the closeness of the mean and median once the final mask has been created, it seems that the median is more reliable, as it was less effected by the beamstop holder in figure 5.17. Thus, for subsequent integrations discussed in this work the median is used to avoid any defective features that the masking algorithm may have missed.

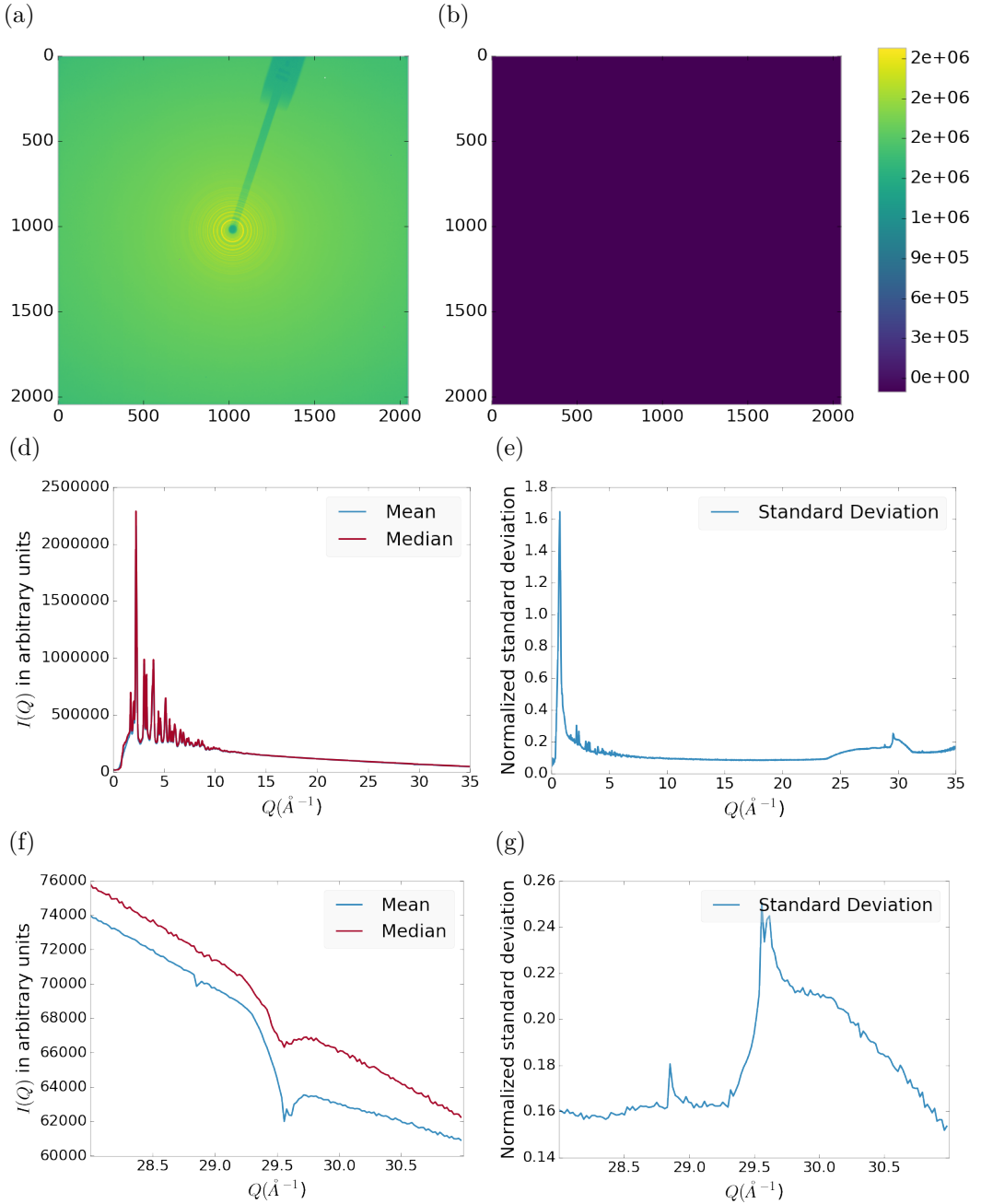


Figure 5.16: Masking, average, and standard deviation of an example x-ray total scattering measurement. This image was produced with no mask. a) the image, b) the mask, c) the mean and median values, d) the standard deviation (normalized to the median), e) a closeup of the  $28 \text{ \AA}^{-1}$  to  $31 \text{ \AA}^{-1}$   $Q$  range for the mean and median, f)  $28 \text{ \AA}^{-1}$  to  $31 \text{ \AA}^{-1}$   $Q$  range for the standard deviation

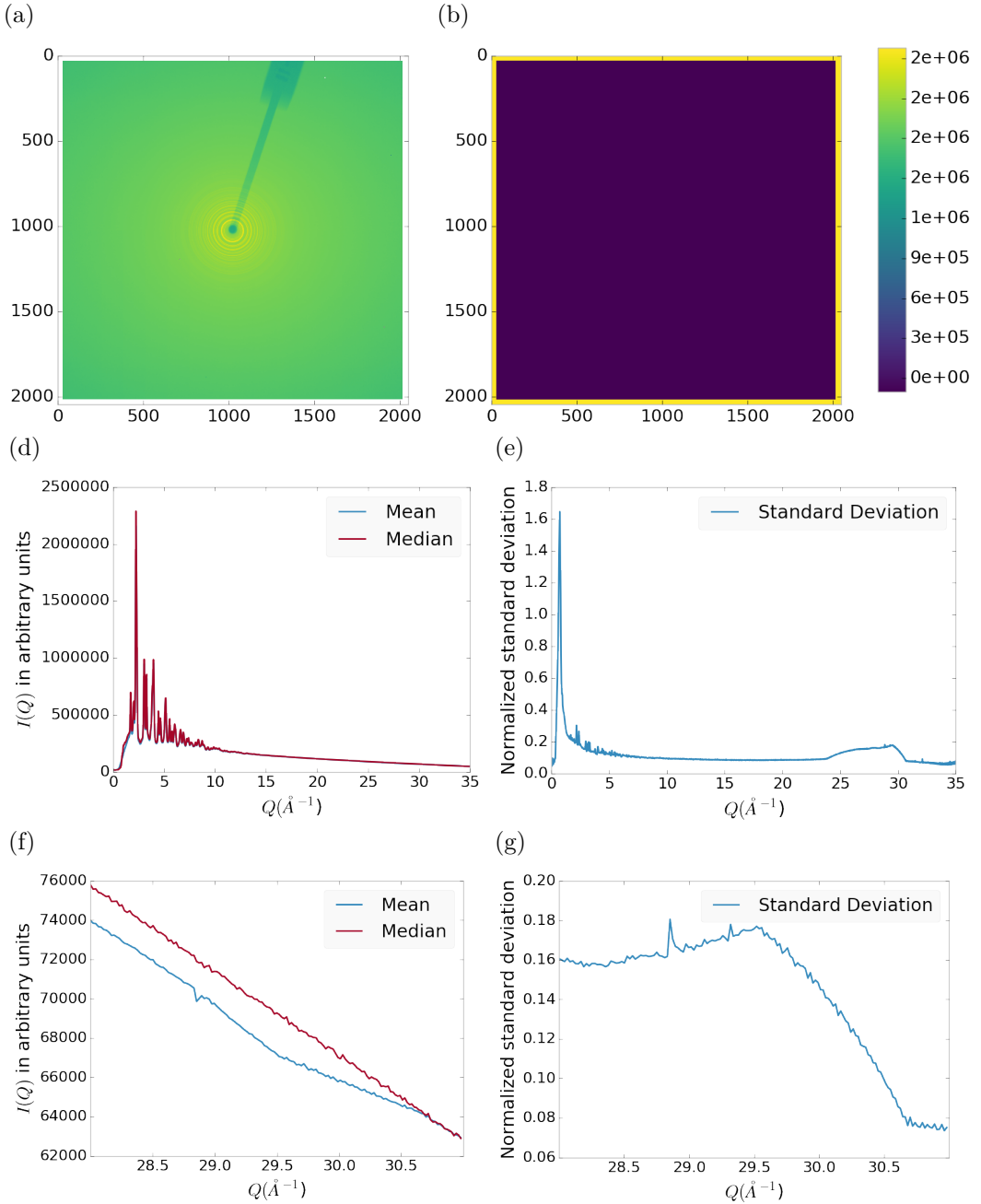


Figure 5.17: Masking, average, and standard deviation of an example x-ray total scattering measurement. This image was produced with only an edge mask. a) the image, b) the mask, c) the mean and median values, d) the standard deviation (normalized to the median), e) a closeup of the  $28 \text{\AA}^{-1}$  to  $31 \text{\AA}^{-1}$   $Q$  range for the mean and median, f)  $28 \text{\AA}^{-1}$  to  $31 \text{\AA}^{-1}$   $Q$  range for the standard deviation

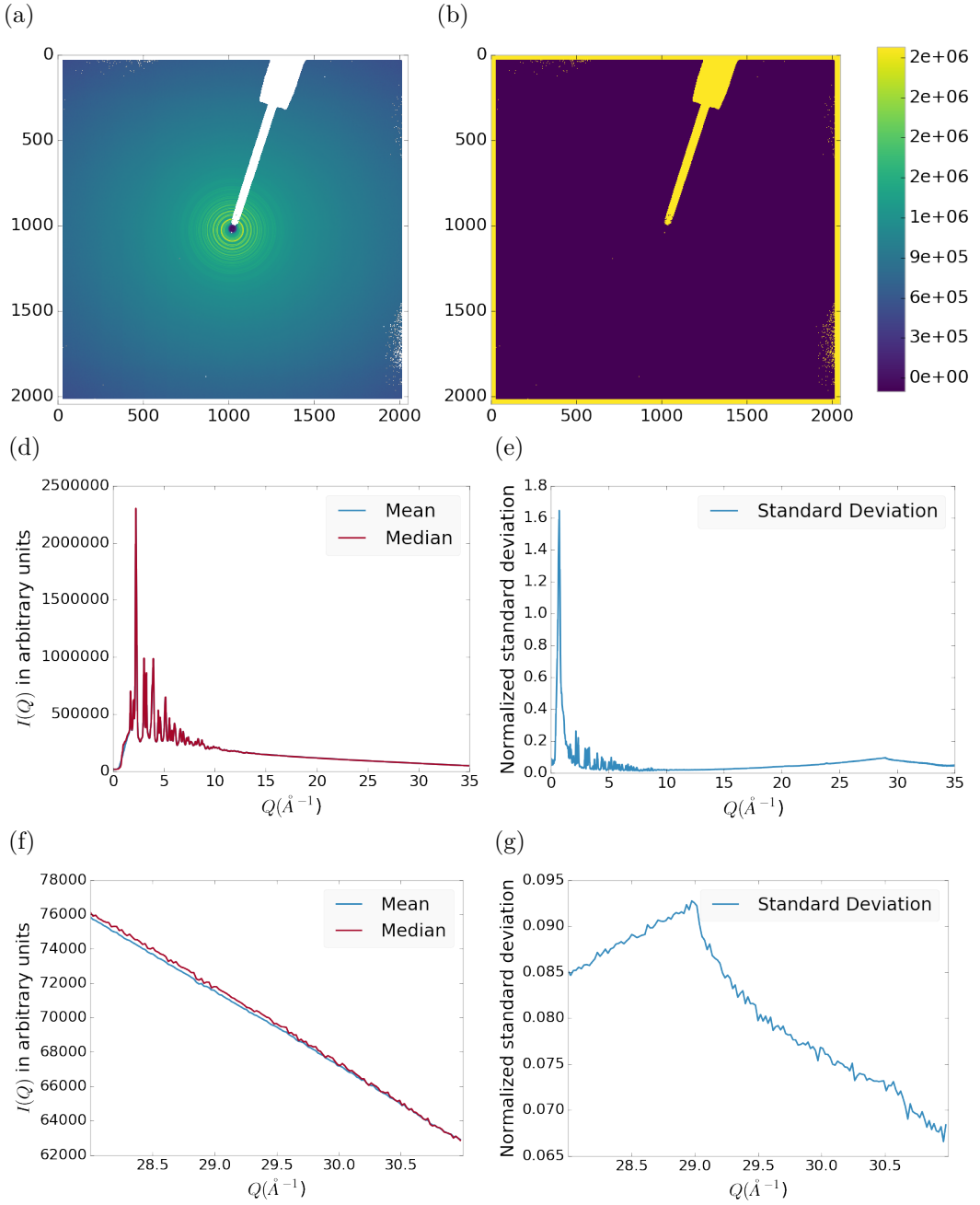


Figure 5.18: Masking, average, and standard deviation of an example x-ray total scattering measurement. This image was produced combining an edge mask and the automatically generated mask. a) the image, b) the mask, c) the mean and median values, d) the standard deviation (normalized to the median), e) a closeup of the  $28 \text{ \AA}^{-1}$  to  $31 \text{ \AA}^{-1}$   $Q$  range for the mean and median, f)  $28 \text{ \AA}^{-1}$  to  $31 \text{ \AA}^{-1}$   $Q$  range for the standard deviation

## 908 5.5 CONCLUSIONS

909 This chapter developed and analyzed the proper data processing and reduction method-  
910 ology for producing reliable  $F(Q)$  data from x-ray total scattering measurements.  
911 Binning at the  $Q$  resolution of the detector was found to be key to the data process-  
912 ing. The primary outcome of using the  $Q$  resolution binning was an enhancement  
913 in effectiveness for the masking algorithm, producing much fewer false positives for  
914 dead/hot pixels. This masking approach was then applied to the integration of ex-  
915 perimental data taken at the APD's 11-ID-B beamline. The automatically generated  
916 masks, when combined with edge masks, were found to greatly reduce the overall  
917 standard deviation of the pixel intensity and produce a smoother  $F(Q)$  at high  $Q$ ,  
918 enabling the use of much higher  $Q$  data in the PDF. Different statistical measures  
919 used in the azimuthal integration was also compared. This comparison showed that  
920 the median was a more reliable statistic for integration with data which had more  
921 detector defects. However, upon properly masking it was shown that these metrics  
922 were almost identical. The masking induced similarity between the mean and me-  
923 dian shows that the rings, when integrated, may form a Gaussian distribution. The  
924 distribution of the pixel intensities for strongly and weakly scattering samples may  
925 be investigated in future work.

926                   CHAPTER 6

927                   PHASE CHANGES AND ANNEALING DYNAMICS OF  
928                    $\text{Pr}_2\text{NiO}_4$  AND ITS DERIVATIVES

929                   6.1 INTRODUCTION

930                    $\text{Pr}_2\text{NiO}_4$  (PNO) electrodes provide higher power density than  $\text{La}_{0.8}\text{Sr}_{0.2}\text{MnO}_3$  (LSM),  
931                   and is more stable than  $(\text{La}_{0.60}\text{Sr}_{0.40})_{0.95}(\text{Co}_{0.20}\text{Fe}_{.80})\text{O}_{3-\text{x}}$  (LSCF), which is known to  
932                   rapidly degrade in performance. [57] PNO's high performance between 600-900 °C is  
933                   associated with its high activity towards the oxygen reduction reaction (ORR), which  
934                   stems from PNO's high oxygen diffusion and surface exchange coefficients, substantial  
935                   oxygen over-stoichiometry, and large oxygen ion conduction paths through the unit  
936                   cell. [55] Despite these advantages, PNO's tendency to partially decompose into  
937                    $\text{PrOx}$  and other phases is particularly challenging. [14] Full cell operation after 500  
938                   hours at 750 °C and 0.8 V shows major decomposition of the parent PNO phase,  
939                   while the performance degrades by only 4%. Such significant changes in phase and  
940                   relatively small changes in performance further assure the necessity for understanding  
941                   the phase evolution in nickelate cathodes during operation. To address these disparity  
942                   in performance and phase degradation PDF and XRD analysis may be able to examine  
943                   these issues from both long and short range ordering perspectives.

944 6.2 EXPERIMENTS

945 **Pr<sub>2</sub>NiO<sub>4</sub> Synthesis**

946 Pr<sub>2</sub>NiO<sub>4</sub> was synthesized using the standard approach, as detailed in the work by  
947 Dogdibegovic et. al. [14] The nickelate powder was initially prepared via the glycine-  
948 nitrate process. This was followed by thermal annealing at 1080 °C for 10 hours in  
949 air.

950 **X-ray Measurements**

951 X-ray total scattering and x-ray powder diffraction experiments were performed at  
952 the APS's 11-ID-B beamline. An x-ray energy of 86.7 keV, .145 Åwas provided  
953 by the beamline monochromator. The detector was moved between a 20cm and a  
954 95 cm sample to detector distance to measure the x-ray total scattering and x-ray  
955 diffraction patterns. Various PNO samples were annealed on the beamline during  
956 x-ray measurement.

957 6.3 DATA PROCESSING

958 The data was calibrated at each of the detector positions using a CeO<sub>2</sub> standard via  
959 pyFAI. [30] The images were corrected for a .95 x-ray polarization. Masks were pro-  
960 duced for both the foreground and background images. The foreground masks were  
961 produced using both a 30 pixel edge mask and a  $2.5\sigma$  automatic mask as discussed  
962 in chapter 5. The background masks were produced by using the foreground mask as  
963 a starting mask with a  $2.5\sigma$  automatic mask.

964 The foreground and background images were then integrated using the  $Q$  resolu-  
965 tion binning discussed in chapter 5. The resulting  $I(Q)$  data were corrected for their  
966 number of frames and  $I_{00}$ . Finally the corrected background  $I(Q)$  was subtracted  
967 from the foreground  $I(Q)$ .

968        Each PDF was generated with a  $Q_{min}$  of 1.5,  $Q_{max}$  of 29.,  $R_{poly}$  of .9,  $R_{max}$  of 40.  
969        descriptions of these parameters can be found in the work by Juhas et. al. [28]

970        **6.4 DATA ANALYSIS**

971        **Intra Sample Comparison**

972        **PDF**

973        As figures 6.1 and 6.2 show the as synthesized PNO undergoes very little change in  
974        structure according to the PDF. The PDF does show some broadening at around 3.5  
975        and 8.5 Å, but the peak shifts themselves are fairly limited. This implies that the as  
976        synthesized PNO structure is stable at least for the 1 hour that the sample was held  
977        at 750 °C.

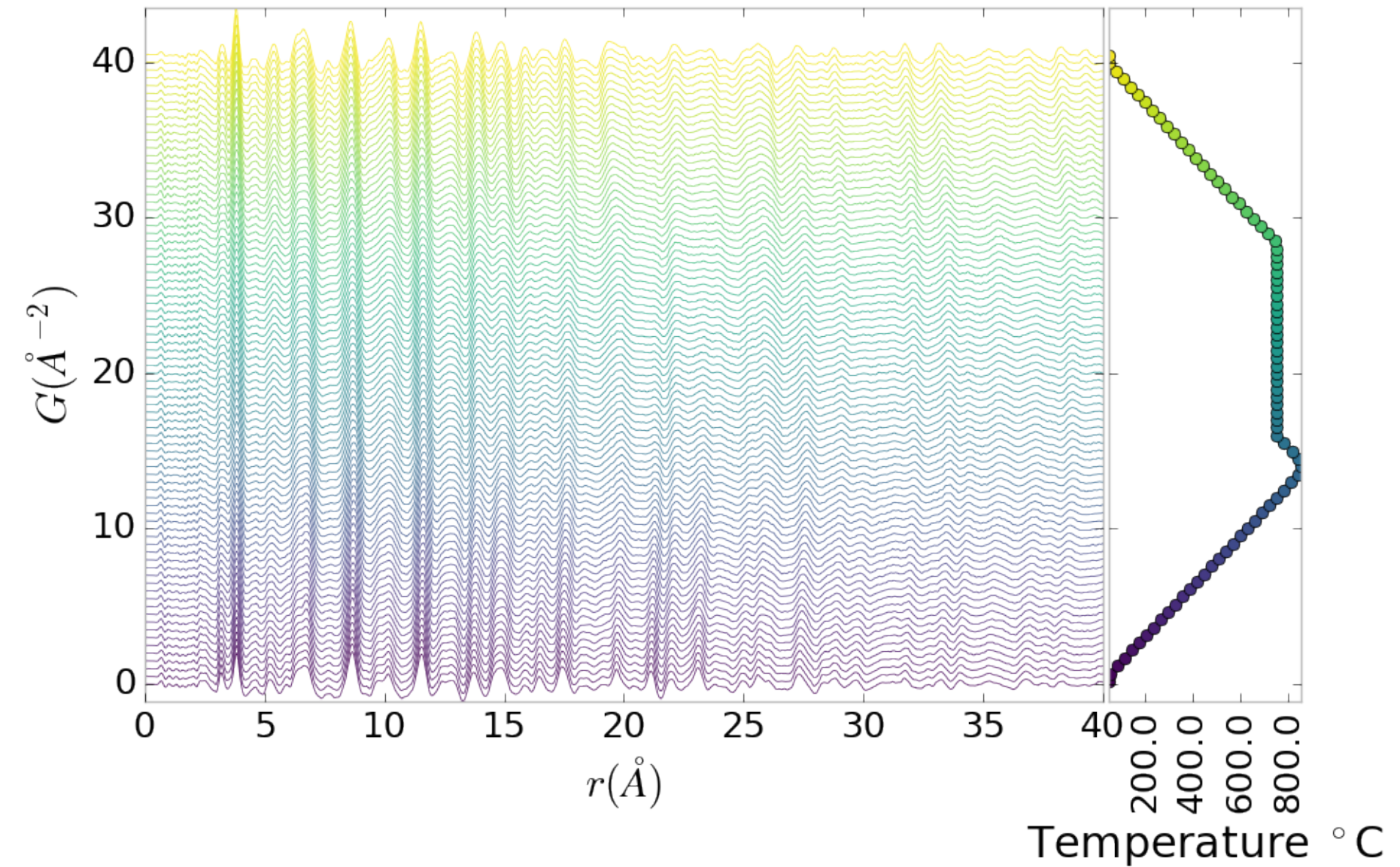
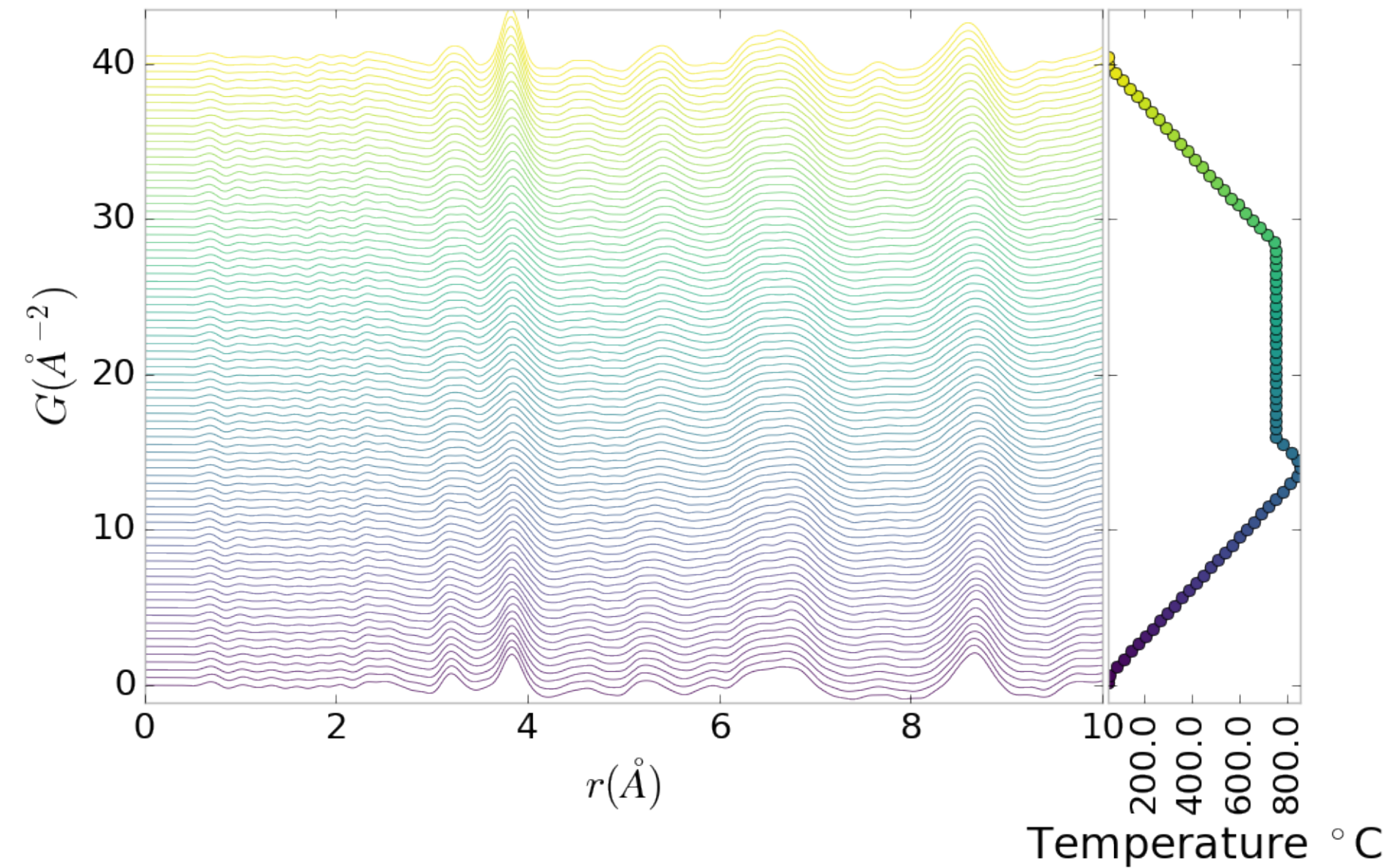


Figure 6.1: PDF as a function of temperature for as synthesized PNO showing the full PDF



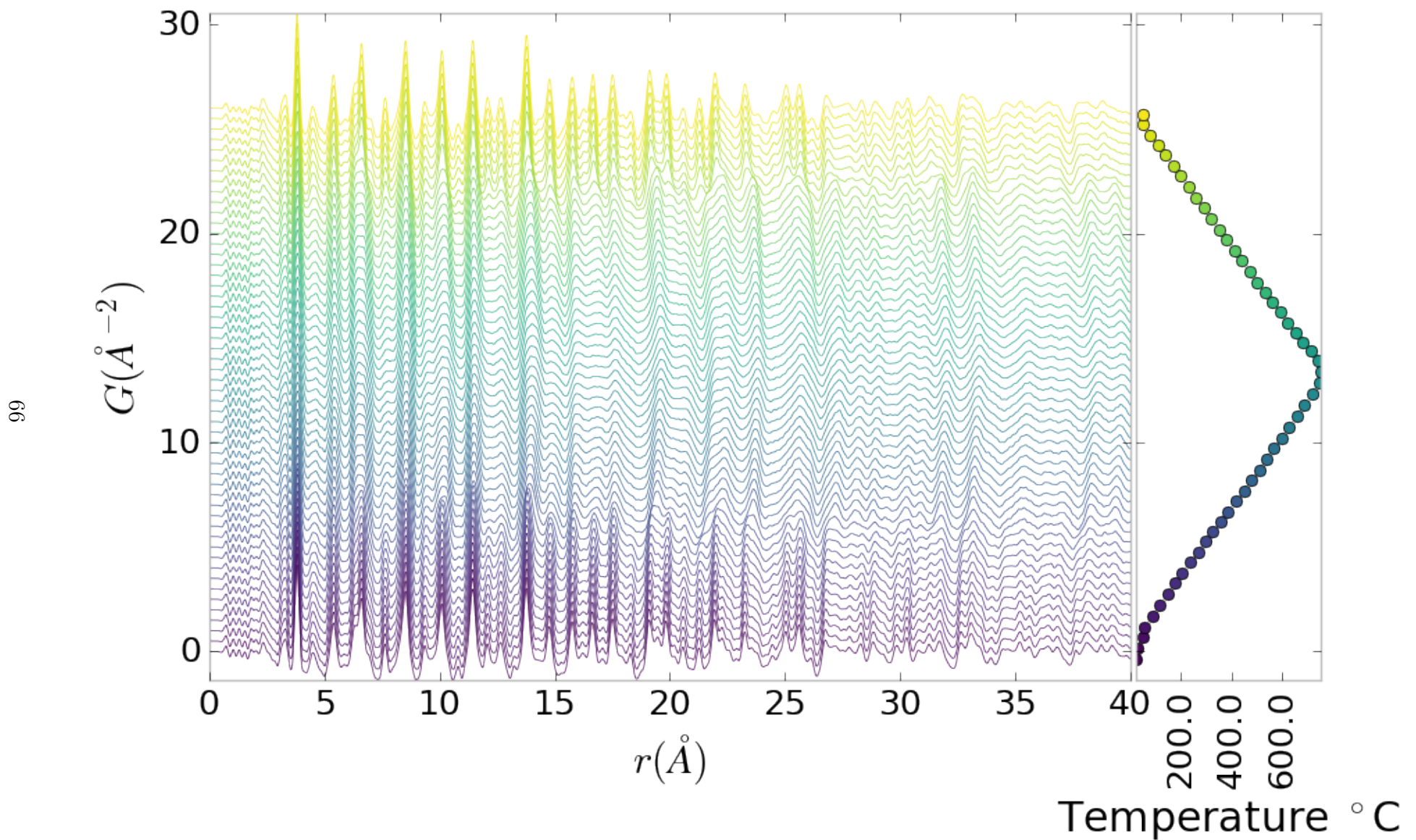


Figure 6.3: PDF as a function of temperature for PNO annealed at 750  $^{\circ}\text{C}$  for 25 hours showing the full PDF

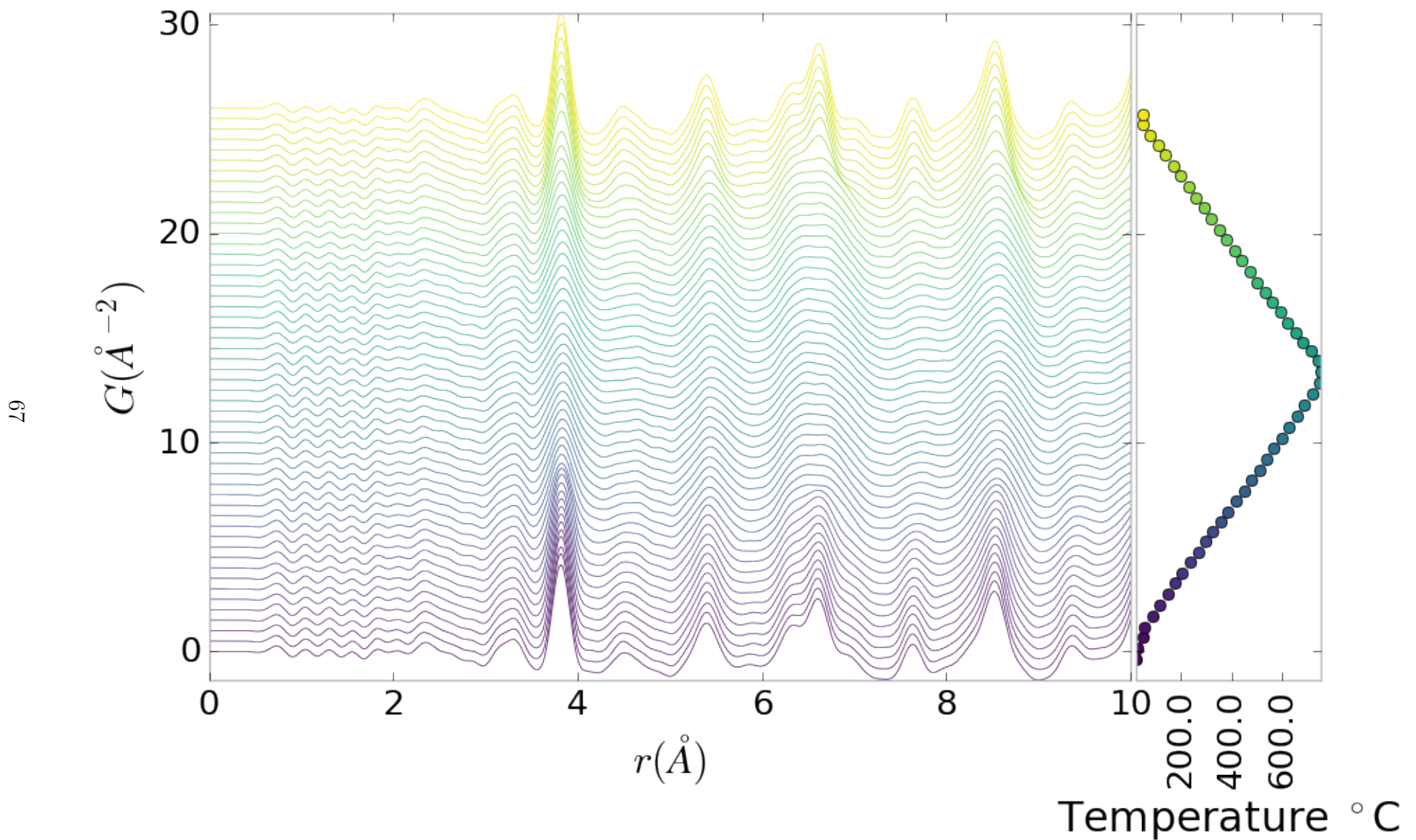


Figure 6.4: PDF as a function of temperature for PNO annealed at 750 °C for 25 hours showing a close up on the short range section

978  $I(Q)$

979 The annealed samples figures, 6.3 and 6.4, tell a rather different story. In this case the  
980 PDF shows significant peak shifts and broadening, especially at higher interatomic  
981 distances. Some peaks completely disappear, like the peak at 12 Å. Similar results  
982 were also observed for samples with longer annealing times, as shown in the appendix.

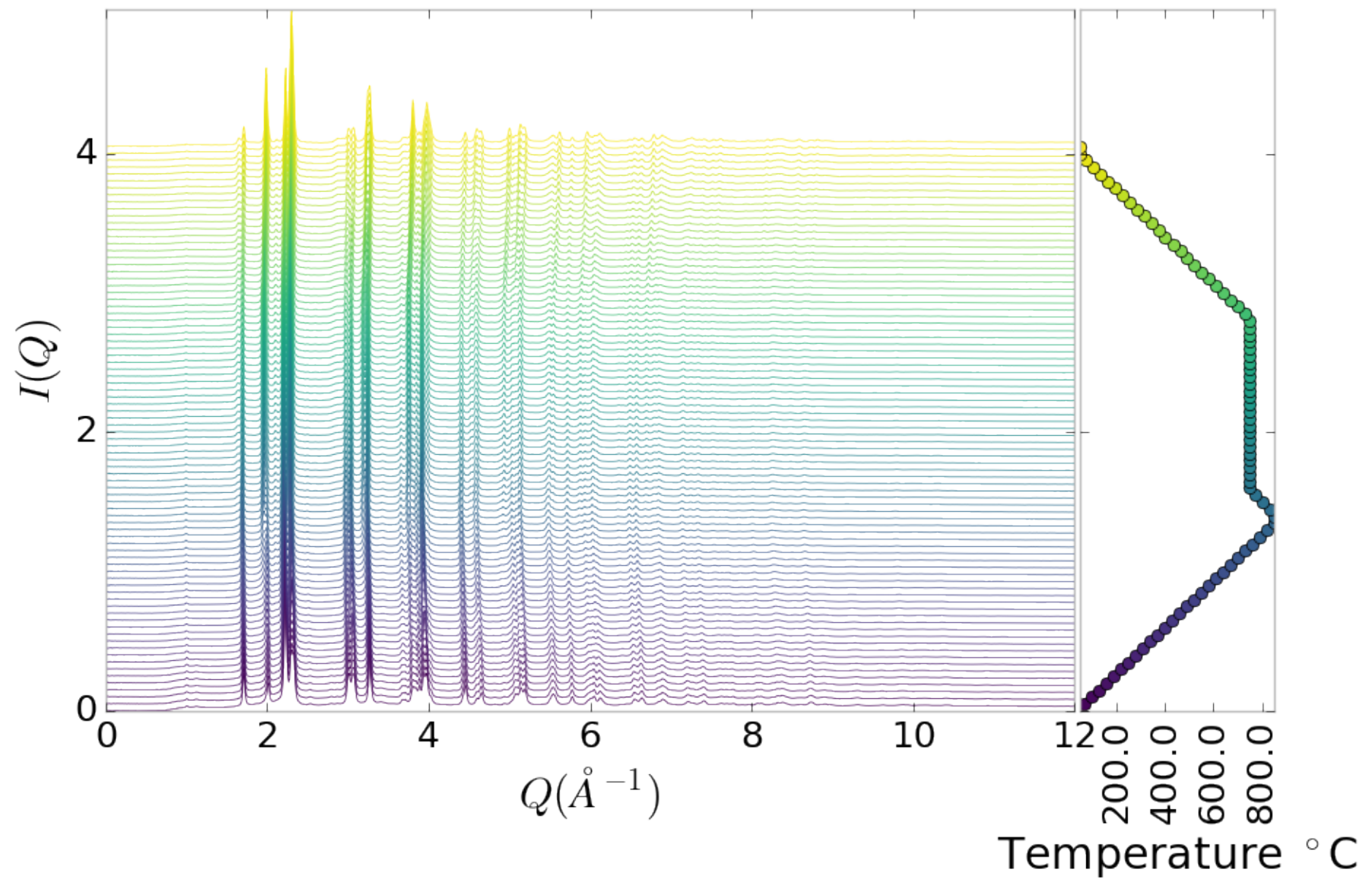


Figure 6.5:  $I(Q)$  as a function of temperature for as synthesized PNO showing the full XRD

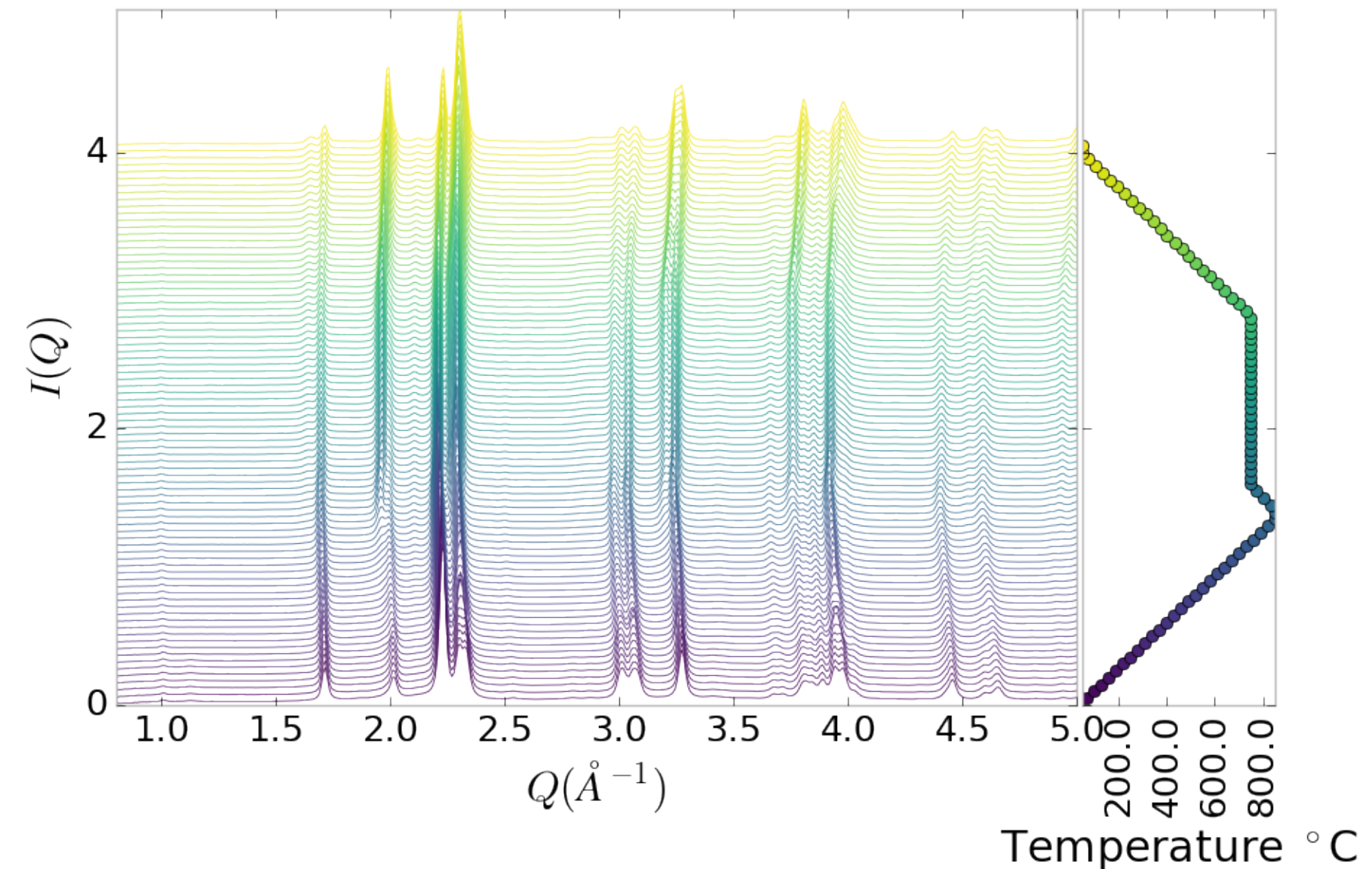


Figure 6.6:  $I(Q)$  as a function of temperature for as synthesized PNO showing a close up on the low  $Q$  section

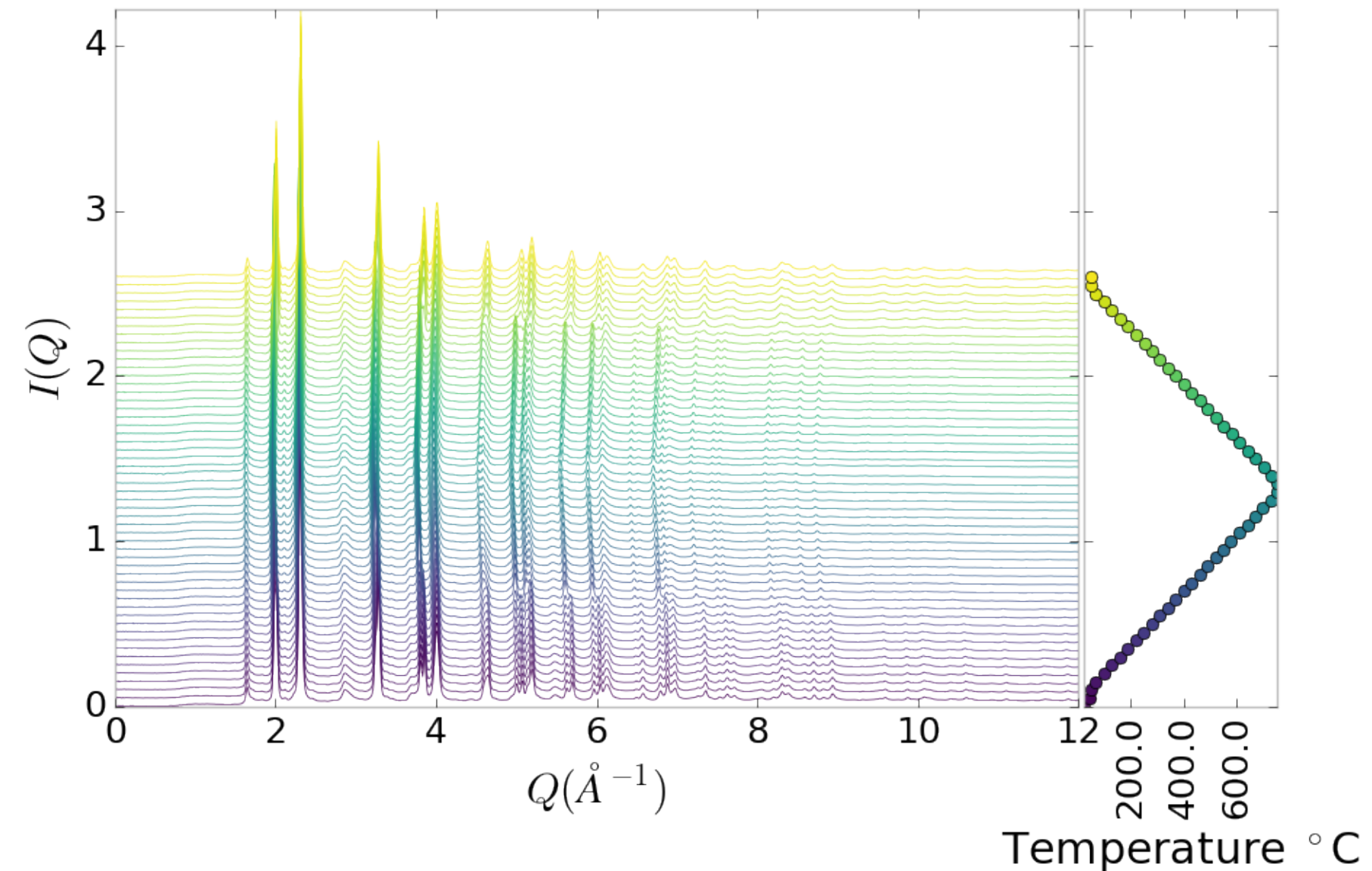


Figure 6.7:  $I(Q)$  as a function of temperature for PNO annealed at 750 °C for 25 hours showing the full XRD

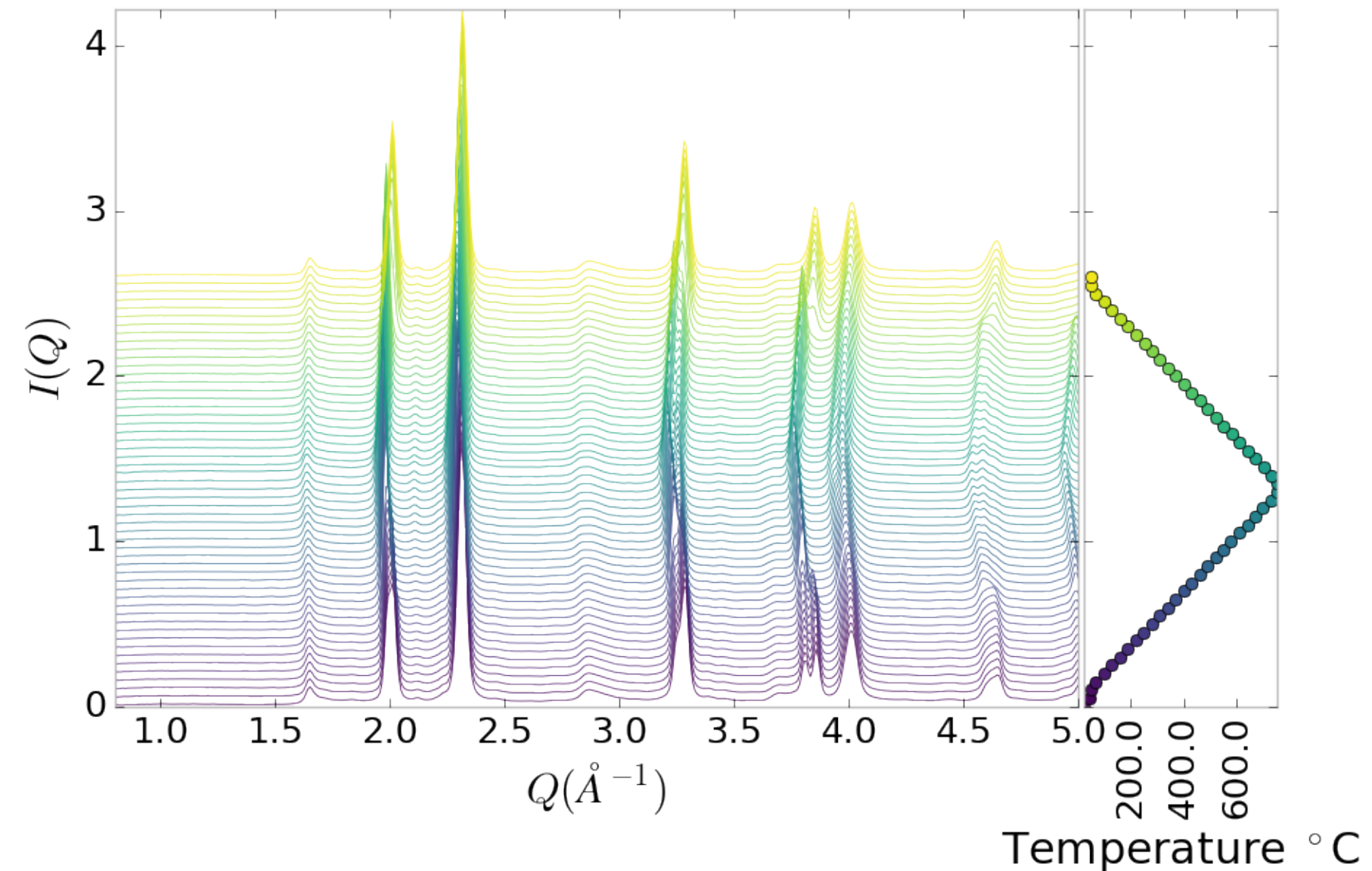


Figure 6.8:  $I(Q)$  as a function of temperature for PNO annealed at 750 °C for 25 hours showing a close up on the low  $Q$  section

983 **Inter Sample Comparison**

984 Figures A.26 and A.20 show a very interesting contrast. Figure A.26 show significant  
985 differences in the  $I(Q)$  between the as-synthesized and annealed PNO, which could  
986 be associated with the more degradation present in the annealed samples. However,  
987 figure A.20 shows very little difference in the PDF between the various annealing  
988 times. This discrepancy seems to point to some kind of disorder which changes the  
989 interatomic distances very little but changes the symmetry enough to change the  
990 Bragg reflections.

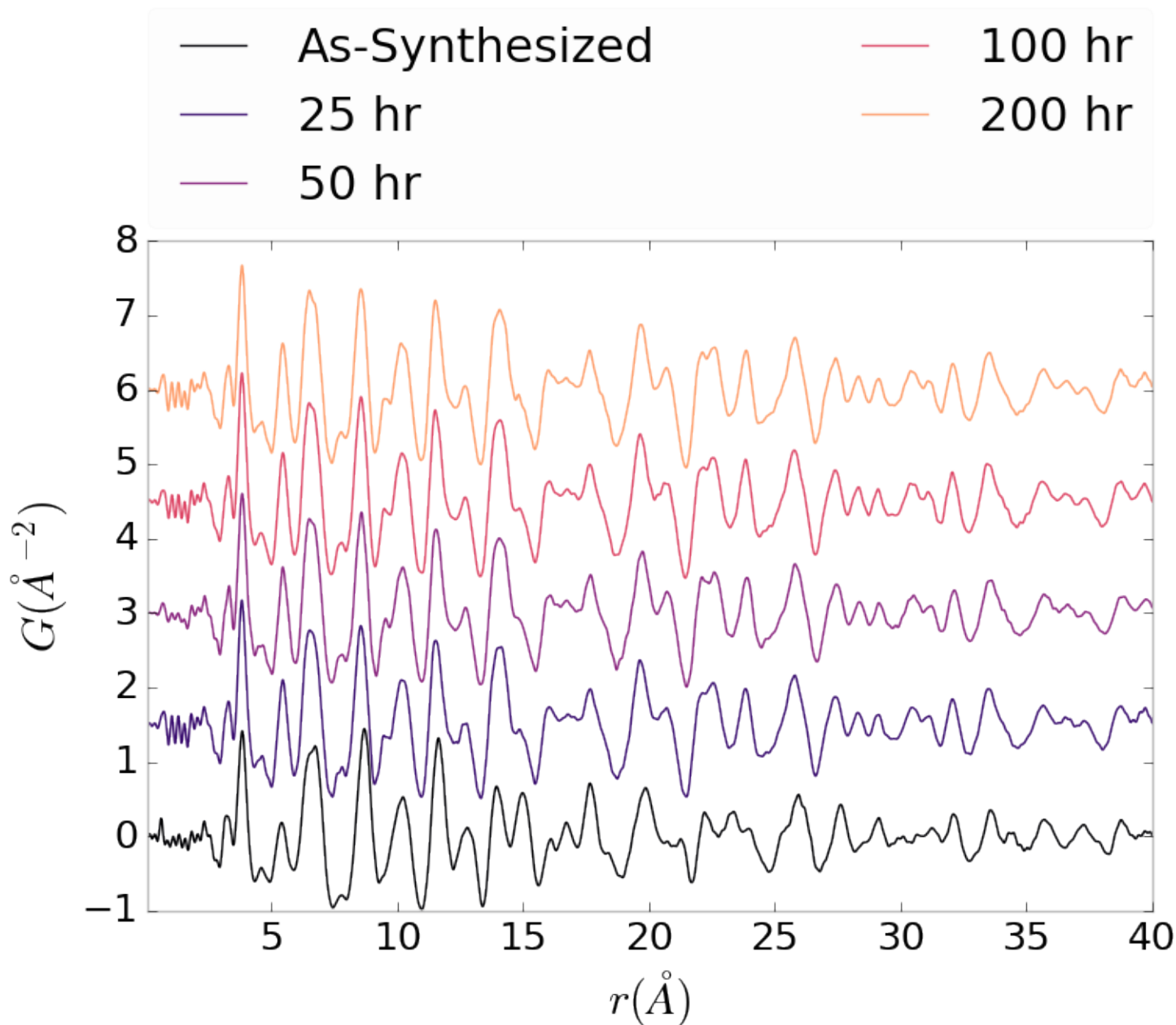


Figure 6.9: Comparison of PNO sample PDFs as a function of annealing time high-temp

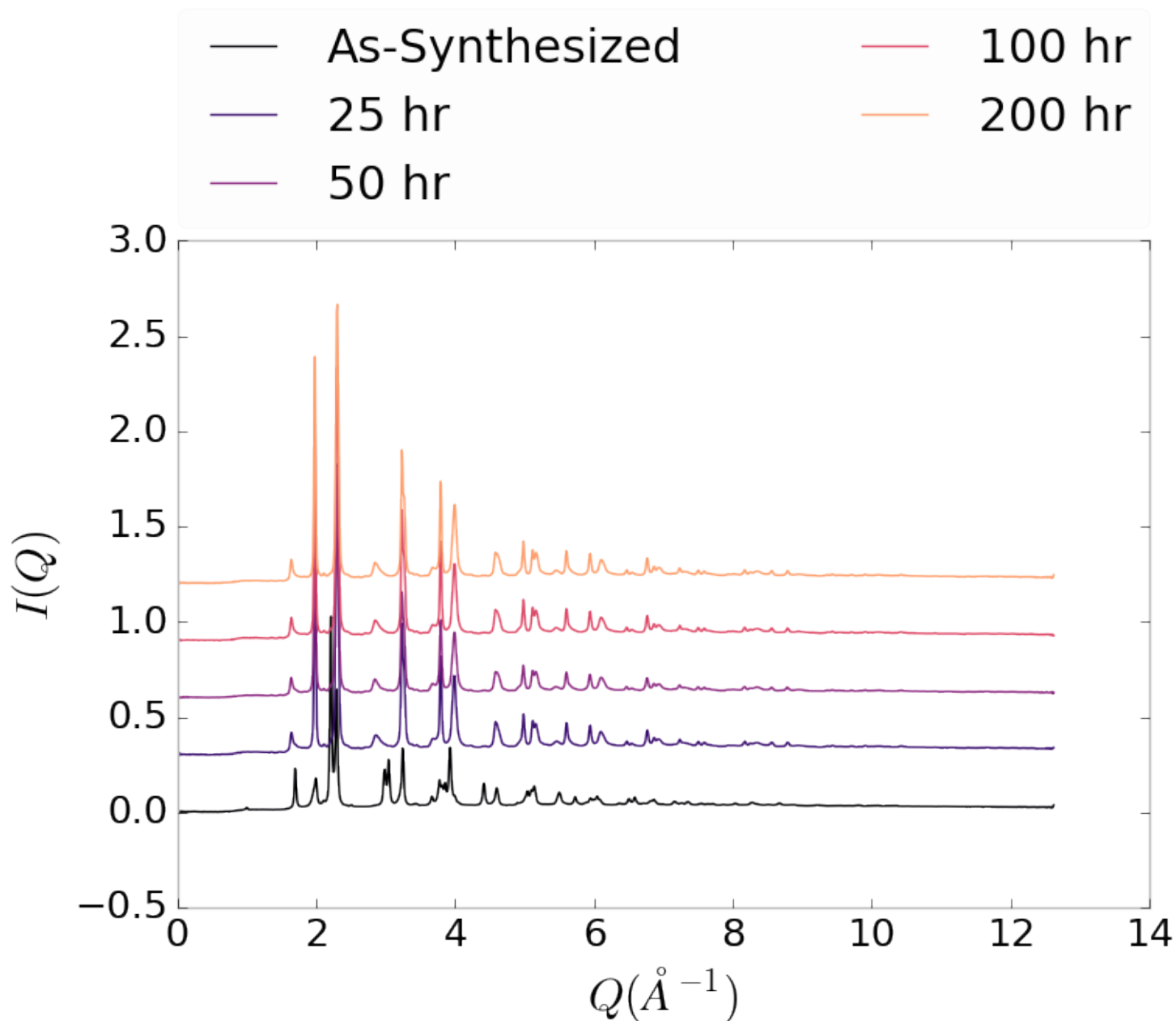


Figure 6.10: Comparison of PNO sample  $I(Q)$  as a function of annealing time high-temp

991 6.5 SIMULATION

992 Simulations have not been run yet on these PNO samples. Solving the structures of  
993 these samples is expected to be more difficult than the NP benchmarks previously  
994 solved. The difficulty of these simulations is due to:

- 995 1. The PDF's insensitivity to the oxygen positions, due to the poor x-ray scattering  
996 off the very electron poor oxygen.
- 997 2. The large difference in mass between the oxygen and other atoms, causing the  
998 dynamics of the simulation to be governed by oxygen motion, necessitating long  
999 simulation times to obtain movement of the other atoms.
- 1000 3. The large parameter space caused by potential defects and degradation prod-  
1001 ucts. Without knowing that the starting phase is pure, it is difficult to even  
1002 produce starting structures, since the simulation will need to explore all the  
1003 potential defect/degenerated structures.

1004 6.6 CONCLUSIONS

1005 X-ray total scattering and x-ray powder diffraction data was obtained on  $\text{Pr}_2\text{NiO}_4$   
1006 powder samples annealed for various lengths of time. In-situ studies on the beamline  
1007 were performed to understand how the structure of each of these powders changes  
1008 at operating temperatures. The data was processed with the previously discussed  $Q$   
1009 binning, masking, and integration methodology. The PDF results show very little  
1010 change in the structure for the as synthesized sample. However, the PDFs show  
1011 a large change in the previously annealed samples. These changes seem to produce  
1012 PDFs similar to the as-synthesized PNO at operating temperatures. This would seem  
1013 to imply that the source of the anomalous PNO phase/power density relationship may  
1014 be due to the adoption of an active structure upon heating which is universal despite

1015 the amount of thermal degradation observed at room temperature. In contrast to the  
1016 PDF results, the XRD results seem to show significant changes in the PNO structure,  
1017 both with ex-situ and in-situ annealing. The XRDs show the degradation of the PNO  
1018 into various phases, potentially including  $\text{Pr}_2\text{O}_{11}$ , and higher ordered Pr based phases.  
1019 The discrepancy between these two results is quite interesting as it seems that the  
1020 XRD and PDF results are contradictory. Turbostratic displacements between the  
1021 layers may be a cause of the PDF/XRD disagreement, as these changes would cause  
1022 very little change in the local structure observed in the PDF, while causing large  
1023 changes in the XRD.

1024

## CHAPTER 7

1025

### CONCLUSION

1026 The work here presents one of the most complete end to end approaches to pro-  
1027 cessing, analyzing, and simulating atomic pair distribution function data. The goals  
1028 of this work were to build a modular, quick, and robust method for handling both  
1029 experimental PDF data and solving atomic structures from said data.

1030 The statistical mechanical PES solvers were designed to robustly find atomic  
1031 solutions which are global minima of the PES. This was accomplished by using some  
1032 of the most advanced Monte Carlo algorithms and samplers. The analytical equations  
1033 for the PES and its gradients were derived to provide the quickest searches.

1034 The PDF gradients were derived and implemented as GPU kernels to further  
1035 speed up the PES search. The inclusion of the GPUs, combined with the atom pair  
1036 mapping, were found to provide a 10x to 100x speedup over a multiprocessor based  
1037 CPU methodology.

1038 The extensive benchmarking of the NUTS-HMC system presented in chapters 2  
1039 and 3 showcased the system's robustness, speed, and effectiveness. Interestingly it  
1040 seems the the simulations also helped to elucidate the relationship between  $Rw$  and  
1041 the resulting fit of the secondary metrics, including radial bond distribution. This is  
1042 particularly important as it begins to establish  $Rw$  goals and a relationship between  
1043  $Rw$  and the confidence that features from the underlying structure that the PDF  
1044 represents are reproduced by the structural model which is produced my Monte Carlo  
1045 modeling. It seems that the threshold for acceptable  $Rw$  in Monte Carlo modeling  
1046 needs to be quite lower than the current literature standards to properly reproduce

1047 the structure.

1048 A novel data processing workflow was also developed which focused on using  $Q$   
1049 resolution binning to create masks automatically and azimuthally integrate. The  
1050  $Q$  resolution binning provided a significant improvement in the automated masking  
1051 robustness, leading to much fewer false positives, as shown by a series of masks  
1052 generated on simulated and experimental data. The effect of these masks on the  
1053 median and mean azimuthal integration was also discussed, establishing masks as  
1054 very important to the removal of the high  $Q$  “kink” seen in 2D area detector data.  
1055 Furthermore, a comparison was drawn between the median and mean integration,  
1056 showing the median to be more reliable than the mean when working with data that  
1057 could have residual detector defects. Overall the masking scheme was shown to reduce  
1058 the standard deviation of the data significantly.

1059 Finally, preliminary results of x-ray total scattering measurements on  $\text{Pr}_2\text{NiO}_4$   
1060 were presented. Interestingly, these results show a strong discrepancy between the  
1061 PDF and  $I(Q)$  data. Where the PDF shows a very static as synthesized structure,  
1062 despite annealing, the associated  $I(Q)$  data shows peak movement and formation. For  
1063 the pre-annealed samples both the  $I(Q)$  and PDF data show peak changes. Inter-  
1064 estingly, the PDFs of the as synthesized and pre-annealed samples show very similar  
1065 local structure at operating temperatures.

1066 Despite all the work presented here, there is of course much more to be done.  
1067 Implementing new ensembles, like Parallel Tempering, and faster Grand Canonical  
1068 Monte Carlo, may help to find solutions faster and with less user based parameter  
1069 tuning. Building the mathematics and software to quickly compute the data from  
1070 other atomistic experiments, including EXAFS, STEM, and neutron scattering, could  
1071 help to produce structures which more fully describe all the available experimental  
1072 data. Implementing the existing codebase in a more general High Performance Com-  
1073 putting context would allow for the solution of much larger particles, and extended

1074 solids. Further benchmarking will help to probe the robustness of the algorithm  
1075 with other systems, including systems with periodic boundary conditions. Faster  
1076 scattering data processing will enable a quicker total turn around time from taking  
1077 experimental images to producing atomic structures.

1078 It is expected that this work will become a standard method for solving atomic  
1079 structures from x-ray total scattering experiments, having presented one of the most  
1080 complete end to end x-ray processing and analysis systems.

1081

## BIBLIOGRAPHY

- 1082 [1] Milinda Abeykoon, Christos D. Malliakas, Pavol Juhás, Emil S. Božin, Mer-  
1083 couri G Kanatzidis, and Simon J L Billinge, *Quantitative nanostructure char-*  
1084 *acterization using atomic pair distribution functions obtained from laboratory*  
1085 *electron microscopes*, Zeitschrift fur Kristallographie **227** (2012), no. 5, 248–256.
- 1086 [2] Alexandre A. Arnold, Victor Terskikh, Qian Ying Li, Rafik Naccache, Isabelle  
1087 Marcotte, and John A. Capobianco, *Structure of NaYF<sub>4</sub> upconverting nanopar-*  
1088 *ticles: A multinuclear solid-state NMR and DFT computational study*, Journal  
1089 of Physical Chemistry C **117** (2013), no. 48, 25733–25741.
- 1090 [3] Simon J L Billinge and Takeshi Egami, *Underneath the Bragg Peaks: Structural*  
1091 *Analysis of complex Materials*, vol. Volume 16, Pergamon, 2012.
- 1092 [4] Simon J L Billinge and Igor Levin, *The problem with determining atomic struc-*  
1093 *ture at the nanoscale.*, Science (New York, N.Y.) **316** (2007), no. 5824, 561–565.
- 1094 [5] P. E. Blöchl, *Projector augmented-wave method*, Physical Review B **50** (1994),  
1095 no. 24, 17953–17979.
- 1096 [6] Gary K. Chen and Yunfei Guo, *Discovering epistasis in large scale genetic as-*  
1097 *sociation studies by exploiting graphics cards*, Frontiers in Genetics **4** (2013),  
1098 no. DEC, 1–12.
- 1099 [7] Joshua J Choi, Xiaohao Yang, Zachariah M Norman, Simon J L Billinge, and  
1100 Jonathan S Owen, *Structure of methylammonium lead iodide within mesoporous*  
1101 *titanium dioxide: Active material in high-performance perovskite solar cells*,  
1102 Nano Letters **14** (2014), no. 1, 127–133.
- 1103 [8] Peter J. Chupas, Karena W. Chapman, Charles Kurtz, Jonathan C. Hanson,  
1104 Peter L. Lee, and Clare P. Grey, *A versatile sample-environment cell for non-*  
1105 *ambient X-ray scattering experiments*, Journal of Applied Crystallography **41**  
1106 (2008), no. 4, 822–824.
- 1107 [9] PJ Chupas, X Qiu, JC Hanson, PL Lee, CP Grey, and SJL Billinge, *Rapid-*

- 1108        *acquisition pair distribution function (RA-PDF) analysis*, Journal of Applied  
1109        Crystallography **36** (2003), 1342–1347.
- 1110 [10] Matthew J. Cliffe, Martin T. Dove, D. A. Drabold, and Andrew L. Goodwin,  
1111        *Structure determination of disordered materials from diffraction data*, Physical  
1112        Review Letters **104** (2010), no. 12, 1–4.
- 1113 [11] Matthew J Cliffe and Andrew L Goodwin, *Nanostructure determination from the*  
1114        *pair distribution function: a parametric study of the INVERT approach.*, Journal  
1115        of physics. Condensed matter : an Institute of Physics journal **25** (2013), no. 45,  
1116        454218.
- 1117 [12] Chunhua Cui, Lin Gan, Marc Heggen, Stefan Rudi, and Peter Strasser, *Composi-*  
1118        *tional segregation in shaped Pt alloy nanoparticles and their structural behaviour*  
1119        *during electrocatalysis.*, Nature materials **12** (2013), no. 12, 765–771.
- 1120 [13] Juarez L F Da Silva, Hyoung Gyu Kim, Maurício J. Piotrowski, Maurício J. Pri-  
1121        eto, and Germano Tremiliosi-Filho, *Reconstruction of core and surface nanopar-*  
1122        *ticles: The example of Pt55 and Au55*, Physical Review B - Condensed Matter  
1123        and Materials Physics **82** (2010), no. 20, 1–6.
- 1124 [14] Emir Dogdibegovic, Christopher J. Wright, and Xiao-Dong Zhou, *Stability and*  
1125        *Activity of  $(Pr_{1-x}Nd_x)_2NiO_4$  as Cathodes for Solid Oxide Fuel Cells: I. Quantifi-*  
1126        *cation of Phase Evolution in  $Pr_2NiO_4$* , Journal of the American Ceramic Society  
1127        **5** (2016), 1–5.
- 1128 [15] Simon Duane, A. D. Kennedy, Brian J. Pendleton, and Duncan Roweth, *Hybrid*  
1129        *Monte Carlo*, Physics Letters B **195** (1987), no. 2, 216–22.
- 1130 [16] Timur Dykhne, Ryan Taylor, Alastair Florence, and Simon J L Billinge, *Data*  
1131        *requirements for the reliable use of atomic pair distribution functions in amor-*  
1132        *phous pharmaceutical fingerprinting.*, Pharmaceutical research **28** (2011), no. 5,  
1133        1041–8.
- 1134 [17] C L Farrow, P Juhas, J W Liu, D Bryndin, E S Božin, J Bloch, Th Proffen, and  
1135        S J L Billinge, *PDFfit2 and PDFgui: computer programs for studying nanostruc-*  
1136        *ture in crystals.*, Journal of Physics. Condensed Matter : an Institute of Physics  
1137        journal **19** (2007), no. 33, 335219.
- 1138 [18] Christopher L Farrow and Simon J L Billinge, *Relationship between the atomic*  
1139        *pair distribution function and small-angle scattering: implications for modeling*

- 1140        *of nanoparticles.*, Acta Crystallographica Section A Foundations of Crystallography **65** (2009), no. Pt 3, 232–9 (en).
- 1142 [19] Riccardo Ferrando, Julius Jellinek, and Roy L Johnston, *Nanoalloys: From Theory to Applications of Alloy Clusters and Nanoparticles*, Chemical Reviews **108** (2008), no. 3, 846–904.
- 1145 [20] Anatoly Frenkel, *Solving the 3D structure of metal nanoparticles*, Zeitschrift für Kristallographie **222** (2007), no. 11, 605–611.
- 1147 [21] Carmelo Giacovazzo, Hugo Luis Monaco, Gilberto Artioli, Davide Viterbo, Marco Milanesio, Gastone Gilli, Paola Gilli, Giuseppe Zanotti, Giovanni Ferraris, and Michele Catti, *Fundamentals of Crystallography*, Oxford University Press, 1992.
- 1151 [22] Benjamin Gilbert, Jasmine J. Erbs, R. Lee Penn, Valeri Petkov, Dino Spagnoli, and Glenn A. Waychunas, *A disordered nanoparticle model for 6-line ferrihydrite*, American Mineralogist **98** (2013), no. 8-9, 1465–1476.
- 1154 [23] Benjamin Gilbert, Feng Huang, Hengzhong Zhang, Glenn A. Waychunas, and Jillian F Banfield, *Nanoparticles: strained and stiff.*, Science (New York, N.Y.) **305** (2004), no. 5684, 651–654.
- 1157 [24] Md Matthew D. Hoffman and Andrew Gelman, *The No-U-Turn Sampler: Adaptively Setting Path Lengths in Hamiltonian Monte Carlo*, The Journal of Machine Learning Research **15** (2014), no. 2008, 1593–1623.
- 1160 [25] W J Huang, R Sun, J Tao, L D Menard, R G Nuzzo, and J M Zuo, *Coordination-dependent surface atomic contraction in nanocrystals revealed by coherent diffraction.*, Nature Materials **7** (2008), no. 4, 308–313.
- 1163 [26] Pablo D Jadzinsky, Guillermo Calero, Christopher J Ackerson, David A Bushnell, and Roger D Kornberg, *Structure of a thiol monolayer-protected gold nanoparticle at 1.1 Å resolution.*, Science (New York, N.Y.) **318** (2007), no. 5849, 430–433.
- 1166 [27] I. K. Jeong, R. H. Heffner, M. J. Graf, and S. J. L. Billinge, *Lattice dynamics and correlated atomic motion from the atomic pair distribution function*, (2002), 9.
- 1169 [28] P. Juhás, T. Davis, C. L. Farrow, and S. J. L. Billinge, *PDFgetX3 : a rapid and highly automatable program for processing powder diffraction data into total*

- 1171        *scattering pair distribution functions*, Journal of Applied Crystallography **46**  
1172        (2013), no. 2, 560–566 (en).
- 1173 [29] A. Kassiba, M. Makowska-Janusik, J. Bouclé, J. Bardeau, A. Bulou, and  
1174        N. Herlin-Boime, *Photoluminescence features on the Raman spectra of quasistoi-*  
1175        *chiometric SiC nanoparticles: Experimental and numerical simulations*, Physical  
1176        Review B **66** (2002), no. 15, 1–7.
- 1177 [30] Jérôme Kieffer and Dimitrios Karkoulis, *PyFAI, a versatile library for azimuthal*  
1178        *regrouping*, Journal of Physics: Conference Series **425** (2013), 202012.
- 1179 [31] G. Kresse and OJ. Hafner, *Ab initio molecular-dynamics simulation of the liquid-*  
1180        *metal-amorphous-semiconductor transition in germanium*, Physical Review B **49**  
1181        (1994), no. 20, 14251–14269.
- 1182 [32] G. Kresse and J. Hafner, *Ab initio molecular dynamics for liquid metals*, Physical  
1183        Review B **47** (1993), no. 1, 558–561.
- 1184 [33] Yan Li, Giulia Galli, and François Gygi, *Electronic structure of thiolate-covered*  
1185        *gold nanoparticles: Au102(MBA)44*, ACS Nano **2** (2008), no. 9, 1896–1902.
- 1186 [34] L D Marks, *Experimental studies of small particle structures*, Reports on  
1187        Progress in Physics **57** (1994), no. 6, 603–649 (en).
- 1188 [35] A. S. Masadeh, E. S. Božin, C. L. Farrow, G. Paglia, P. Juhas, S. J. L. Billinge,  
1189        A. Karkamkar, and M. G. Kanatzidis, *Quantitative size-dependent structure and*  
1190        *strain determination of CdSe nanoparticles using atomic pair distribution func-*  
1191        *tion analysis*, Physical Review B - Condensed Matter and Materials Physics **76**  
1192        (2007), no. 11, 115413.
- 1193 [36] R L McGreevy and L Pusztai, *Reverse Monte Carlo Simulation: A New Tech-*  
1194        *nique for the Determination of Disordered Structures*, Molecular Simulation **1**  
1195        (1988), no. 6, 359–367.
- 1196 [37] Donald A. McQuarrie, *Statistical Mechanics*, University Science Books, Sausalito,  
1197        CA, 2000.
- 1198 [38] Radford M Neal, *Probabilistic Inference Using Markov Chain Monte Carlo Meth-*  
1199        *ods*, Intelligence **45** (1993), no. September, 144.

- 1200 [39] Radford M. Neal, *MCMC Using Hamiltonian Dynamics*, Handbook of Markov  
1201 Chain Monte Carlo (Steve Brooks, Andrew Gelman, Galin L. Jones and Xiao-Li  
1202 Meng, eds.), Chapman and Hall/CRC, 2011, pp. 113–162.
- 1203 [40] Katharine Page, Taylor C. Hood, Thomas Proffen, and Reinhard B. Neder,  
1204 *Building and refining complete nanoparticle structures with total scattering data*,  
1205 Journal of Applied Crystallography **44** (2011), no. 2, 327–336 (en).
- 1206 [41] B R Pauw, *Corrigendum: Everything SAXS: small-angle scattering pattern col-*  
1207 *lection and correction (2013 J. Phys.: Condens. Matter 25 383201)*, Journal of  
1208 Physics: Condensed Matter **26** (2014), no. 23, 239501.
- 1209 [42] Vitalij Pecharsky and Peter Zavalij, *Fundamentals of Powder Diffraction and*  
1210 *Structural Characterization of Materials*, Springer Science, 2009.
- 1211 [43] John P. Perdew, Kieron Burke, and Matthias Ernzerhof, *Generalized Gradient*  
1212 *Approximation Made Simple*, Physical Review Letters **77** (1996), no. 18, 3865–  
1213 3868.
- 1214 [44] Andrew A. Peterson, *Global optimization of adsorbate-surface structures while*  
1215 *preserving molecular identity*, Topics in Catalysis **57** (2014), no. 1-4, 40–53.
- 1216 [45] Valeri Petkov, Youngmin Lee, Shouheng Sun, and Yang Ren, *Noncrystallographic*  
1217 *atomic arrangement driven enhancement of the catalytic activity of Au nanoparticles*, Journal of Physical Chemistry C **116** (2012), no. 50, 26668–26673.
- 1219 [46] Valeri Petkov, Binay Prasai, Yang Ren, Shiyao Shan, Jin Luo, Pharrah Joseph,  
1220 and Chuan-Jian Zhong, *Solving the nanostructure problem: exemplified on metal-*  
1221 *alloy nanoparticles*, Nanoscale **6** (2014), no. 17, 1–11.
- 1222 [47] Valeri Petkov, Shiyao Shan, Peter Chupas, Jun Yin, Lefu Yang, Jin Luo, and  
1223 Chuan-Jian Zhong, *Noble-transition metal nanoparticle breathing in a reactive*  
1224 *gas atmosphere.*, Nanoscale **5** (2013), no. 16, 7379–87.
- 1225 [48] Th. Proffen and R. B. Neder, *DISCUS: a Program for Diffuse Scattering and*  
1226 *Defect-Structure Simulation*, Journal of Applied Crystallography **30** (1997), 171–  
1227 175.
- 1228 [49] Erin L. Redmond, Brian P. Setzler, Pavol Juhas, Simon J. L. Billinge, and  
1229 Thomas F. Fuller, *In-Situ Monitoring of Particle Growth at PEMFC Cathode*  
1230 *under Accelerated Cycling Conditions*, Electrochemical and Solid-State Letters  
1231 **15** (2012), no. 5, B72 (en).

- 1232 [50] H. W. Sheng, M. J. Kramer, A. Cadien, T. Fujita, and M. W. Chen, *Highly*  
1233      *optimized embedded-atom-method potentials for fourteen FCC metals*, Physical  
1234      Review B - Condensed Matter and Materials Physics **83** (2011), no. 13, 134118.
- 1235 [51] Chenyang Shi, Majid Beidaghi, Michael Naguib, Olha Mashtalir, Yury Gogotsi,  
1236      and Simon J L Billinge, *Structure of Nanocrystalline Ti<sub>3</sub>C<sub>2</sub> MXene Using Atomic*  
1237      *Pair Distribution Function.*, Physical Review Letters **112** (2014), no. March,  
1238      125501.
- 1239 [52] Randall Q. Snurr, Alexis T. Bell, and Doros N. Theodorou, *Prediction of ad-*  
1240      *sorption of aromatic hydrocarbons in silicalite from grand canonical Monte Carlo*  
1241      *simulations with biased insertions*, The Journal of Physical Chemistry **97** (1993),  
1242      no. 51, 13742–13752 (EN).
- 1243 [53] Chang Q. Sun, *Size dependence of nanostructures: Impact of bond order defi-*  
1244      *ciency*, Progress in Solid State Chemistry **35** (2007), no. 1, 1–159.
- 1245 [54] X. Yang, P. Juhás, and S. J L Billinge, *On the estimation of statistical uncertain-*  
1246      *ties on powder diffraction and small-angle scattering data from two-dimensional*  
1247      *X-ray detectors*, Journal of Applied Crystallography **47** (2014), no. 4, 1273–1283.
- 1248 [55] Masatomo Yashima, Makiko Enoki, Takahiro Wakita, Roushown Ali, Yoshitaka  
1249      Matsushita, Fujio Izumi, and Tatsumi Ishihara, *Structural Disorder and Dif-*  
1250      *fusional Pathway of Oxide Ions in a Doped Pr<sub>2</sub>NiO<sub>4</sub> -Based Mixed Conductor*,  
1251      Journal of the American Chemical Society **130** (2008), no. 9, 2762–2763.
- 1252 [56] Hengzhong Zhang, Bin Chen, Jillian F. Banfield, and Glenn A. Waychunas,  
1253      *Atomic structure of nanometer-sized amorphous TiO<sub>2</sub>*, Physical Review B **78**  
1254      (2008), no. 21, 214106.
- 1255 [57] X.-D. Zhou, J.W. Templeton, Z. Nie, H. Chen, J.W. Stevenson, and L.R. Pedersen,  
1256      *Electrochemical performance and stability of the cathode for solid oxide fuel*  
1257      *cells: V. high performance and stable Pr<sub>2</sub>NiO<sub>4</sub> as the cathode for solid oxide fuel*  
1258      *cells*, Electrochimica Acta **71** (2012), 44–49.

1259

## APPENDIX A

1260

SUPPLEMENTAL INFORMATION: PHASE CHANGES AND

1261

ANNEALING DYNAMICS OF  $\text{Pr}_2\text{NiO}_4$  AND ITS

1262

DERIVATIVES

1263 **Intra Sample Comparison**

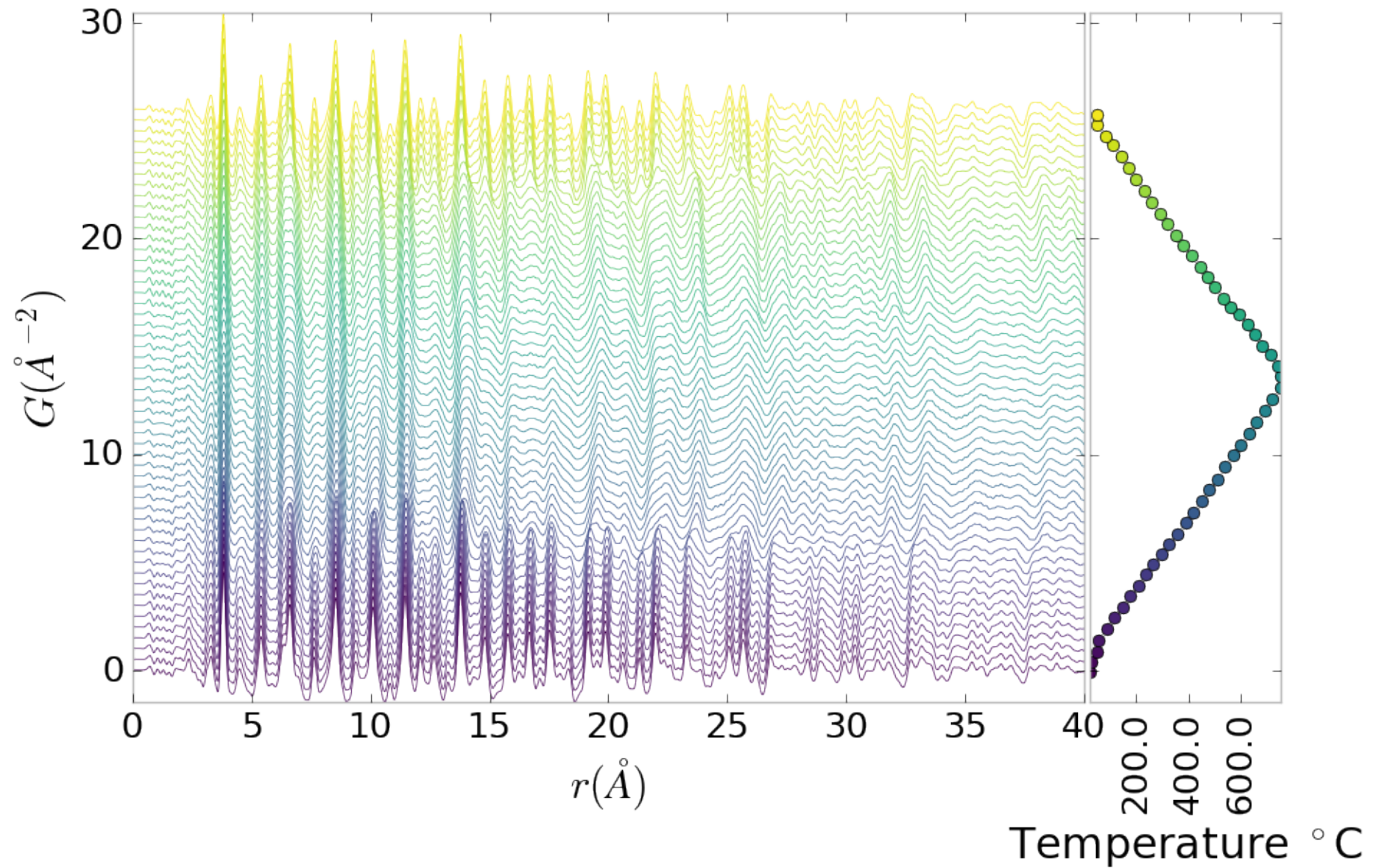


Figure A.1: PDF as a function of temperature for PNO annealed at  $750 \text{ }^{\circ}\text{C}$  for 50 hours showing the full PDF

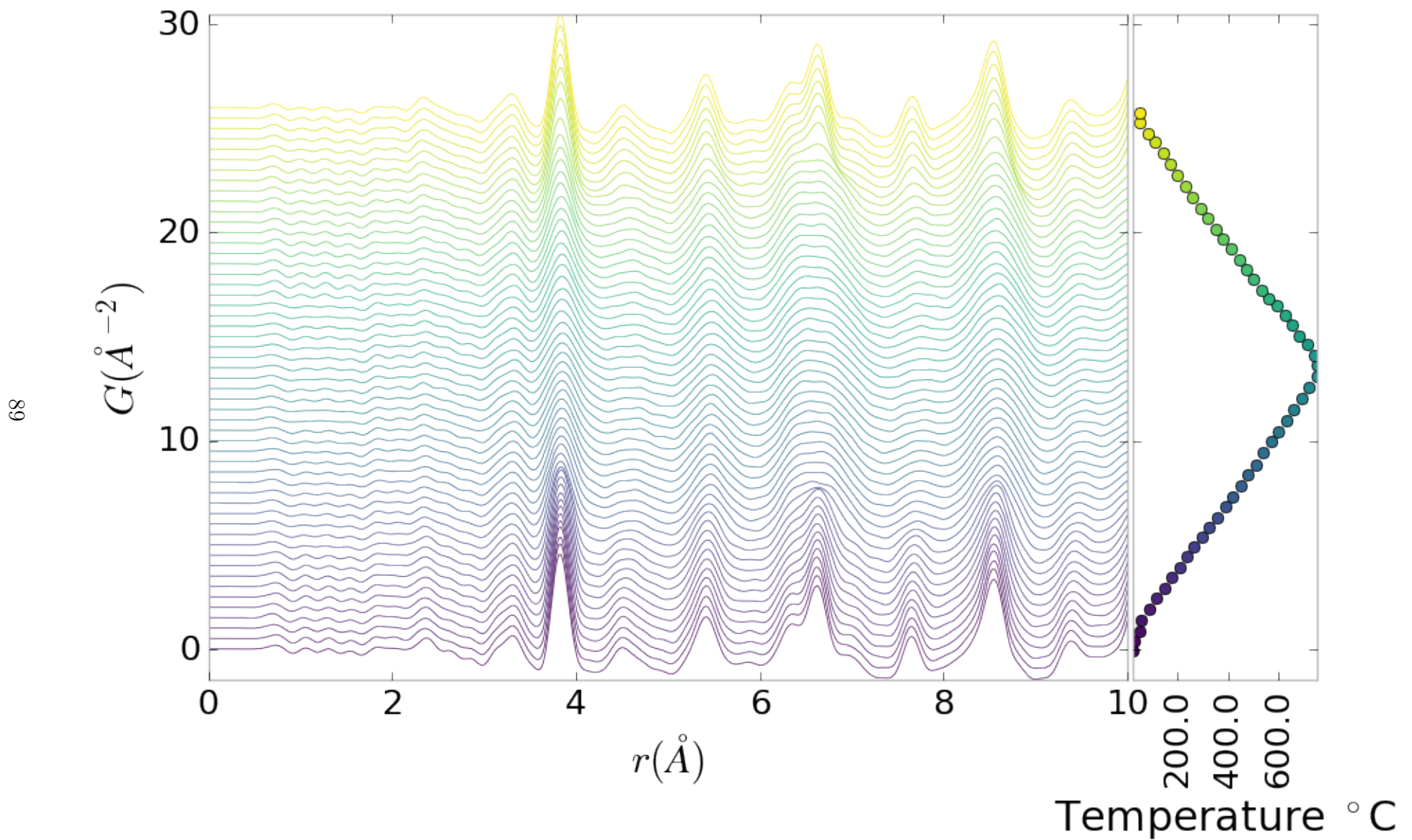


Figure A.2: PDF as a function of temperature for PNO annealed at 750 °C for 50 hours showing a close up on the short range section

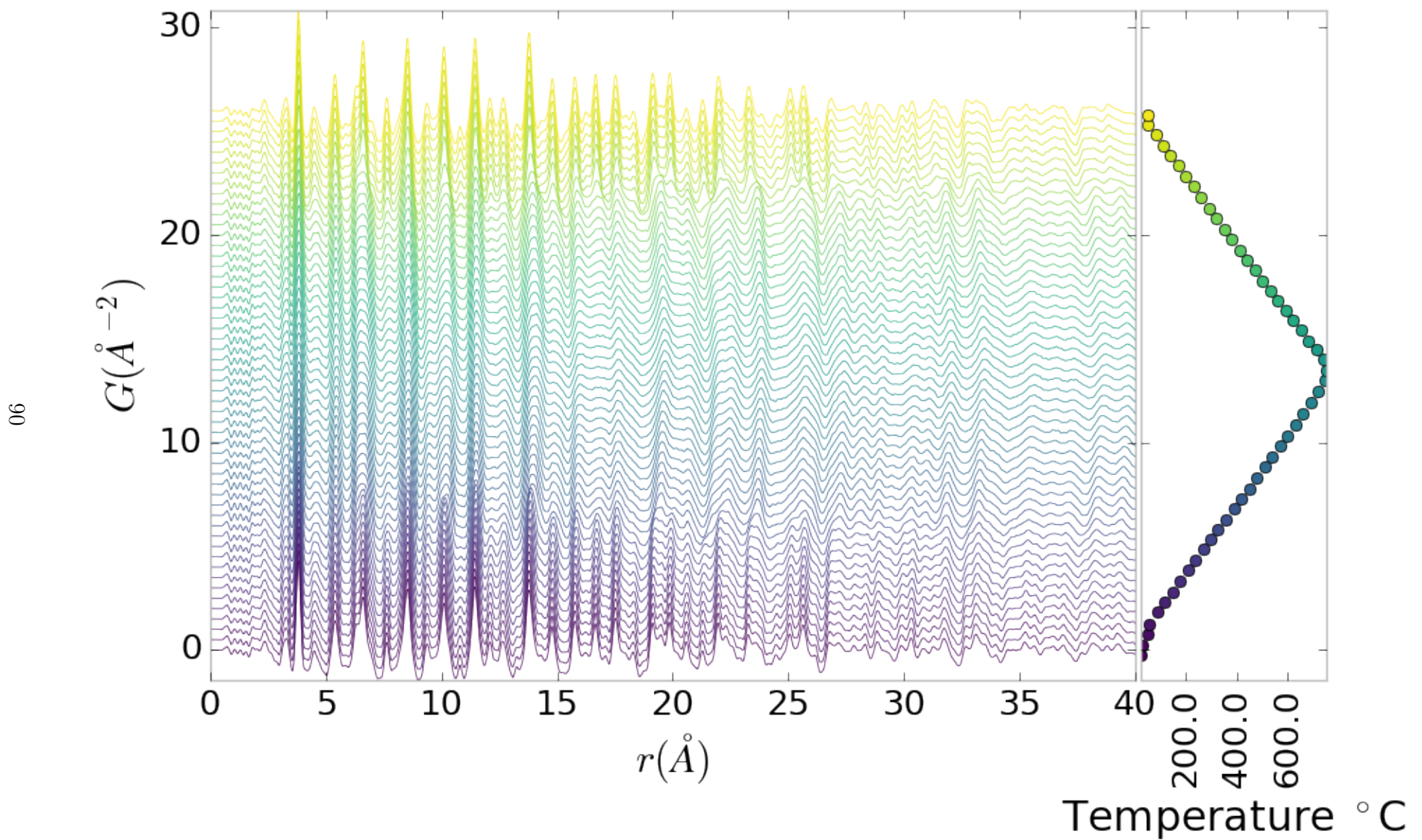


Figure A.3: PDF as a function of temperature for PNO annealed at 750 °C for 100 hours showing the full PDF

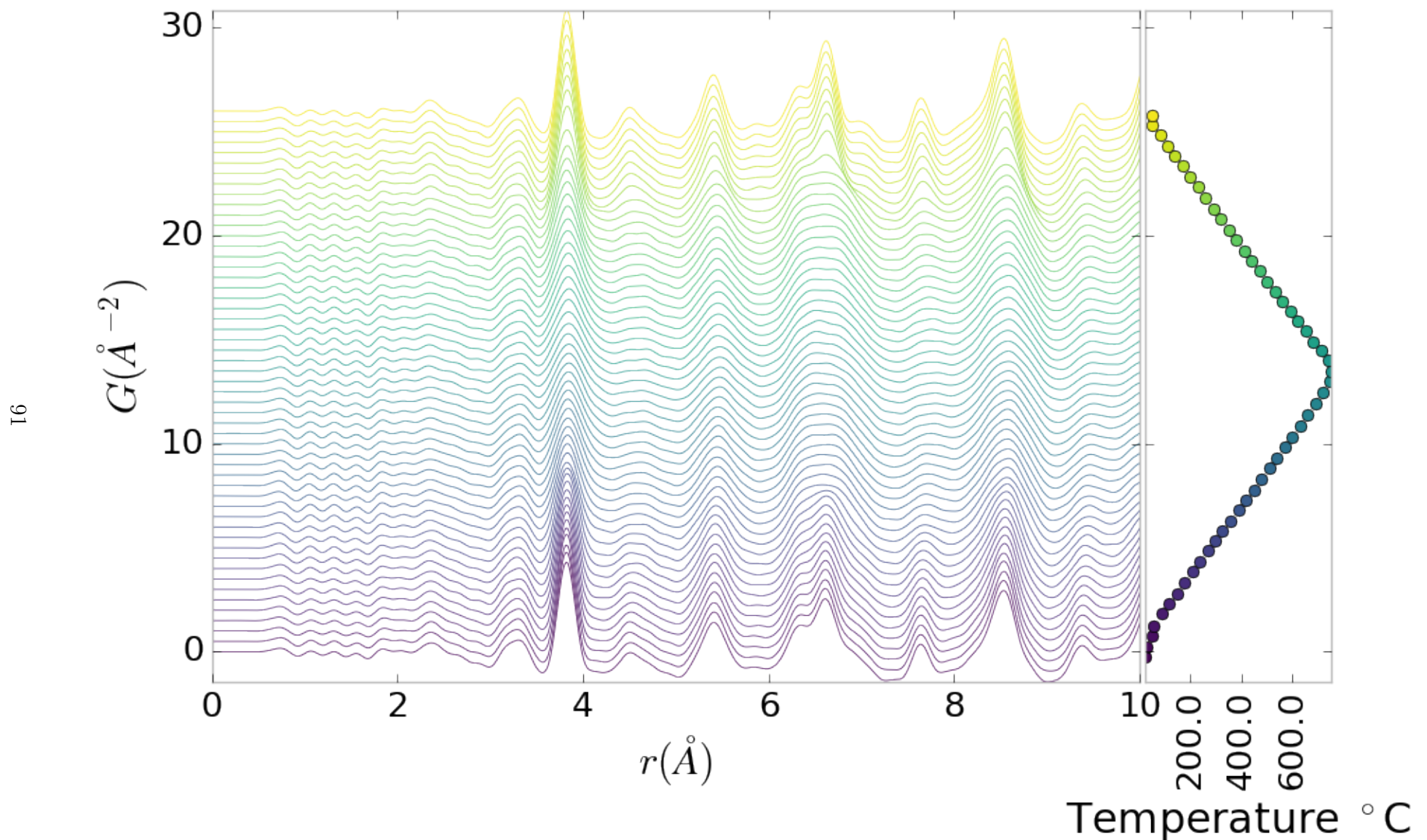


Figure A.4: PDF as a function of temperature for PNO annealed at 750  $^{\circ}\text{C}$  for 100 hours showing a close up on the short range section

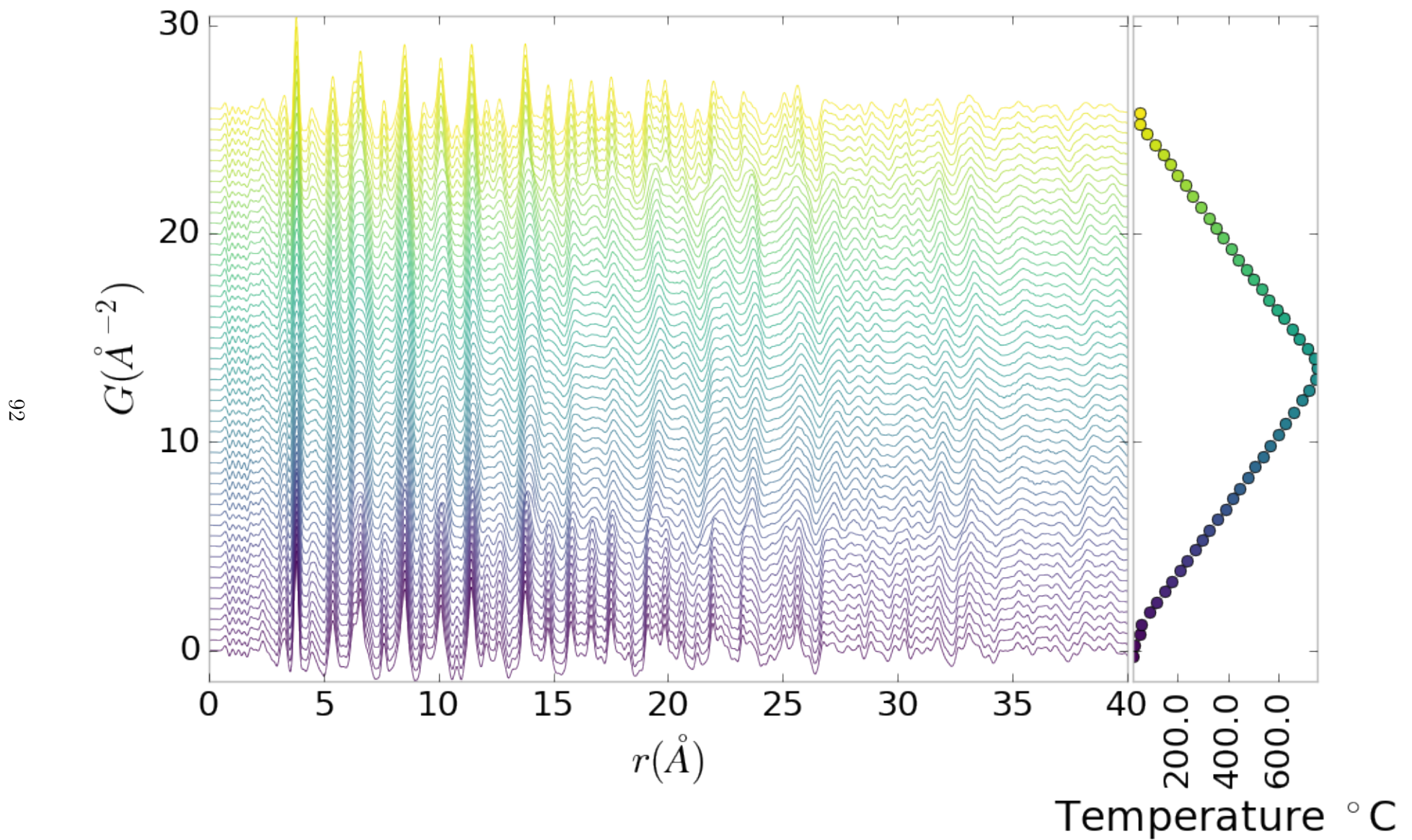


Figure A.5: PDF as a function of temperature for PNO annealed at 750 °C for 200 hours showing the full PDF

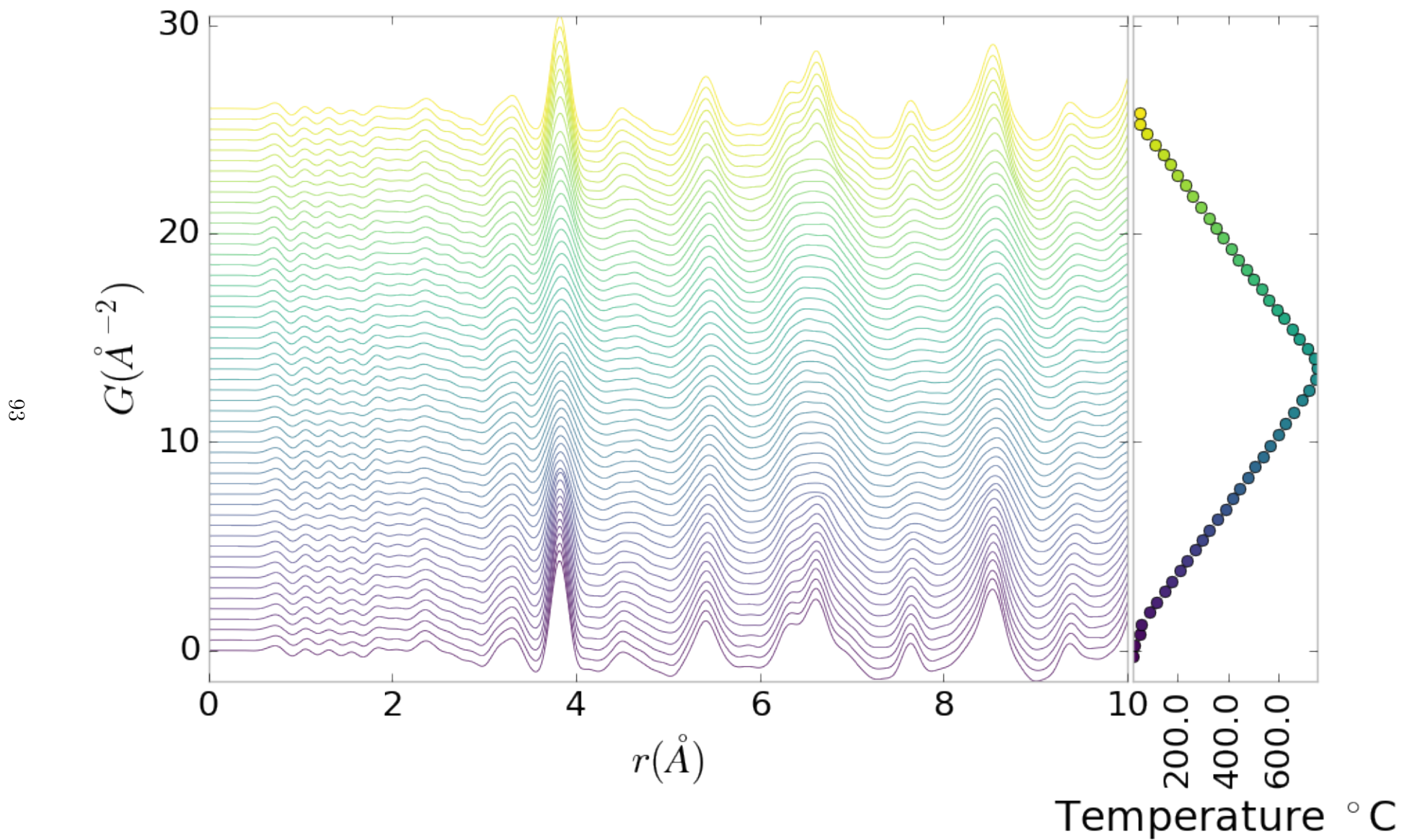


Figure A.6: PDF as a function of temperature for PNO annealed at 750 °C for 200 hours showing a close up on the short range section

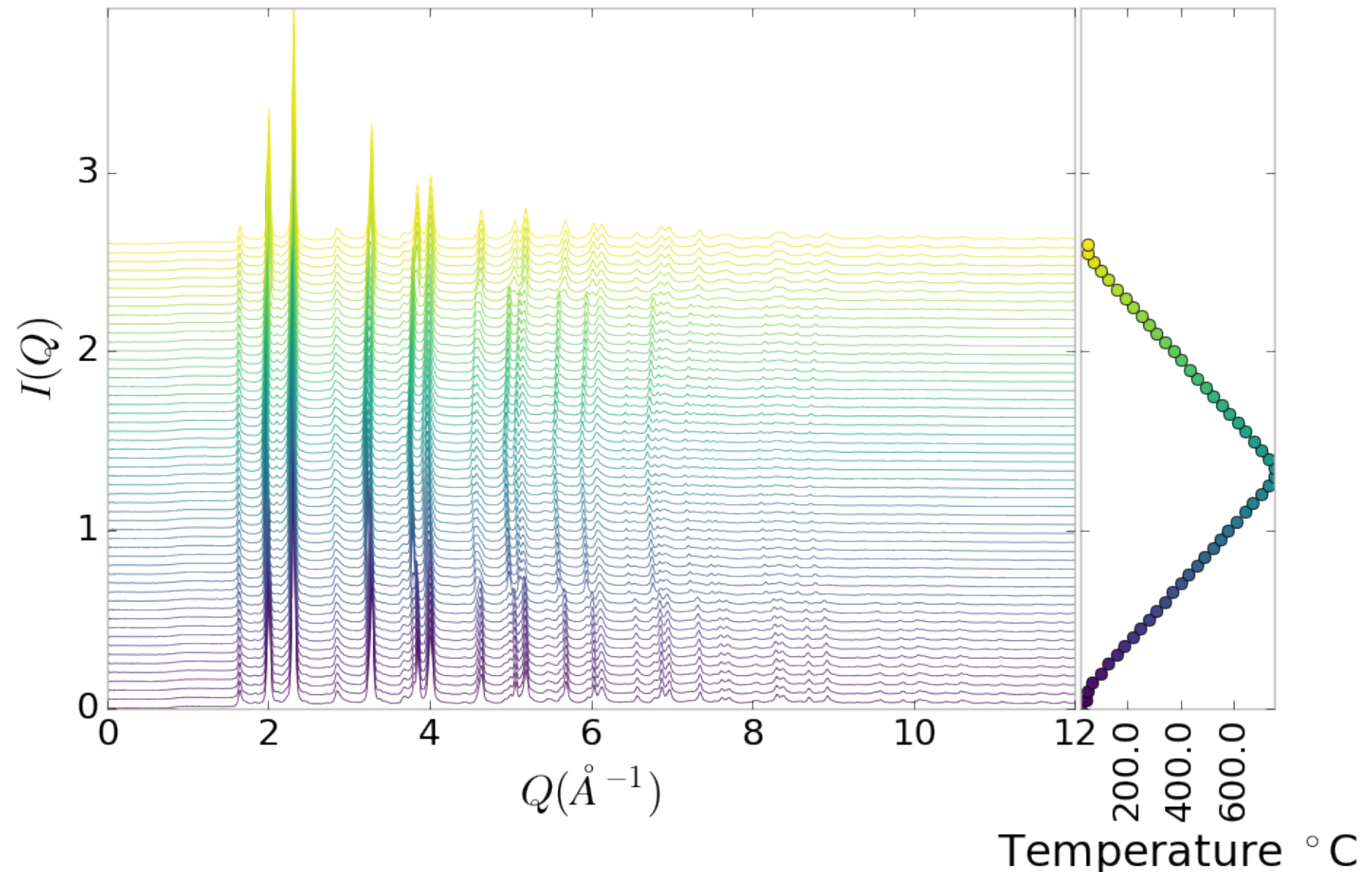


Figure A.7:  $I(Q)$  as a function of temperature for PNO annealed at 750 °C for 50 hours showing the full XRD

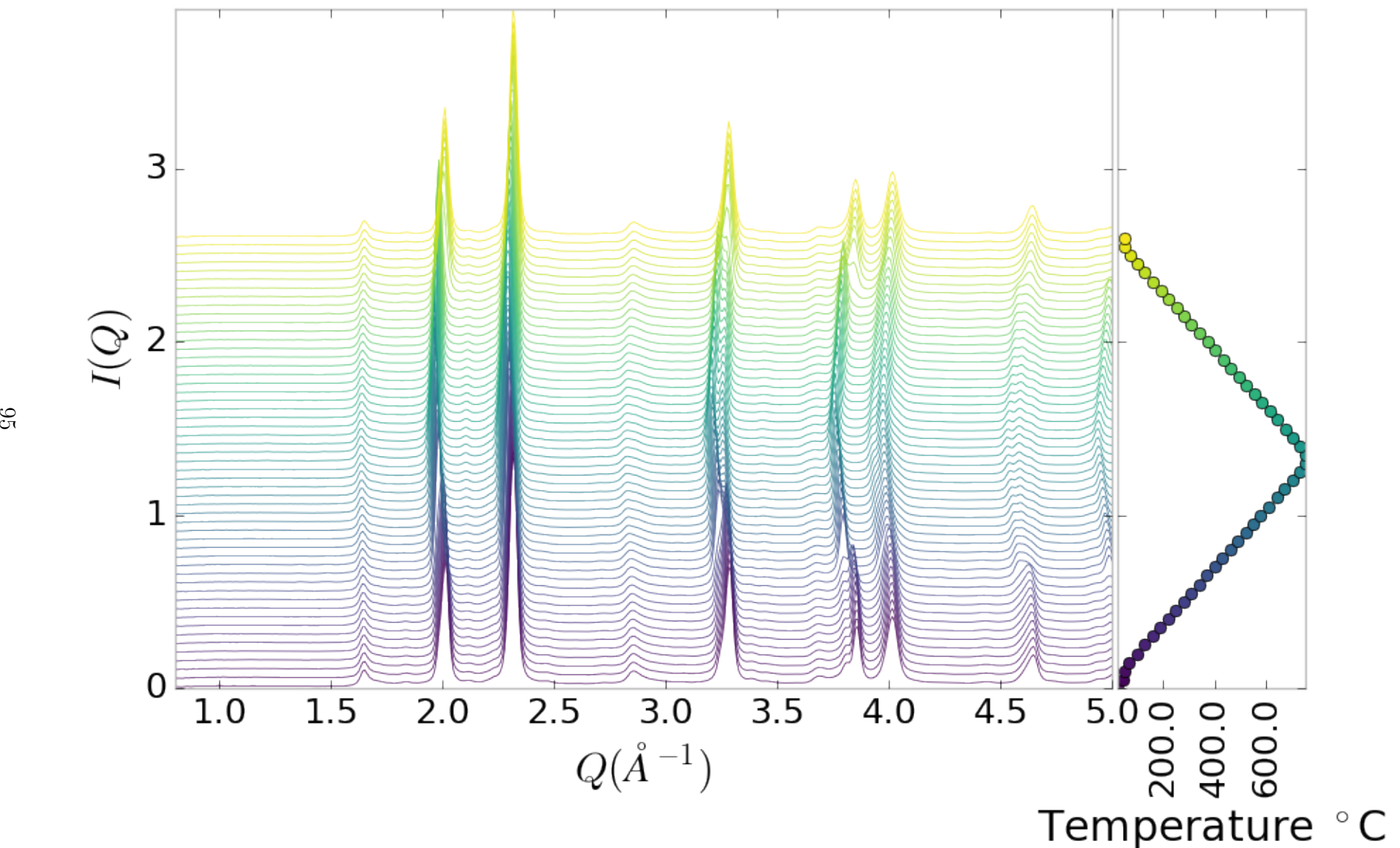


Figure A.8:  $I(Q)$  as a function of temperature for PNO annealed at 750  $^{\circ}\text{C}$  for 50 hours showing a close up on the low  $Q$  section

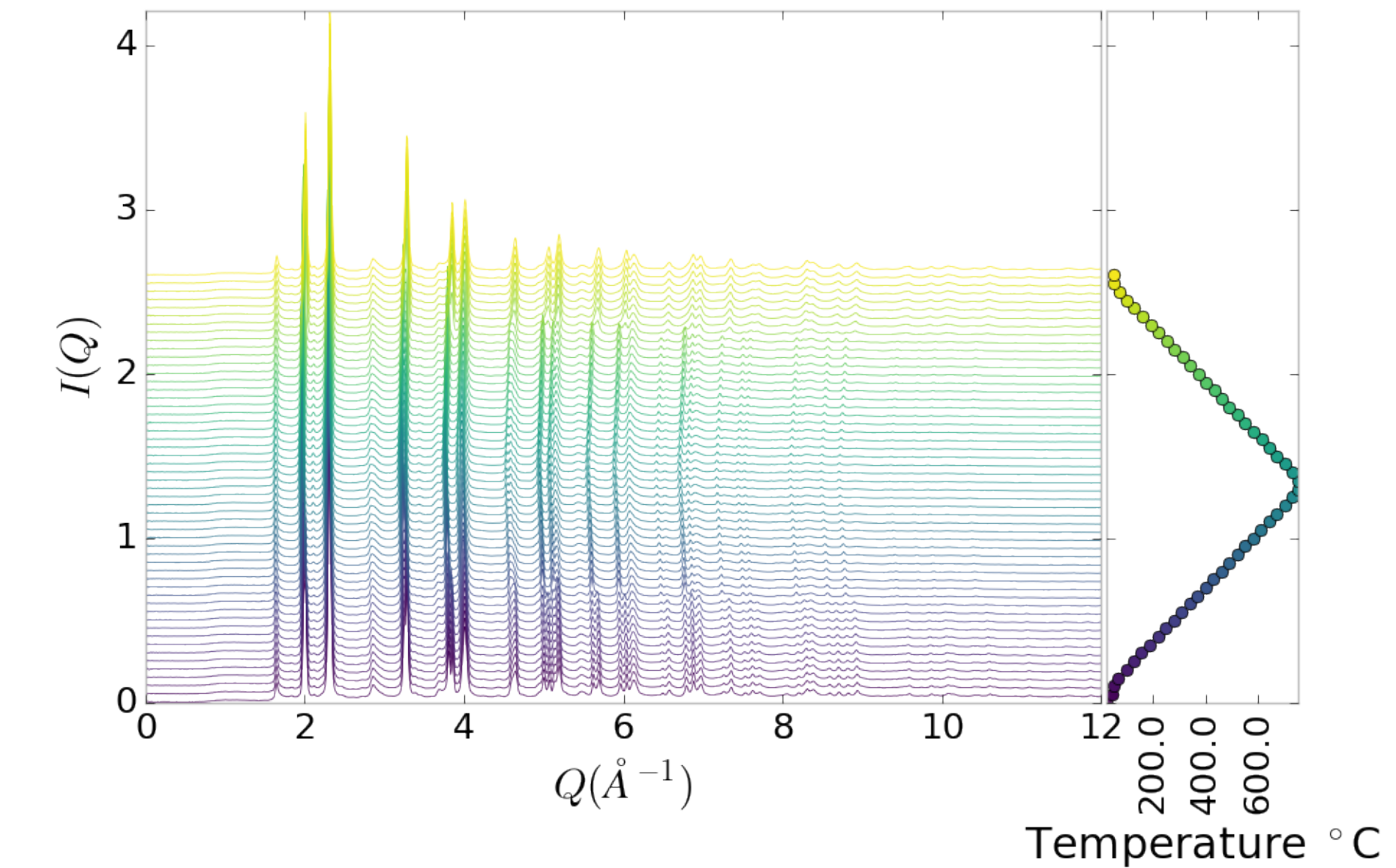


Figure A.9:  $I(Q)$  as a function of temperature for PNO annealed at 750 °C for 100 hours showing the full XRD

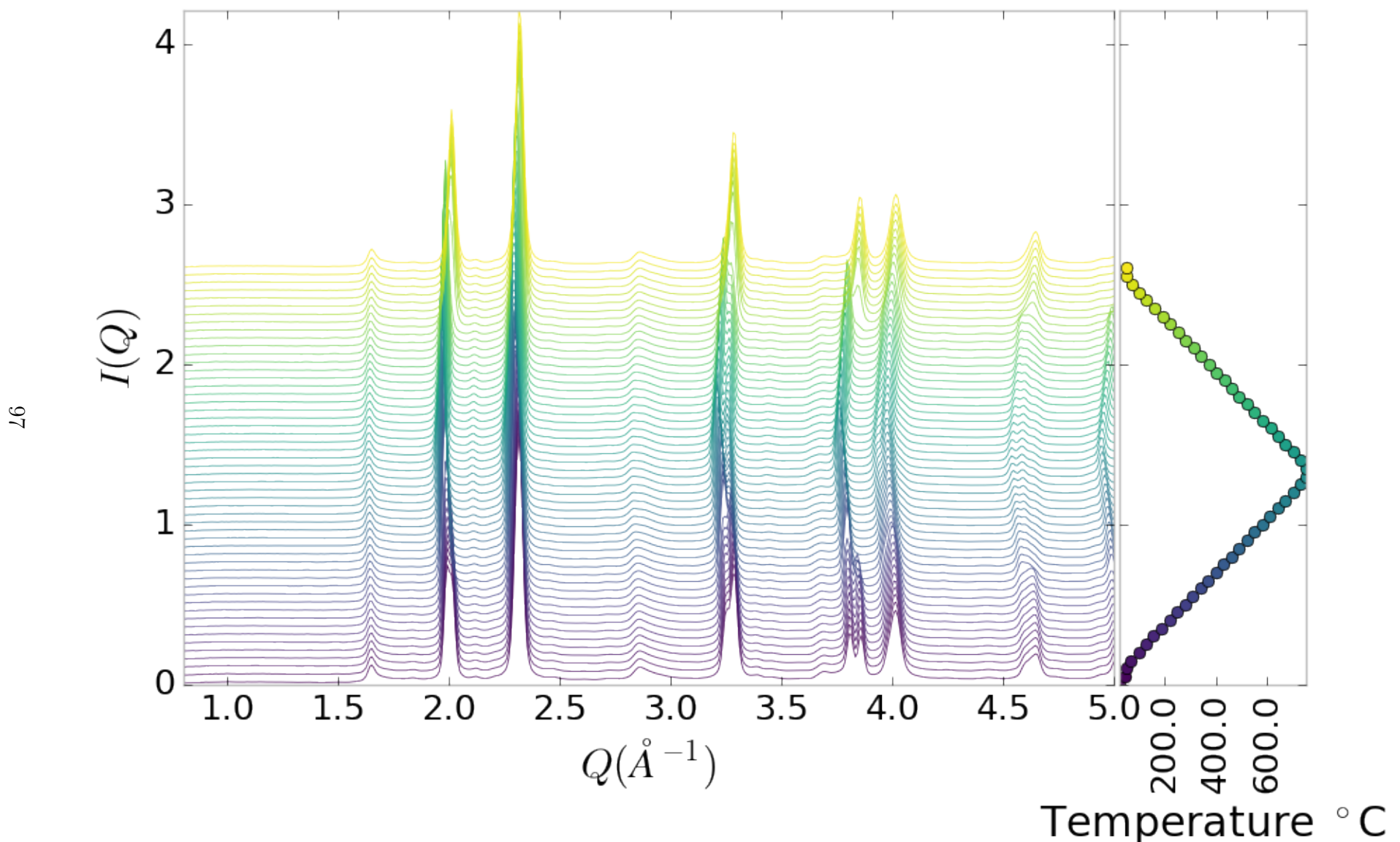


Figure A.10:  $I(Q)$  as a function of temperature for PNO annealed at 750 °C for 100 hours showing a close up on the low  $Q$  section

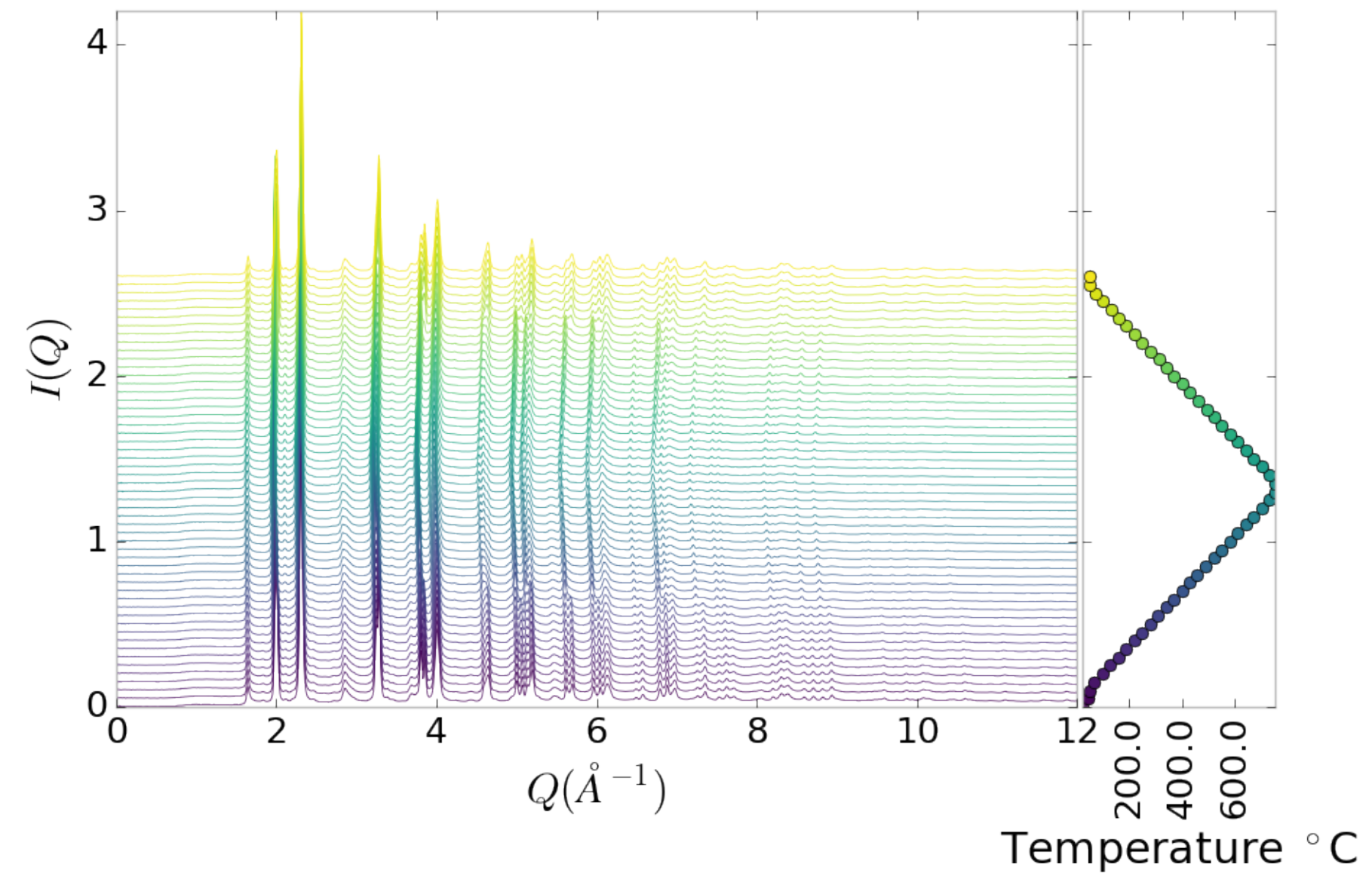


Figure A.11:  $I(Q)$  as a function of temperature for PNO annealed at 750 °C for 200 hours showing the full XRD

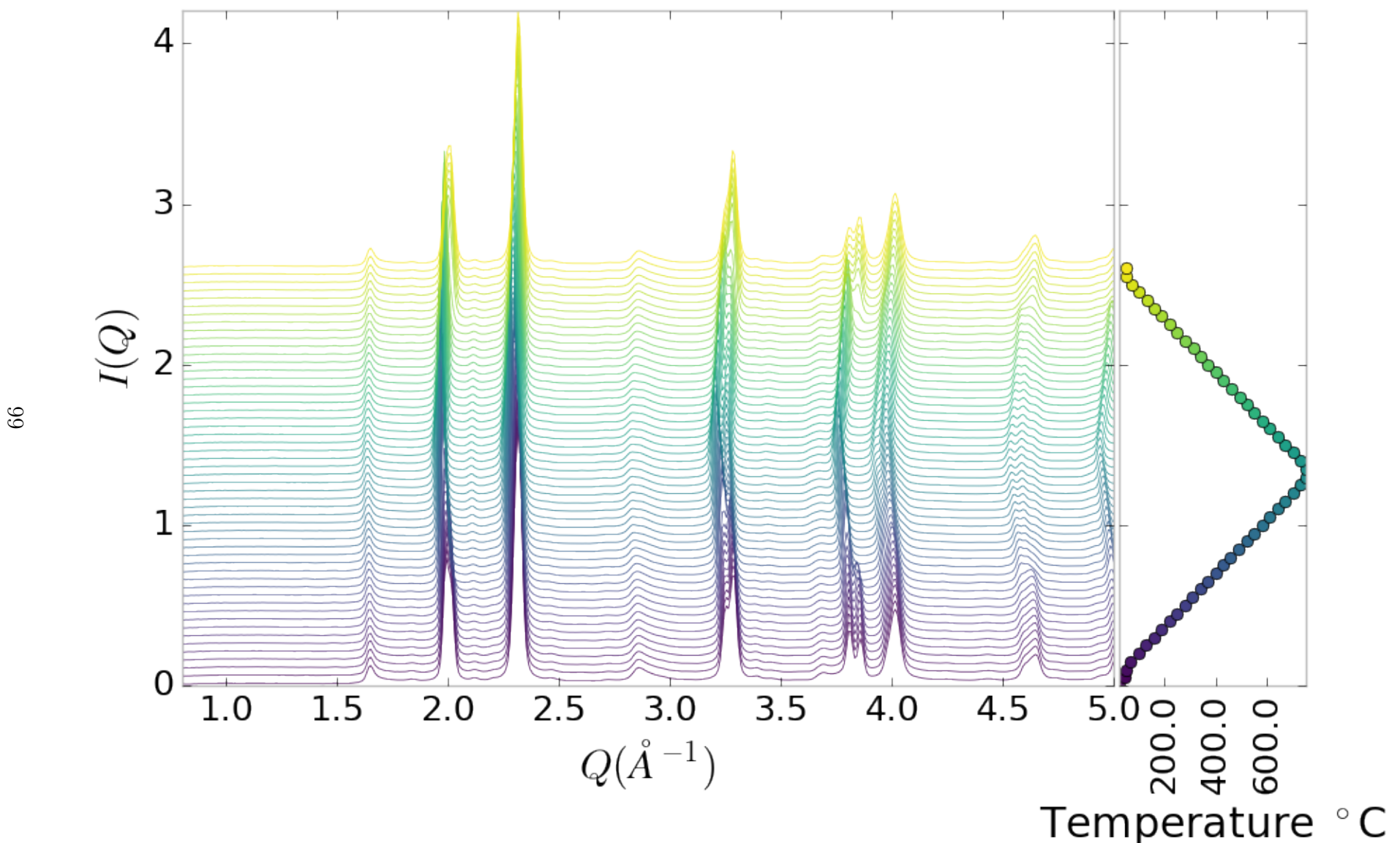


Figure A.12:  $I(Q)$  as a function of temperature for PNO annealed at  $750 \text{ }^{\circ}\text{C}$  for 200 hours showing a close up on the low  $Q$  section

<sup>1264</sup> Inter Sample Comparison

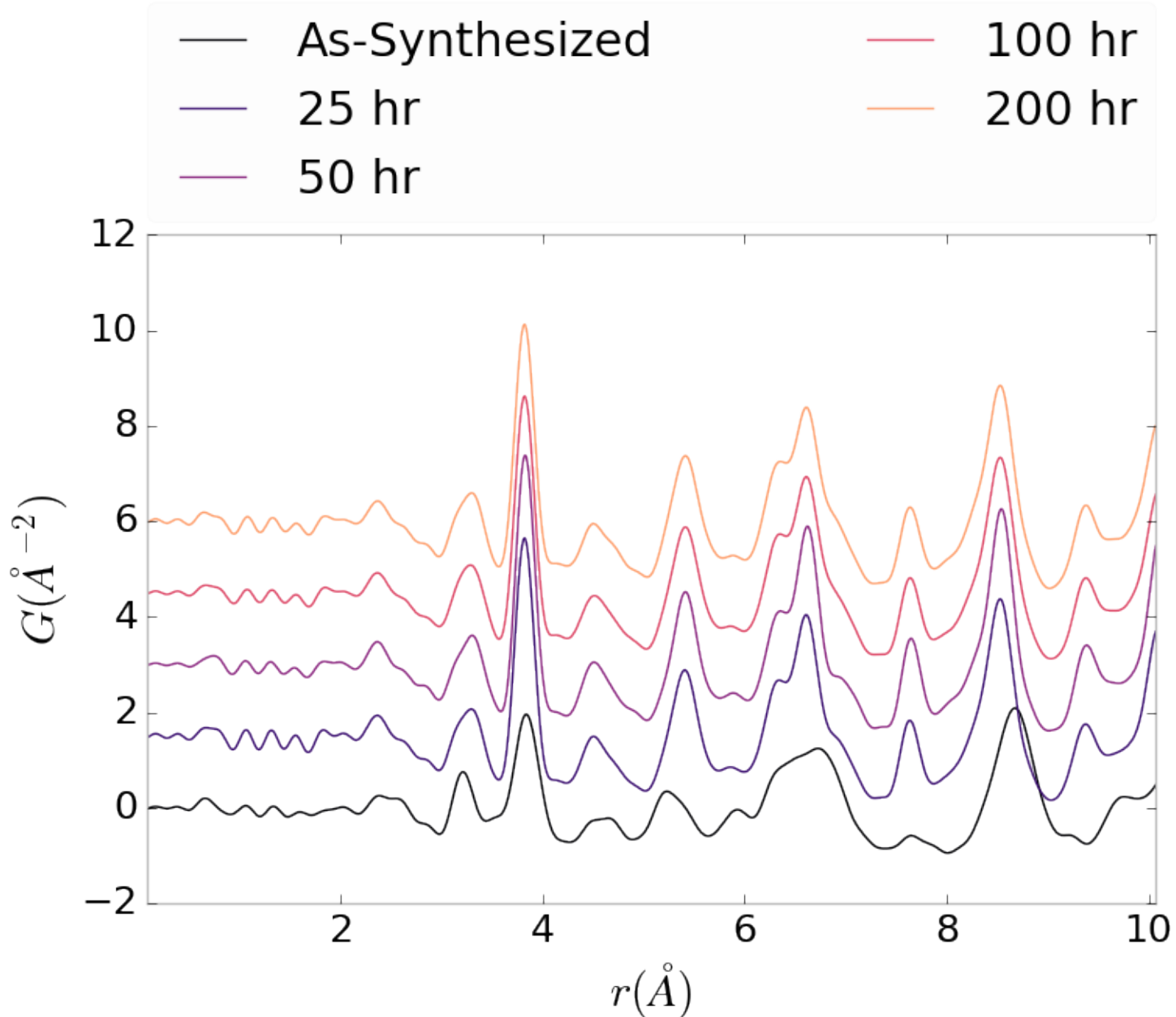


Figure A.13: Comparison of PNO sample PDFs as a function of annealing time at room temperature

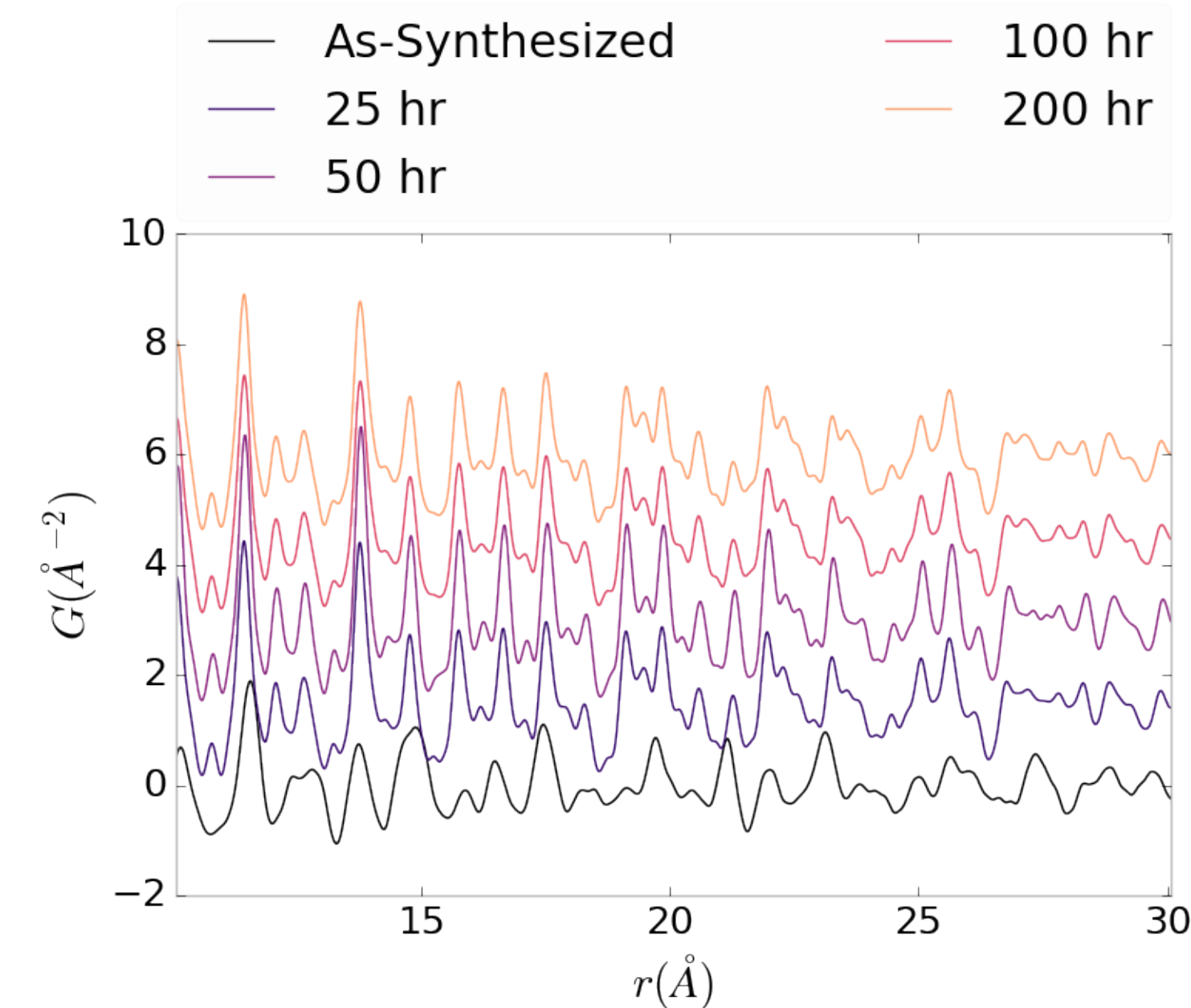


Figure A.14: Comparison of PNO sample PDFs as a function of annealing time at room temperature

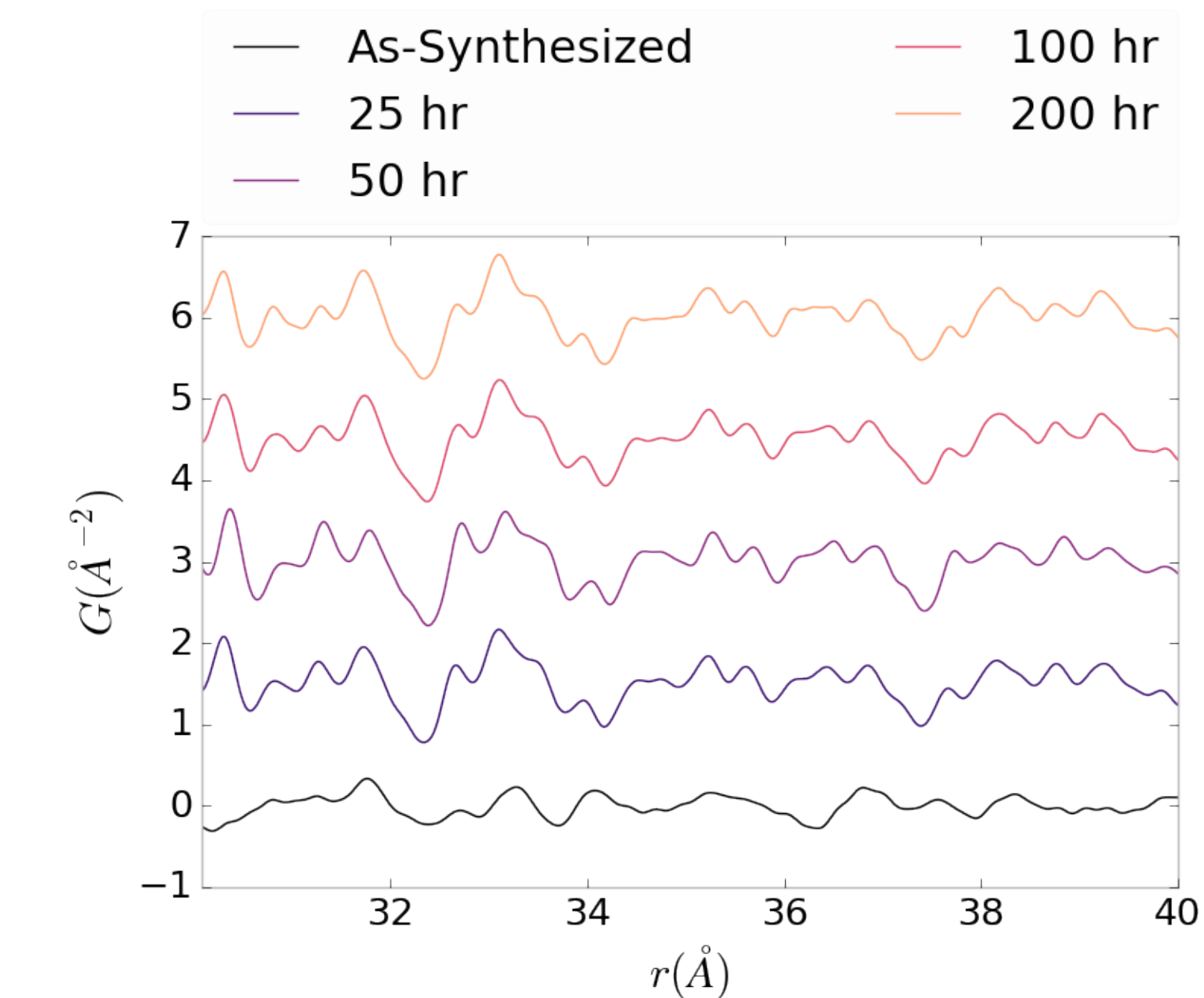


Figure A.15: Comparison of PNO sample PDFs as a function of annealing time at room temperature

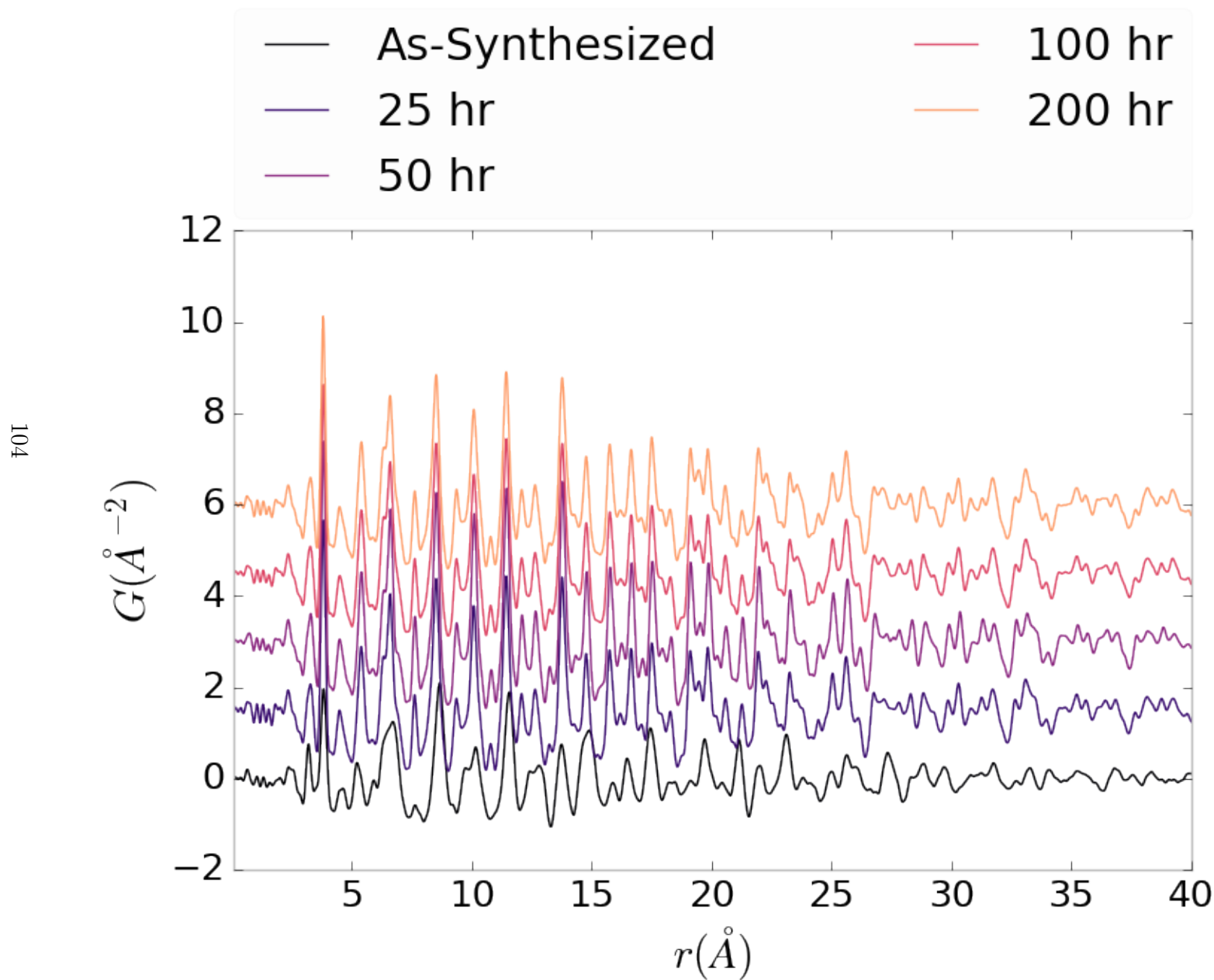


Figure A.16: Comparison of PNO sample PDFs as a function of annealing time at room temperature

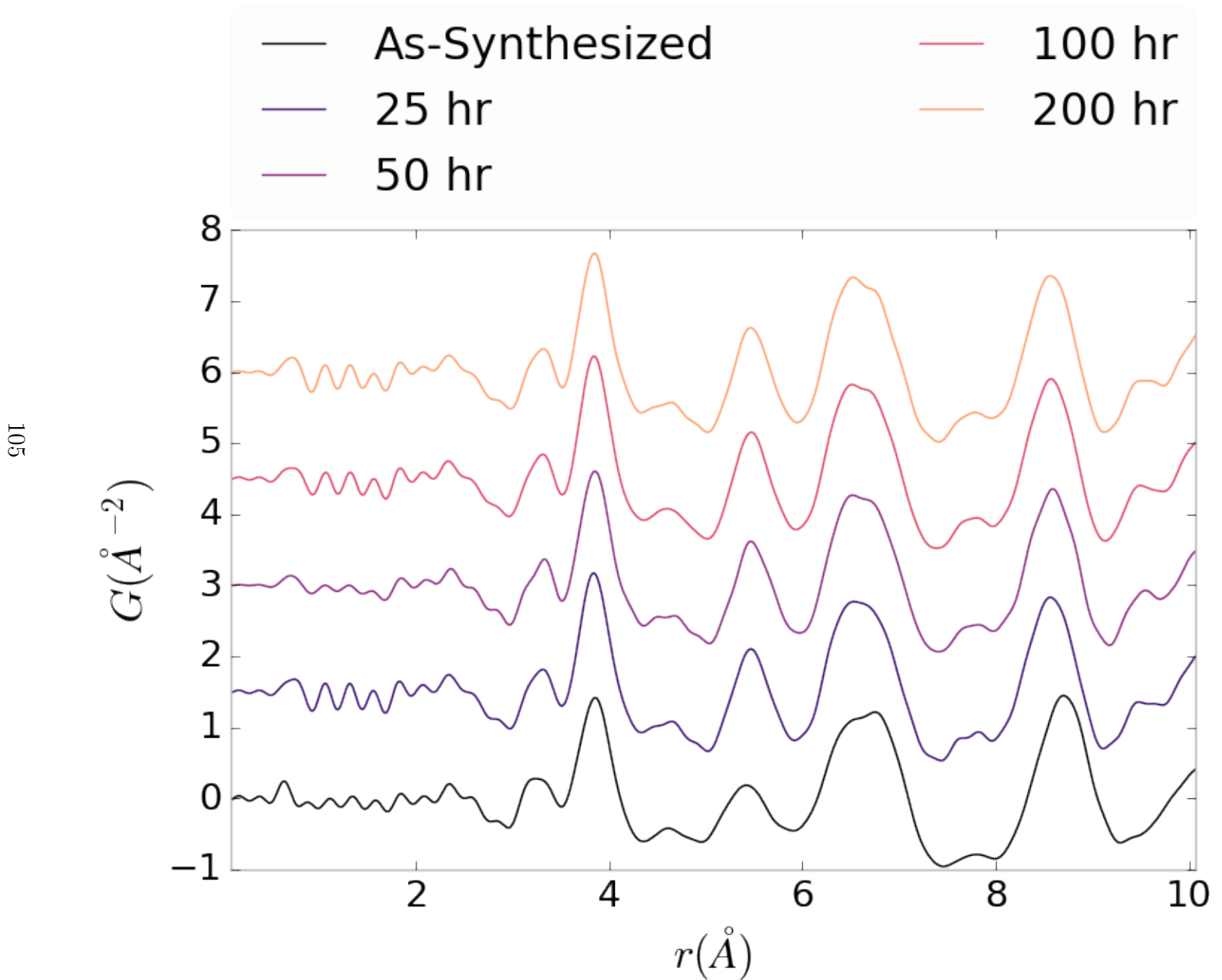


Figure A.17: Comparison of PNO sample PDFs as a function of annealing time at operating temperature

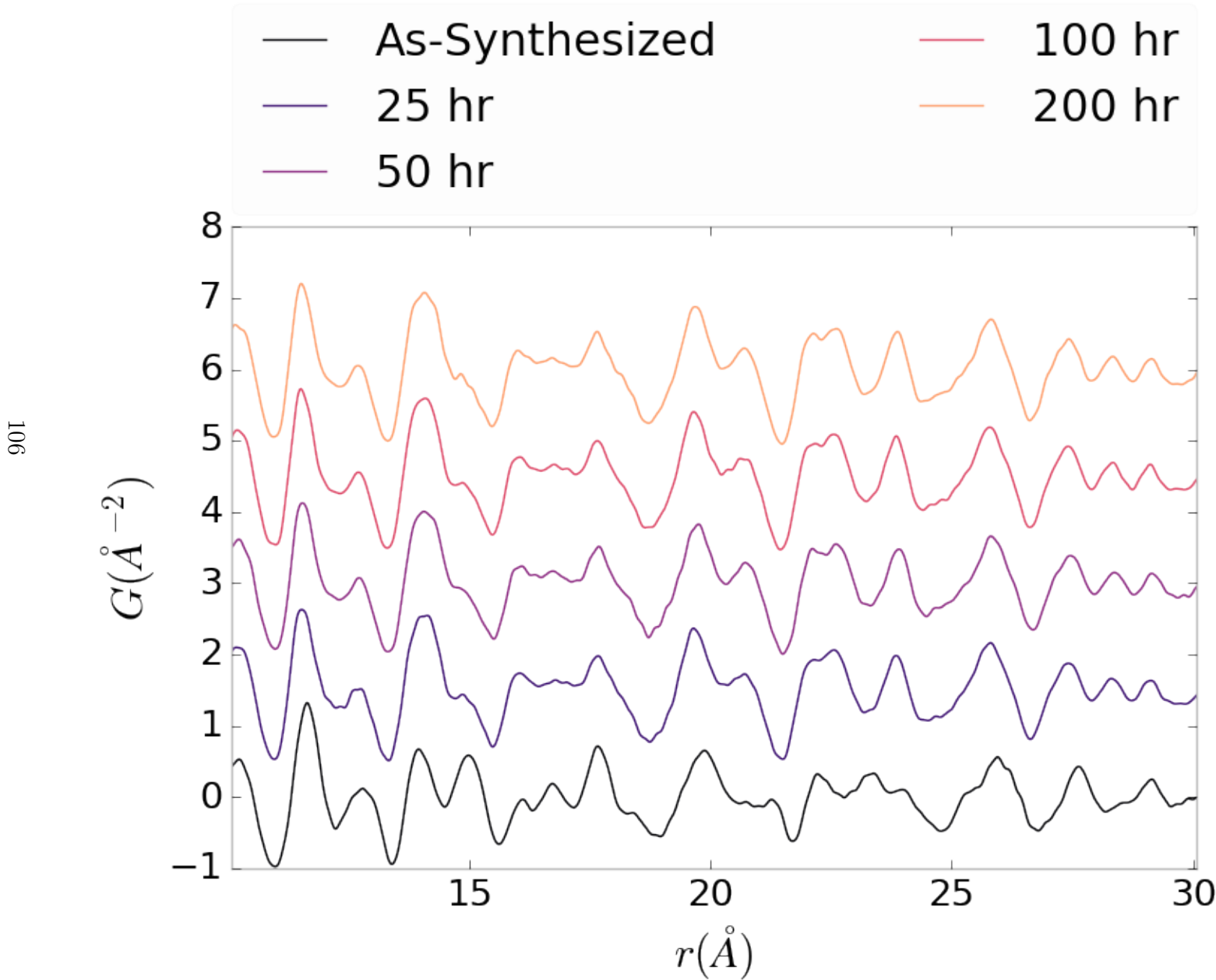


Figure A.18: Comparison of PNO sample PDFs as a function of annealing time at operating temperature

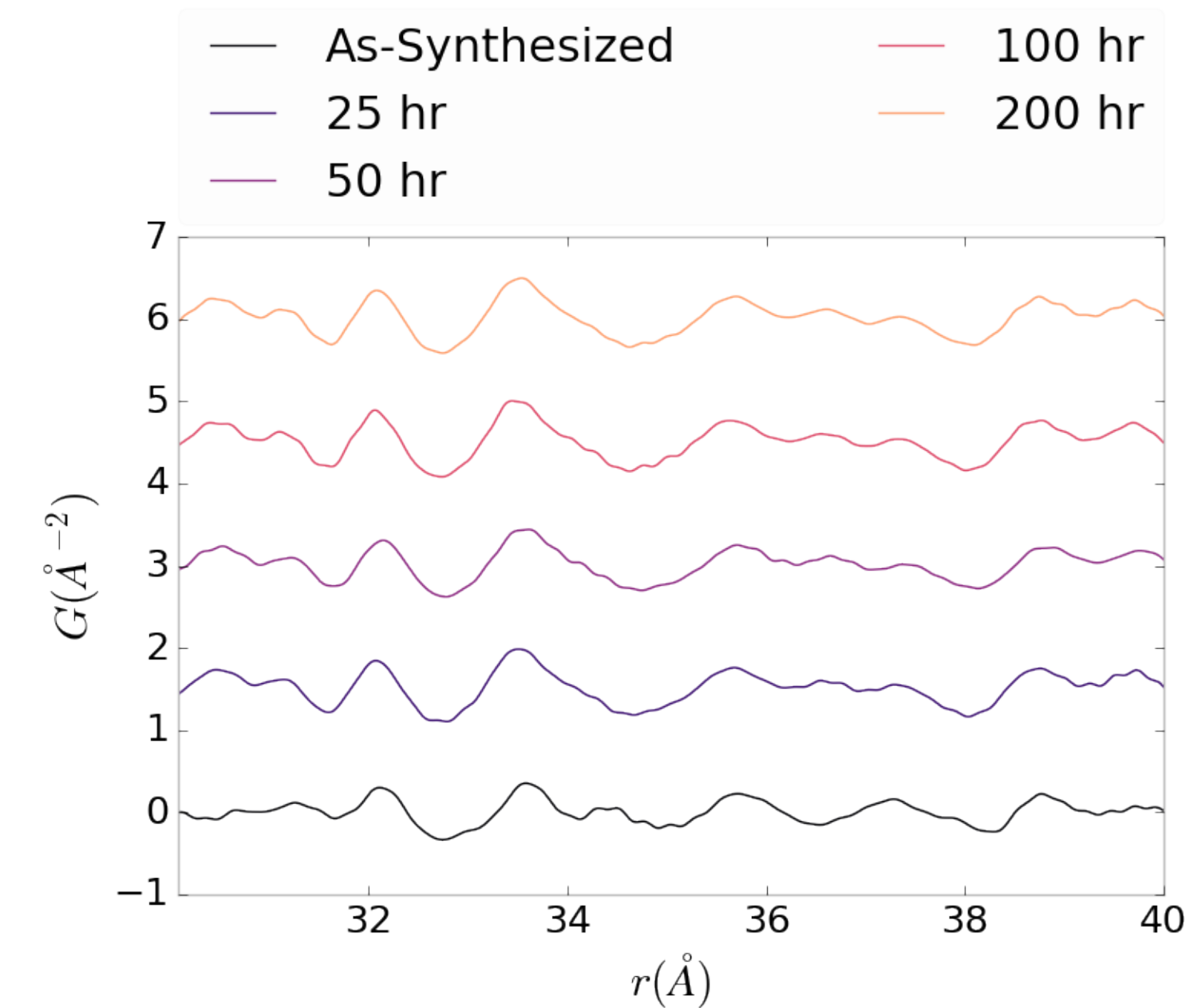


Figure A.19: Comparison of PNO sample PDFs as a function of annealing time at operating temperature

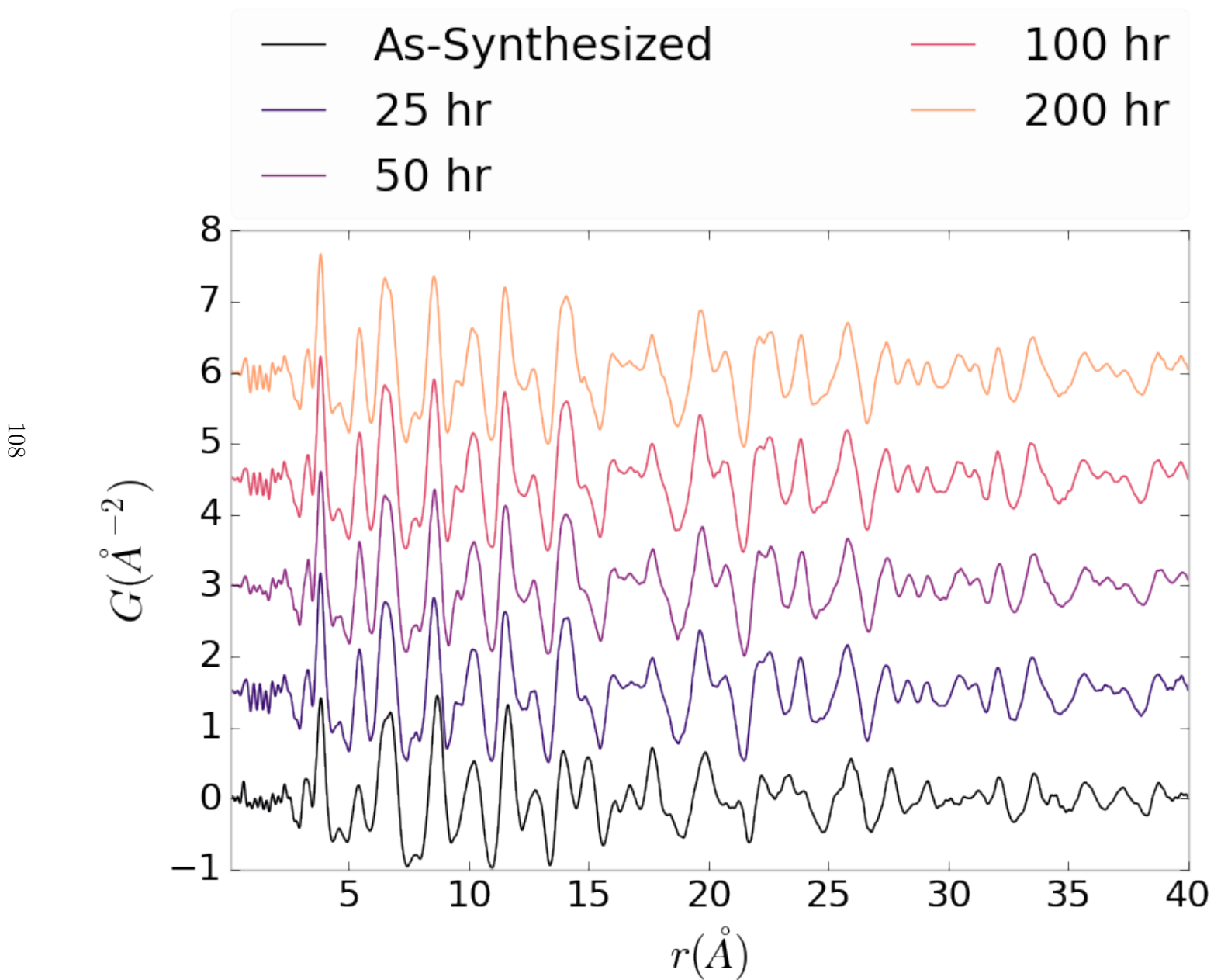


Figure A.20: Comparison of PNO sample PDFs as a function of annealing time at operating temperature

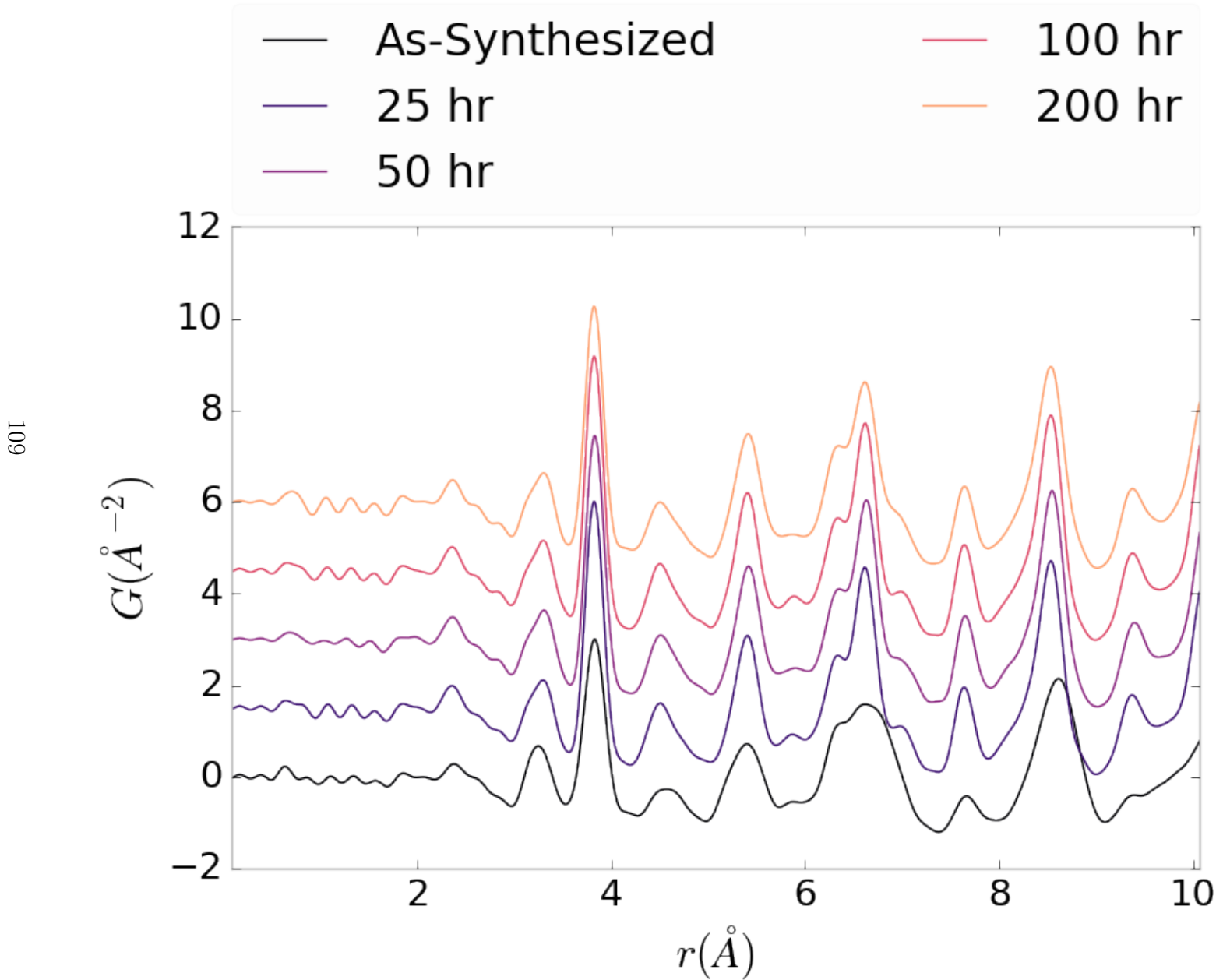


Figure A.21: Comparison of PNO sample PDFs as a function of annealing time cooled back to room temperature

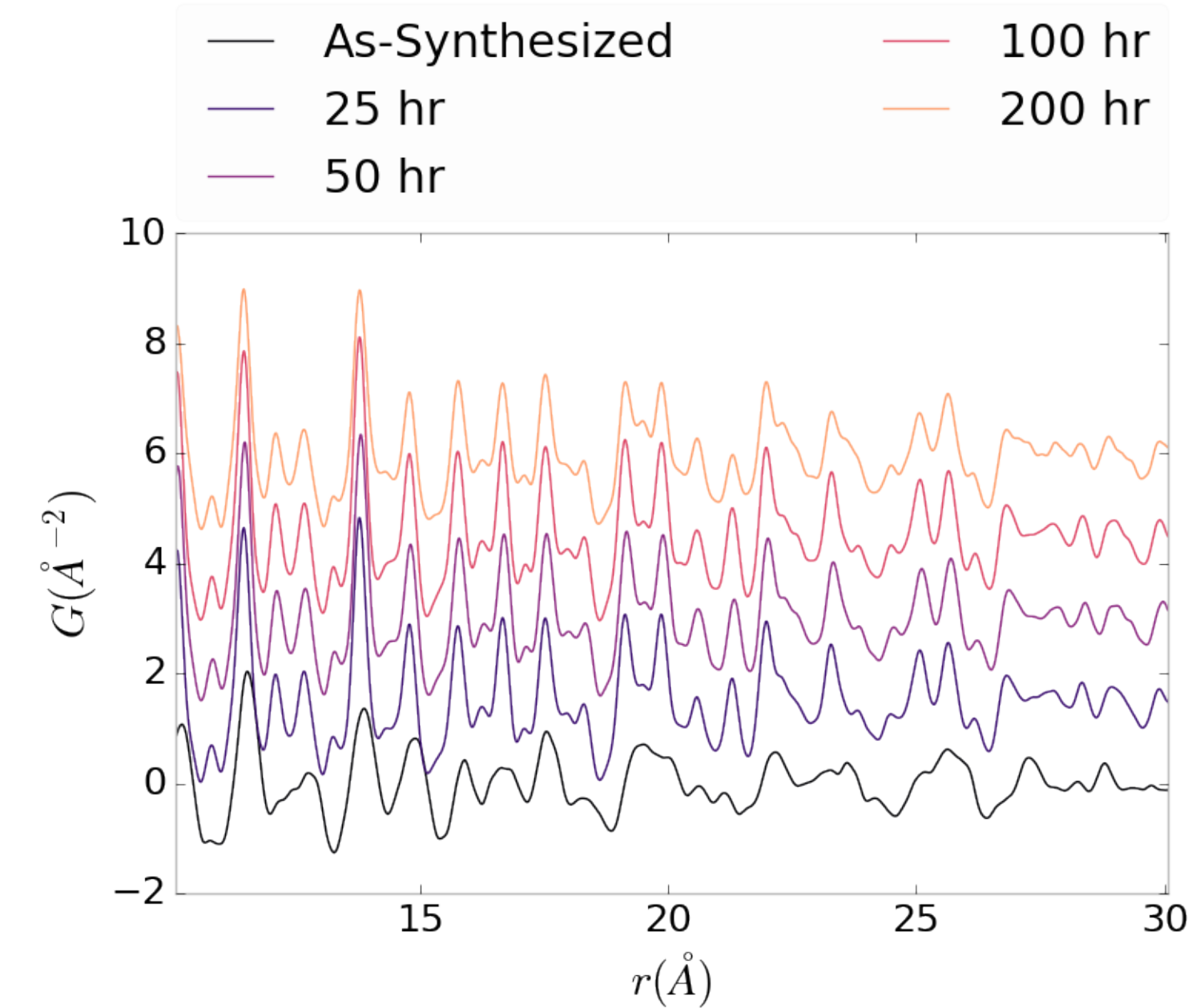


Figure A.22: Comparison of PNO sample PDFs as a function of annealing time cooled back to room temperature

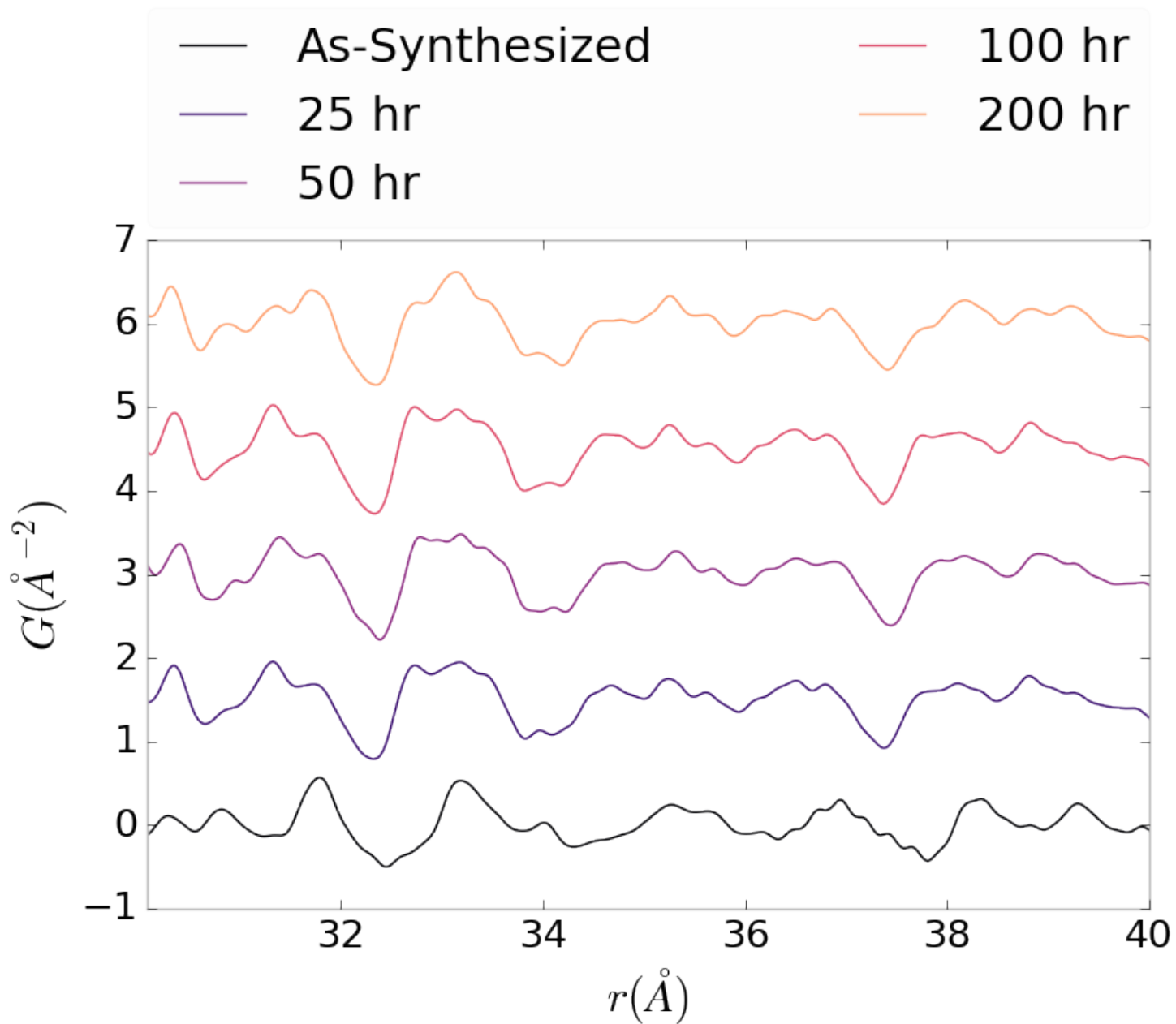


Figure A.23: Comparison of PNO sample PDFs as a function of annealing time cooled back to room temperature

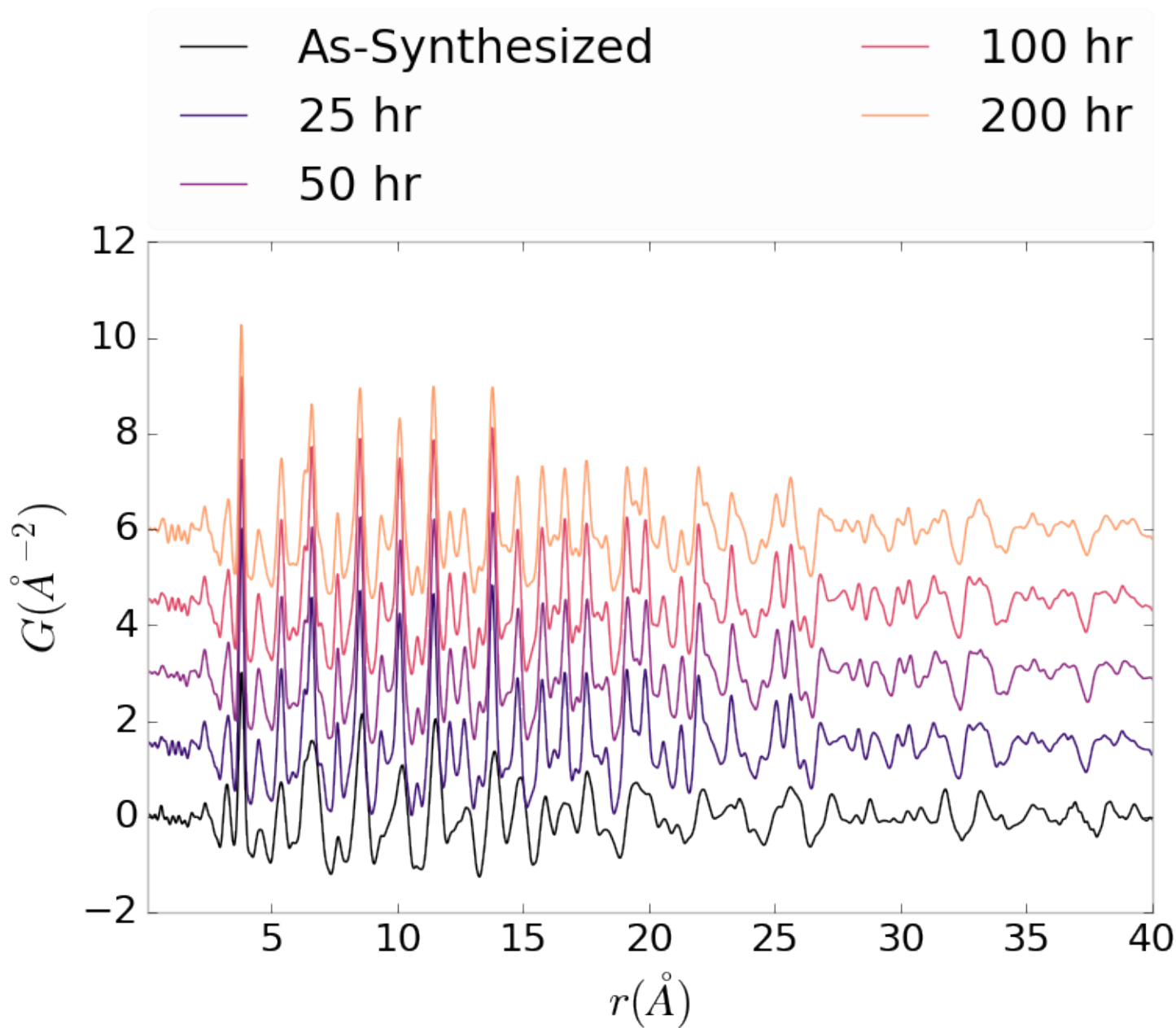


Figure A.24: Comparison of PNO sample PDFs as a function of annealing time cooled back to room temperature

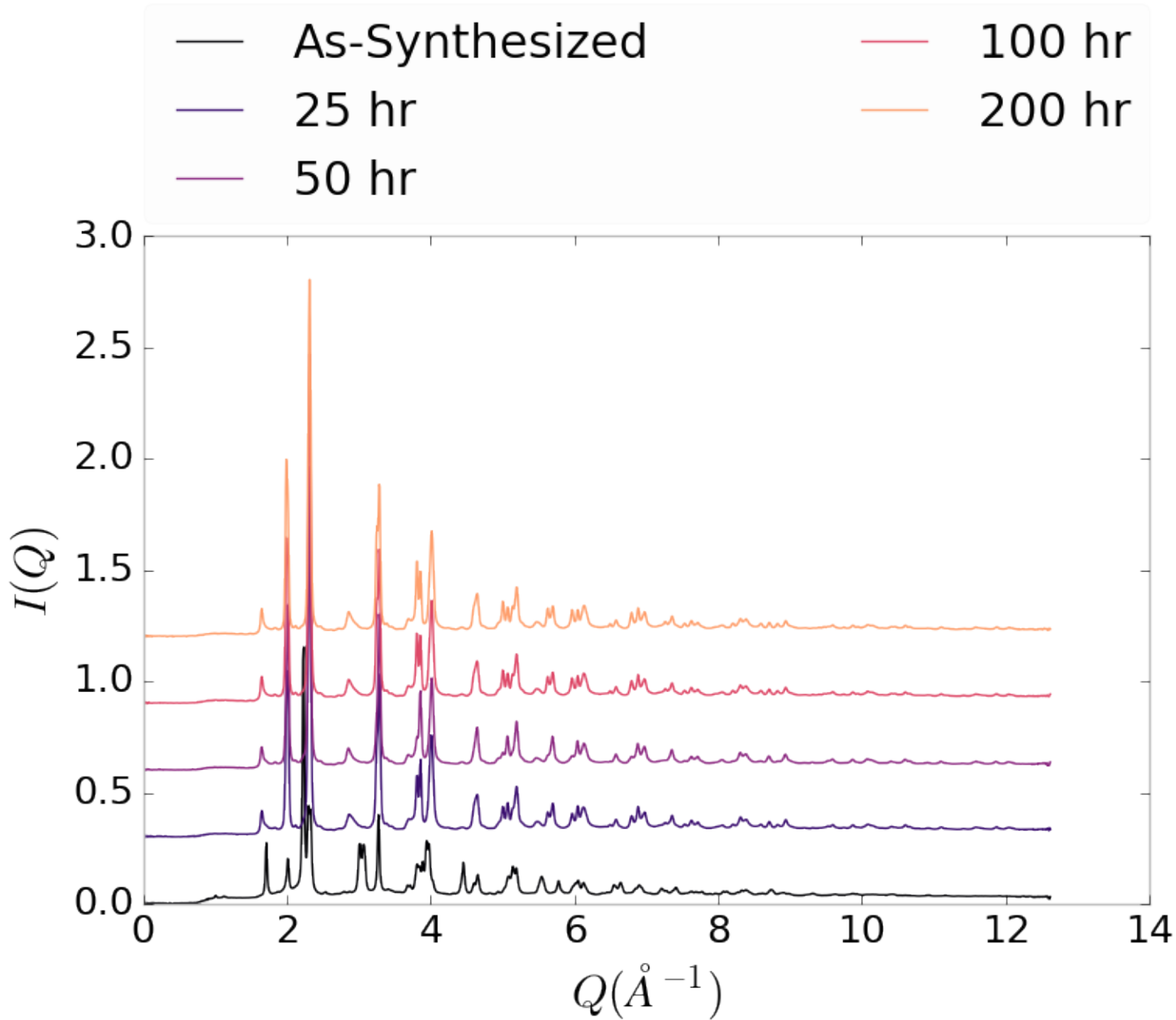


Figure A.25: Comparison of PNO sample  $I(Q)$  as a function of annealing time at room temperature

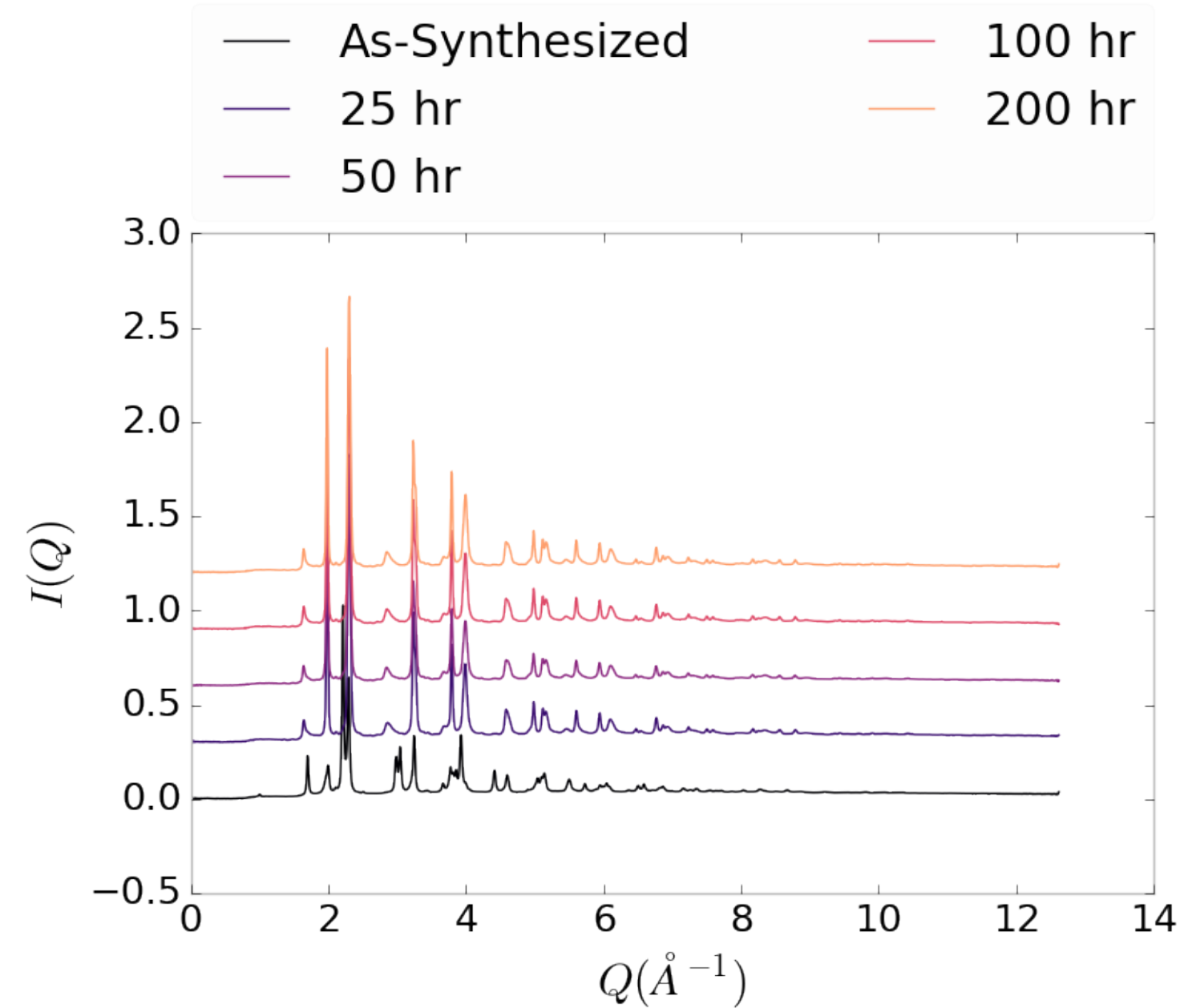


Figure A.26: Comparison of PNO sample  $I(Q)$  as a function of annealing time at operating temperature

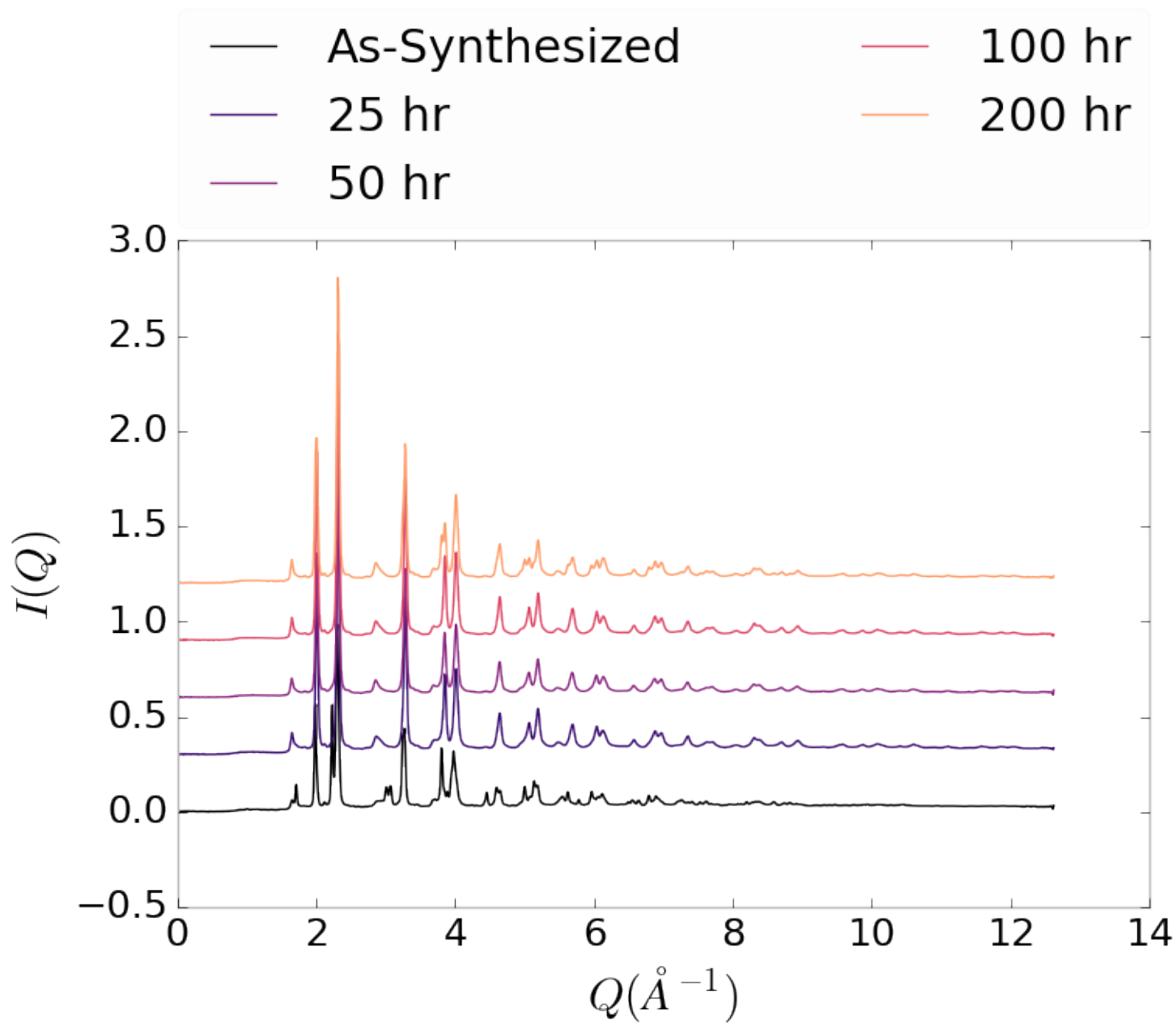


Figure A.27: Comparison of PNO sample  $I(Q)$  as a function of annealing time cooled back to room temperature